MOCVD GROWTH AND CHARACTERIZATION OF AL-RICH ALN/ALGAN EPILAYERS AND QUANTUM WELLS

by

TALAL MOHAMMED AHMAD AL TAHTAMOUNI

B. S., Yarmouk University, Irbid, Jordan, 1994

M. S., Western Michigan University, 2003

AN ABSTRACT OF A DISSERTATION

submitted in partial fulfillment of the requirements for the degree

DOCTOR OF PHILOSOPHY

Department Of Physics
College of Arts and Sciences

KANSAS STATE UNIVERSITY
Manhattan, Kansas

2007

Abstract

The correlation between polarity and material quality of un-doped $Al_{0.81}Ga_{0.19}N$ was studied. The overall material quality is significantly influenced by the growth polarity. The epilayers with aluminum-polarity have a much higher crystalline quality and better surface morphology than those of nitrogen-polarity. Nitrogen-polar growth more readily incorporates unintentional impurities.

A-plane AlN epilayers have been grown on *r*-plane sapphire substrates. The orientation and high crystalline quality were confirmed by x-ray diffraction (XRD) θ-2θ scan exhibiting a reflection peak at $2\theta = 59.4^0$ and rocking curve of the (110) reflection having a linewidth of 940 arcsec. Room temperature photoluminescence (PL) spectroscopy showed that the surface emission intensity of *a*-plane AlN epilayers is comparable to that of *c*-plane AlN. PL spectra of Mg-doped *a*- and *c*-plane AlN revealed that the Mg level in both *a*- and *c*-plane AlN is identical and is about ~ 0.5 eV.

Identically designed *a*-plane and *c*-plane $AlN/Al_{0.65}Ga_{0.35}N$ QWs have been grown on *a*- and *c*-plane AlN/Al_2O_3 templates respectively, and their PL emission properties were studied. Low temperature PL characteristics of *a*-plane QWs are primarily governed by the quantum size effect, whereas those of *c*-plane QWs are significantly affected by the polarization fields.

The growth of AlN epilayers on SiC substrates was investigated. A smooth, crack free AlN epilayer with high optical and crystalline quality was achieved. Because of its high quality, AlN was used as active layer in a hybrid Schottky photodetector.

Highly conductive Si-doped $Al_{0.75}Ga_{0.25}N$ alloys were grown on AlN/SiC templates. The effects of using Indium as a surfactant during the growth of Si-doped $Al_{0.75}Ga_{0.25}N$ epilayers at relatively high temperature 1050 ^{0}C were studied. Indium significantly increases the doping efficiency as shown by RT Hall measurements. RT PL measurements show a clear correlation between emission intensity of the defect related transition and indium flow rate.

P-type conductivity has been obtained in beryllium doped GaN by MOCVD. The activation energy of the beryllium acceptor was estimated to be 118 ± 4 meV, which is about 40 meV less than the activation energy of the Mg acceptor in GaN.

MOCVD GROWTH AND CHARACTERIZATION OF AL-RICH ALN/ALGAN EPILAYERS AND QUANTUM WELLS

by

TALAL MOHAMMED AHMAD AL TAHTAMOUNI

B. S., Yarmouk University, Irbid, Jordan, 1994

M. S., Western Michigan University, 2003

A DISSERTATION

submitted in partial fulfillment of the requirements for the degree

DOCTOR OF PHILOSOPHY

Department of Physics
College of Arts And Sciences

KANSAS STATE UNIVERSITY
Manhattan, Kansas

2007

Approved by:

Major Professor
Hongxing Jiang

Copyright

Abstract

The correlation between polarity and material quality of un-doped $Al_{0.81}Ga_{0.19}N$ was studied. The overall material quality is significantly influenced by the growth polarity. The epilayers with aluminum-polarity have a much higher crystalline quality and better surface morphology than those of nitrogen-polarity. Nitrogen-polar growth more readily incorporates unintentional impurities.

A-plane AlN epilayers have been grown on *r*-plane sapphire substrates. The orientation and high crystalline quality were confirmed by x-ray diffraction (XRD) θ-2θ scan exhibiting a reflection peak at $2\theta = 59.4^0$ and rocking curve of the (110) reflection having a linewidth of 940 arcsec. Room temperature photoluminescence (PL) spectroscopy showed that the surface emission intensity of *a*-plane AlN epilayers is comparable to that of *c*-plane AlN. PL spectra of Mg-doped *a*- and *c*-plane AlN revealed that the Mg level in both *a*- and *c*-plane AlN is identical and is about ~ 0.5 eV.

Identically designed *a*-plane and *c*-plane $AlN/Al_{0.65}Ga_{0.35}N$ QWs have been grown on *a*- and *c*-plane AlN/Al_2O_3 templates respectively, and their PL emission properties were studied. Low temperature PL characteristics of *a*-plane QWs are primarily governed by the quantum size effect, whereas those of *c*-plane QWs are significantly affected by the polarization fields.

The growth of AlN epilayers on SiC substrates was investigated. A smooth, crack free AlN epilayer with high optical and crystalline quality was achieved. Because of its high quality, AlN was used as active layer in a hybrid Schottky photodetector.

Highly conductive Si-doped $Al_{0.75}Ga_{0.25}N$ alloys were grown on AlN/SiC templates. The effects of using Indium as a surfactant during the growth of Si-doped $Al_{0.75}Ga_{0.25}N$ epilayers at relatively high temperature 1050 ^{0}C were studied. Indium significantly increases the doping efficiency as shown by RT Hall measurements. RT PL measurements show a clear correlation between emission intensity of the defect related transition and indium flow rate.

P-type conductivity has been obtained in beryllium doped GaN by MOCVD. The activation energy of the beryllium acceptor was estimated to be 118 ± 4 meV, which is about 40 meV less than the activation energy of the Mg acceptor in GaN.

Table of Contents

List of Figures

List of Tables

Acknowledgements

All praise is due to Allah for his blessings and guidance. No words will be sufficient to express my acknowledgement to my parents, Mohammed Al tahtamouni and Wasfieh (Munirah) Al shaniek for spending their whole life caring for me.

I would like to express my thanks and gratitude to my advisors, Professor Hongxing Jiang and Professor Jingyu Lin for their support, encouragement, and guidance during my research. I would also like to thank Dr. Jing Li for his help and informative discussions. I would like to thank Professor Sixuan Jin, Dr. Zhaoyang Fan, Cris Ugolini, Neelam Khan, Weiping Zhao, Rajendra Dahal, Bed Nidhi Pantha, and Ashok Sedhain for their cooperation, assistance and useful discussions. I would also like to thank our past group members Dr. Kyoung Hoon Kim, Dr. Mim Lal Nakarmi, Dr. Neeraj Nepal for valuable discussion and help. I am grateful to other members in my committee, Professor Michael O'Shea, Professor James Edgar, and chairperson, Professor Dolores Takemoto. I appreciate their valuable advice and time.

I would like to acknowledge my brothers and sisters, Ahmad, Ismaiel, Buthaina, Ammar, Mahmood, Eman, Fatima, Noor, Alaa alden, and other family members, Omar, Rami, Rana, Rama, and Zied for their continuous love and support. I would like also to thank all friends around me, especially Mohamed Ishak, for their support.

Enough thanks can't be given to my wife, Manar for her support and understanding of the long hours at work and the late nights of writing.

Dedication

To my parents Mohammed Al tahtamouni and Wasfieh (Munirah) Al shaneik, whom I owe everything in my life, to my brothers and sisters, Ahmad, Ismaiel, Buthaina, Ammar, Mahmood, Eman, Fatima, Noor, Alaa alden, to my wife, Manar, and to my lovely daughter, Munirah.

CHAPTER 1 - Introduction to III-nitrides

1.1 Introduction

Group III-nitrides (InN, GaN, AlN and their ternary and quaternary alloys) are direct bandgap compound semiconductors, which crystallize in the wurtzite structure in the most stable form. The bandgap ranges from 0.7 eV for InN to 3.4 eV for GaN to 6.1 eV for AlN (figure 1.1), spanning a very wide spectral range from infrared (IR) to deep ultra violet (DUV). Being direct-bandgap semiconductors, they can be used to fabricate light-emitting devices such as light-emitting diodes (LED) and laser diodes (LDs) over this entire spectral range. Another reason that makes the III-nitride semiconductors attractive for device applications is their high bond strength. ZnSe-based II-VI semiconductors also have bandgaps suitable for short-wavelength optoelectronic devices, but the bond strength in the II-VI wide-bandgap semiconductors is relatively low. Due to the stronger bonds, nitride based devices have the ability to operate in high-temperature environments and are compatible with high processing temperatures. In addition, the III-nitrides have a high thermal conductivity, which allows for efficient heat dissipation from devices operating in high-current conditions (e.g. lasers and power transistors). They also have a high electron saturation velocity (V_s), which is a useful property for a number of device applications such as p- i-n photodetectors, because high V_s translates into higher device speed [1-4].

To design high-performance optoelectronic devices, the use of heterostructures is essential. Fabrication of a heterostructure, however, may be limited by alloy miscibility and lattice constant considerations. Low miscibility leads to difficulty in growth of homogeneous material and a high lattice mismatch leads to relaxation and material quality deterioration. The AlGaN alloy system is fully miscible, and the lattice mismatch between GaN (c-lattice constant c = 5.185 Å) and AlN (c = 4.98 Å) is small. As a result, much flexibility is available in the design of optoelectronic devices using AlGaN alloys. As noted before, the bandgap of AlGaN alloys spans the spectral range from 365 nm to 200 nm. As a result, it is a very attractive material for fabrication of UV light emitters and photodetectors.

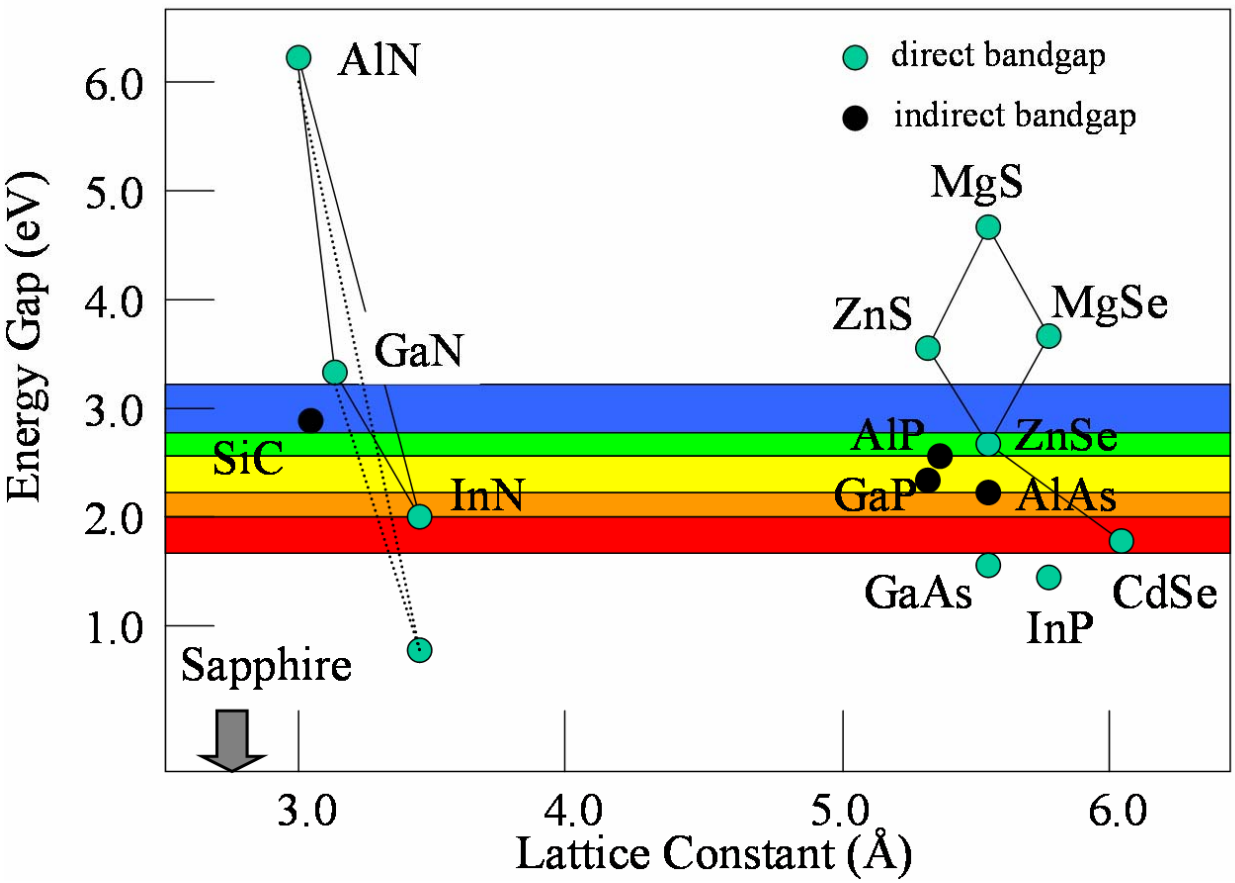

Figure 1.1 Bandgap energy of various semiconductors versus in plane lattice constant (after ref. [5]). Recent work indicates that the bandgap of InN is around 0.7 eV [6].

1.2 General properties of III-nitrides

The thermodynamically stable structure for AlN, GaN and InN is the wurtzite structure. Though under special conditions they can also be grown in the zinc blende structure, the wurtzite nitrides are grown and studied almost exclusively. In the wurtzite structure, there are two interpenetrating hexagonal close-packed lattices, each displaced from the other ideally by (3/8) c. Each atom is tetrahedrally bonded to four atoms of the other type as shown in figure 1.2, and the primitive unit cell is simple hexagonal with a basis of four atoms, two of each species. There is no inversion symmetry in this lattice along the [001] direction (same holds true for zinc blende structure along [111] direction), resulting in all atoms on the same plane at each side of a bond being the same. Hence, a GaN crystal has two distinct faces, the Ga-face and the N-face.

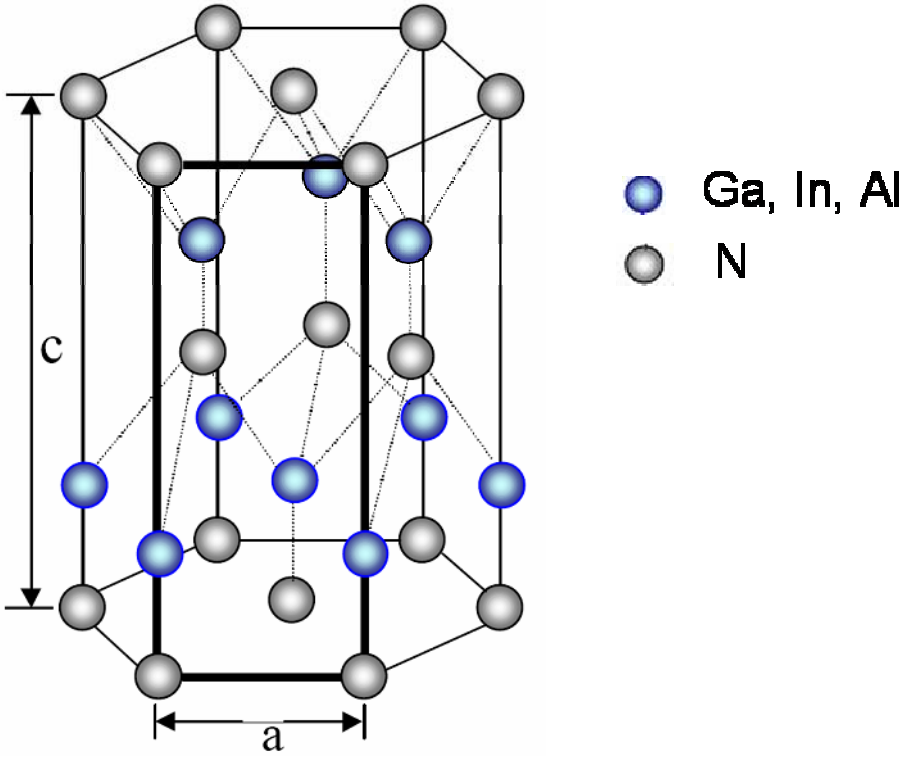

Figure 1.2 Schematic diagram showing the hexagonal wurtzite structure of InN, GaN, and AlN.

The arrangement of atoms for the Ga-face and the N-face are shown in Fig. 1.3. Note that for Ga-face the N-atom is stacked directly over the Ga-atom and vice-versa for the N-face. The growth polarity of III-nitrides is important because it dictates the direction of the polarization vector resulting from spontaneous and induced piezoelectric fields. Also, surfaces of differing polarity can have profound effects on many physical characteristics such as impurity incorporation.

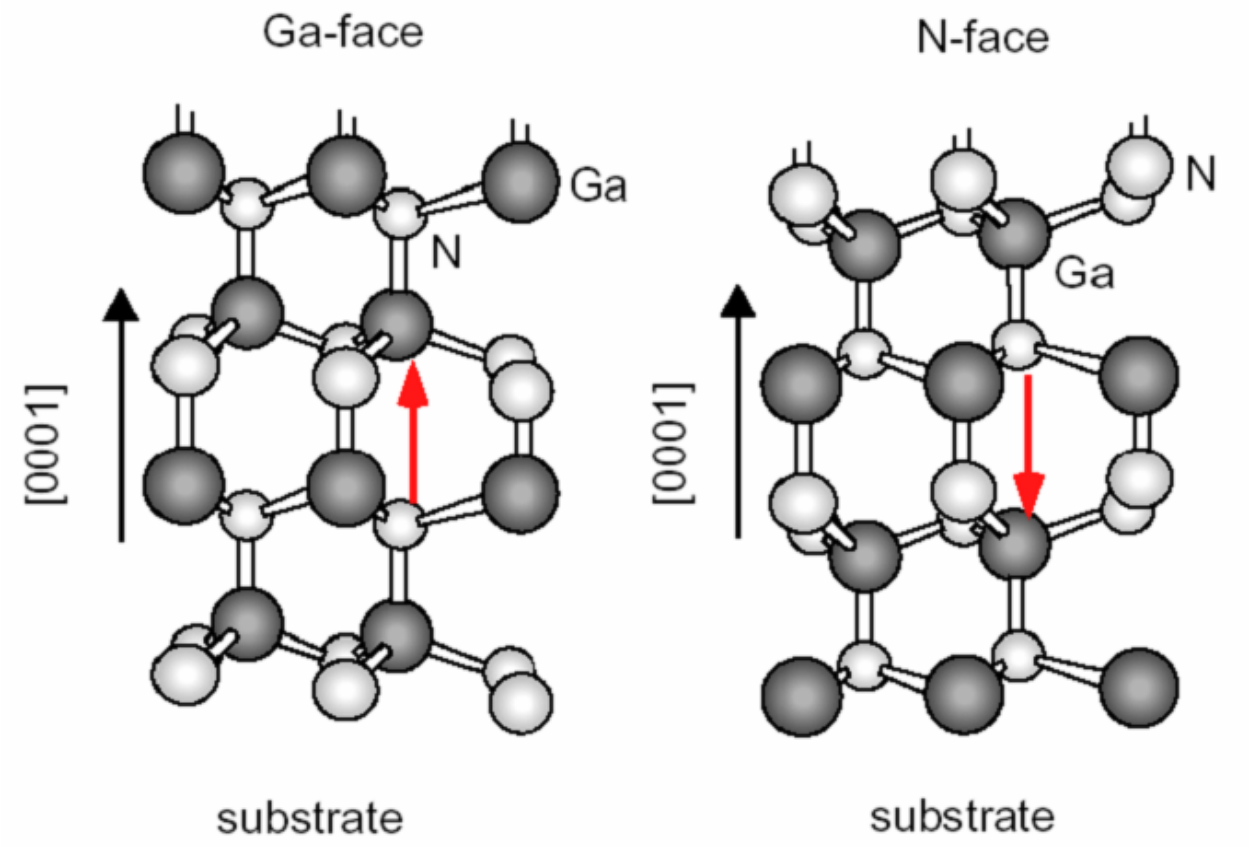

Figure 1.3 Atomic arrangement in Ga-face and N-face GaN crystals. The arrow pointing from N to Ga atom shows the direction of the spontaneous polarization (after ref. [7]).

The wurtzite lattice is characterized by three parameters: the edge length of the basal hexagon (a), the height of the hexagonal lattice cell (c), and the cation-anion bond length ratio (u) along the [001] axis in units of c. In an ideal wurtzite crystal, the c/a ratio is 1.6330 and u is 0.375. Because of the different metal cations, the bond lengths and the resultant c/a ratio of AlN, GaN and InN are different. This fact is very important because the degree of non-ideality is a determining factor in the strength of polarization in group-III nitrides.

1.3 Spontaneous and piezoelectric polarizations

Group-III nitrides are special among the III-V compound semiconductors because of the fact that the group-V element involved is nitrogen, the smallest and the most electronegative group-V element. This has a strong impact on the properties of the III-nitrides. Because of the electronic configuration of the nitrogen atom, or rather the lack of electrons occupying outer electron orbitals, the electrons involved in the metal-nitrogen covalent bond will be strongly attracted by the coulomb potential of the nitrogen atomic nucleus. This means that the metal-nitrogen covalent bond will have stronger ionicity compared to other III-V covalent bonds. This ionicity (a localized polarization) will result in macroscopic polarization if there is a lack of inversion symmetry in the crystal.

As mentioned before, there is no inversion symmetry in the wurtzitie III-nitrides along the c-axis. Absence of this inversion symmetry, in addition to the strong ionicity of the metal-nitrogen bond, results in a strong macroscopic polarization along the [001] direction in the III-nitrides. Since this polarization effect occurs in the equilibrium lattice of the III-nitrides at zero strain, it is called spontaneous polarization [8].

If stress is applied to the III-nitride lattice, the ideal lattice parameters c and a of the crystal structure will be changed to accommodate the stress. Thus the polarization strength will be changed. This additional polarization in strained III-nitride crystals, in addition to the spontaneous polarization already present, is called piezoelectric polarization [8]. For example, if the nitride crystal is under biaxial compressive stress, the in-plane lattice constant a will decrease and the vertical lattice constant c will increase, making the c/a ratio increase towards the ideal lattice value of 1.6330. This will decrease the polarization strength of the crystal, since the piezoelectric polarization and the spontaneous polarization will act in opposite directions. On the other hand, if the nitride crystal is under tensile stress, the in-plane lattice constant will increase

and the vertical lattice constant will decrease, lowering the c/a ratio further away from the ideal value 1.6330. This will increase the overall polarization, since the piezoelectric and the spontaneous polarizations now act in the same direction.

1.4 Polar and nonpolar wurtzite nitrides

The large electronic polarization fields (on the order of MV/cm) in the III-nitride semiconductors [8] affect the electronic properties (band diagrams, charge distributions) of layered structures in many ways. The polarization induced electric field is beneficial for the formation of a two-dimensional (2D) electron gas in high-electron mobility transistors (HEMTs) without the need of doping [7]. However, the built-in electric field created within quantum wells of optoelectronic device leads to a spatial separation of electron and hole wavefunctions, and results in a quantum-confined Stark effect. The consequences of this effect are a decreased recombination efficiency, and a red-shift of emission, thus limiting the performance of the optoelectronic devices. Thus the polarization of wurtzite nitrides has a deleterious effect on the performance of optoelectronic devices.

A promising means of eliminating internal field effects in the nitrides is through the growth of wurtzite device structures with nonpolar orientations, e.g. growth along the *m*- and *a*-direction as shown in Fig. 1.4.

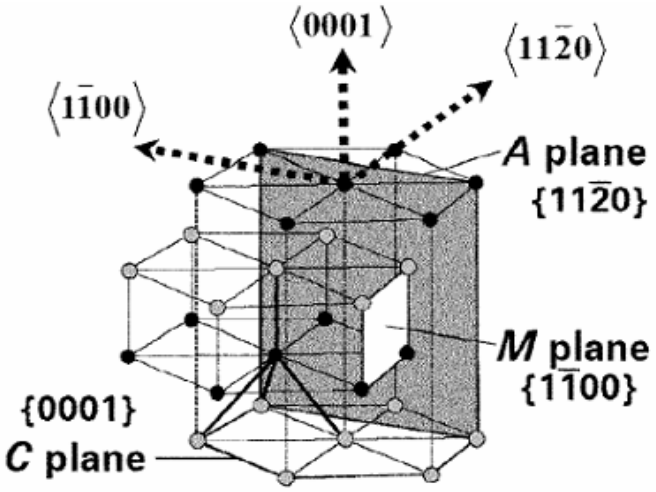

Figure 1.4 Polar and nonpolar crystal planes and directions of interest in hexagonal III nitrides (after ref.[9]).

With the *c*-axis lying within the plane of growing film, polarization discontinuities do not exist at the heterointerfaces. Therefore, internal electric fields are absent in nonpolar quantum-wells resulting in a flat-band condition as shown in Fig. 1.5. Therefore, optoelectronic devices grown and fabricated along nonpolar direction promise to offer improved performance over their conventional c-plane counterparts.

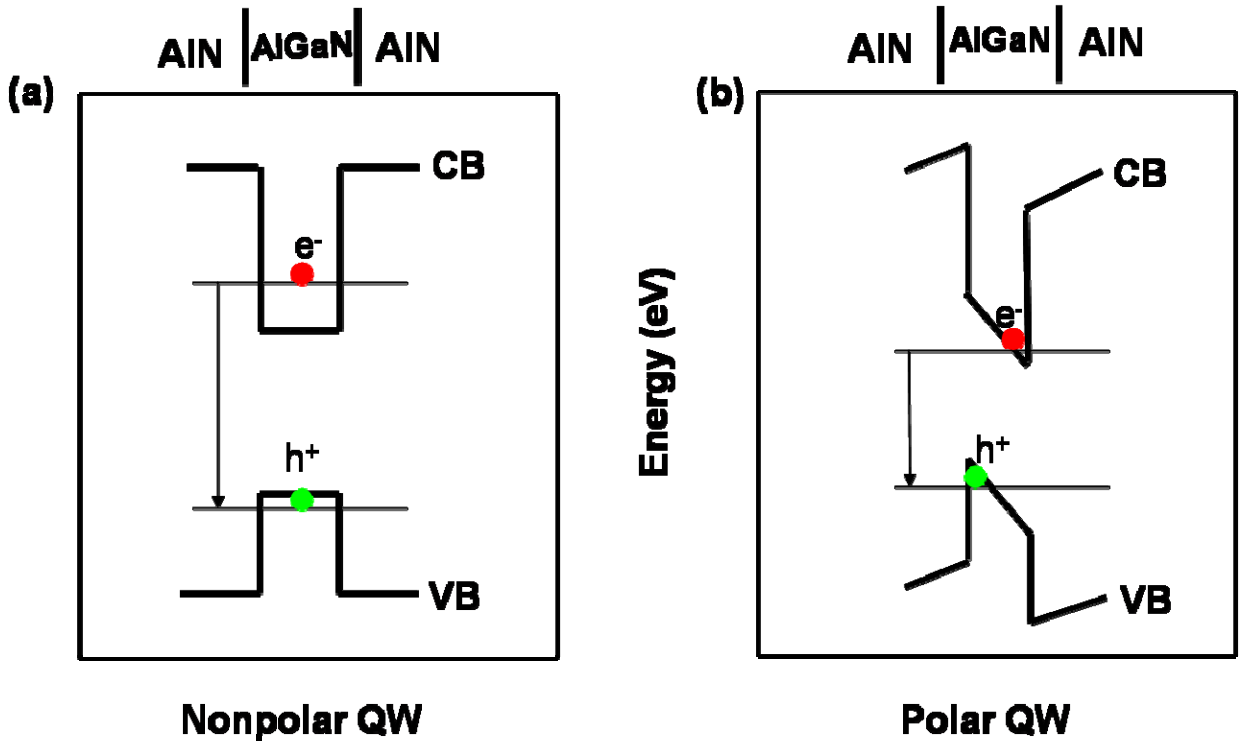

Figure 1.5 A comparison of band diagram between (a) non-polar a-plane AlN/AlGaN SQW in the absence of polarization electric field and (b) polar c-plane AlN/AlGaN SQW in the presence of polarization electric field.

1.5 Choice of substrate

The aim of this work is to assess the individual steps needed for optimizing the growth of III-nitride optoelectronic devices such as light emitting diodes (LEDs) and photodetectors. The first step is the choice of a suitable substrate. Table 1.1 displays the characteristics of some substrates available for epitaxial growth of III nitride materials. To select the optimum substrate, several issues have to be considered pertaining to growth related and device related ones.

For growth, it is generally accepted that lower lattice and thermal mismatches, smoother and cleaner surfaces as well as higher chemical and thermal stabilities result in lower defect densities. For device operation, a good choice will in general depend on the individual demand of the device. In the case of high power applications, like LDs, the substrate acts as a heat sink. Thus, the thermal conductivity should be as high as possible.

Until recently, native substrates for homoepitaxy of nitrides were not available at all. The substrates recently made available commercially are of small size, low material quality and high cost. Most of the epitaxial growth of III-nitrides is done on sapphire substrates because of its wide availability in high-quality, hexagonal symmetry, adequate material quality, compatibility with high temperature growth, ease of handling and pregrowth cleaning, and low cost. However, due to the thermal and lattice mismatch between sapphire and the III-nitrides, growth has to be started with a thin polycrystalline nucleation layer which incorporates a high threading dislocation density into the material. A thick epilayer of 1 to 2 μm thickness is therefore required to be grown to reduce the threading dislocation density to acceptable levels before starting the growth of the device layers. Another limitation of sapphire substrates is that due to the large lattice mismatch, the nitride epilayers grown on them have a 30^0 rotation in the c-plane. This causes a misalignment between the cleavage planes of the nitrides and the sapphire substrates. As a result, when an epitaxial structure on sapphire is cleaved, the substrate cleaves while the epilayer is broken along the sapphire cleavage plane (known as break and cleave). This eliminates the possibility for formation of mirror facets by cleaving for edge emitting laser fabrication. The facets on an epilayer grown on sapphire must be fabricated by dry etching, which can be a challenging process.

In contrast to sapphire, hexagonal SiC has a better lattice and thermal expansion coefficient match with the III- nitrides. SiC is also high-temperature compatible for use in the high-temperature CVD growth environment, and in high-power device applications. Additionally, SiC has a much higher thermal conductivity compared to sapphire, which makes heat dissipation for high-power devices a much simpler issue. SiC wafers are also available in n-type form, allowing for fabrication of backside contact directly to the substrate. It is also available in a semi-insulating form (at a very prohibitive price) which is required for most electronic device applications. Due to the smaller lattice mismatch, the cleaving problem in the case of sapphire substrates is not present. One problem for the SiC substrates, however, is that they are not UV-transparent, which makes light extraction or light introduction through the substrate not possible for UV operation.

Table 1.1 Characteristics of some substrates available for epitaxial growth of III-nitrides.

Property	sapphire	SiC	GaN	AlN
Lattice-match to GaN	poor	moderate	excellent	moderate
Lattice-match to AlN	poor	excellent	moderate	excellent
Thermal conductivity	poor	excellent	excellent	excellent
Electrical resistivity	excellent	moderate	poor	excellent
UV transparency	excellent	poor	moderate	excellent
Cost	excellent	moderate	poor	poor

1.6 Doping of III-nitrides

The effective doping of GaN and its alloys with AlN and InN plays a crucial role in the application of nitride semiconductors for electronic and optoelectronic devices. Therefore, investigation of the doping of III nitrides is very important for both basic research and applications. For *n*-type doping of nitrides, a number of elements (e.g., Si) can be successfully used as dopants, and carrier concentrations exceeding $5x10^{20}$ cm^{-3} can routinely be achieved [10]. The situation is less favorable for *p*-type doping. Magnesium is the acceptor of choice, as it can be incorporated in concentrations up to about 10^{20} cm^{-3}. But, because of its large ionization energy (160 meV) the resulting room-temperature hole concentration is only about 10^{18} cm^{-3}, i.e., only about 1% of Mg atoms are ionized at room temperature. Increasing the Mg concentration beyond 10^{20} cm^{-3} leads to a saturation and decrease in the hole concentration [11]. The Mg solubility limit is the main cause of this behavior [12]. The limited conductivity of *p*-type doped layers constitutes an impediment for progress in device applications [13].

It would be desirable to identify an alternative acceptor that would exhibit higher solubility and/or lower ionization energy. Previous computational studies [14–16] have addressed a variety of candidate acceptors, including Li, Na, K, Be, Zn, Ca, and Cd. Only Be has emerged as a viable acceptor, exhibiting a higher solubility and a lower ionization energy than Mg. However, self-compensation may occur due to incorporation of Be on interstitial sites, where it acts as a donor [15].

1.7 Brief history of nitrides development

GaN was first synthesized in 1932 by passing ammonia through hot Ga [17]. Later, the same technique was used to get GaN needles and platelets, which were used for studying the optical and structural properties [18, 19]. However, the progress in research and development of GaN before the 1970s was slowed down due to the lack of modern crystal growth techniques. With the technological development of epitaxial growth of high-quality thin films on appropriate substrate materials, the first GaN was epitaxially grown on sapphire in 1969 [20]. The films at early time were unintentionally n-type, with electron concentrations ranging from 10^{18} to 10^{20} cm^{-3}. Such high *n*-type background concentrations made it difficult to achieve *p*-type doping.

Most potential acceptor elements, such as Mg, Be, Zn and Cd, were incorporated into GaN, either during growth [21-24] or by post-growth ion implantation [25], but no *p*-type conduction was obtained. The first light emitting diode (LED) based on GaN was produced by a Zn-doped metal-insulator-semiconductor structure but showed only a very low efficiency [26]. After this initial progress made during the 1970s, the pace of research of GaN became slow, because of the lack of high quality epilayers and the lack of success in making *p*-type GaN. Ultimately, the origin of high background electron concentration was identified as oxygen, incorporated during the growth [27], instead of N vacancies as was assumed before. It was not until the modern growth techniques of molecular beam epitaxy (MBE) and metal-organic vapor phase epitaxy (MOVPE, also called metal-organic chemical vapor deposition, i.e. MOCVD) were developed that further development and progress took place. Many efforts were made to optimize growth conditions and introduce more suitable buffer layers to reduce the *n*-type background doping levels. Eventually background levels below 10^{17} cm^{-3} at room temperature were achieved, in the late 1980s and the early 1990s. This remarkable progress was made by an insertion of either a low-temperature AlN [28, 29] or a low-temperature GaN buffer layer [30, 31] before the GaN growth.

With regards to *p*-type doping, although the group II element Mg had long been expected to be a good acceptor dopant and significant amounts of Mg could be incorporated into GaN during MOVPE growth, it was impossible to detect positive charge carriers at room temperature. In fact, the films turned out to be highly resistive. An accidental discovery allowed Amano *et al*. [32] to demonstrate that post-growth low-energy electron beam irradiation activates Mg-doped GaN films and converts them from the as-grown highly resistive state to a *p*-type conductive state. Previous observations in other III-V materials such as GaAs and InP had established that hydrogen incorporation plays a crucial role in passivating *p*-type dopants. Based on this knowledge, Nakamura *et al*. [33] improved the activation of the Mg acceptors in MOVPE-grown GaN by utilizing thermal annealing in N_2 causing the resistivity to drop from ~10^6 to 2 Ωcm. These advances led to the first GaN based p-n junction LED in 1994 [34]. Present-day high-brightness nitride-based LEDs are mostly comprised of (In, Ga)N or GaN quantum well (QW) structures as active regions. This breakthrough has paved the way for further rapid research and development of nitride-based devices.

CHAPTER 2 - MOCVD and characterization tools

In this chapter, the experimental apparatus employed to grow and characterize the synthesized materials are discussed. Details of the metalorganic chemical vapor deposition (MOCVD) process, including the growth system are provided. Various characterization tools utilized in this work are discussed, including photoluminescence (PL), X-ray diffraction (XRD), Hall measurements, atomic force microscopy (AFM), and scanning electron microscopy (SEM).

2.1 Meta-lorganic Chemical Vapor Deposition (MOCVD)

The metalorganic chemical vapor deposition (MOCVD) is a vapor-phase process for producing an epitaxial film of a semiconductor deposited on a single crystal substrate. MOCVD is a proven technique for obtaining high-quality, high-purity epitaxial layers in a variety of material systems. MOCVD utilizes metalorganics, such as trimethyl-aluminum (TMAl), as sources for the group-III elements. The group-V element is usually a hydride such as ammonia (NH_3). Typically, the hydride reacts with the metalorganic source in hydrogen ambient under appropriate temperature and pressure conditions producing molecules of the required semiconductor material, which then adsorbs on the substrate, producing an epitaxial layer. MOCVD can occur in one of two growth regimes: diffusion-controlled and kinetically controlled. Kinetic control is achieved when the reaction rate is limited by the reaction at the surface, rather than by the rate of arrival of precursors at the surface. This mode of growth is usually not desired because this leads to high non-uniformity due to a small spatial variation of temperature. The desired diffusion-controlled growth is obtained when the deposition rate is controlled by the precursor arrival rate and the temperature is high enough to support a much higher growth rate. More details on MOCVD growth mechanism can be found in reference [35].

Compared to the growth of conventional III-V materials, MOCVD growth of nitrides is problematic because of the involvement of ammonia. Ammonia is a corrosive substance, thus requiring careful selection of materials for fabrication of the reactor chamber. Also, ammonia is a very stable compound, thus requiring a high temperature for dissociation. The high growth temperature poses problems, such as the thermal strain because the substrate and epilayer are

different materials with different thermal expansion coefficients. During cooling, thermal strain will inevitably build in the layer in the amount proportional to the growth temperature. Alternate nitrogen sources have been studied to eliminate the growth requirements imposed by ammonia. However, a high-temperature is required to provide sufficient surface mobility to the adsorbed molecules to create a high-quality crystal. Additionally, the highly volatile nature of nitrogen requires that a high partial pressure of the nitrogen be maintained in the vapor, which leads to the need for very high ammonia partial pressures. This results in a large V/III ratios (ratio of the flow rates of group V element to that of group III element). This complicates the ability to obtain of laminar flow. Due to the high partial pressure of ammonia, growth rate of the epilayer can be precisely controlled by adjusting only group III element flows.

2.2 MOCVD system

The MOCVD growth system can be divided into four main components: the gas handling system, the reaction chamber, the heating system, and the exhaust and low pressure pumping system. In this work, the materials were grown by a home built MOCVD system. The system has 4 metal-organic (MO) sources, TMGa, TMAl, TMIn and Cp_2Mg, H_2, N_2, NH_3 and SiH_4 gas lines. All the MO sources are temperature and pressure controlled to ensure constant vapor pressure. All gas flows are computer controlled via mass flow controllers. All MO sources are held in stainless steel bubblers mounted in temperature controlled chillers. The temperature of MO sources, TMGa, TMAl, TMIn, and Cp_2 Mg are set at 0 for TMGa and 20 ^{0}C for other sources. The resultant source vapor is carried by hydrogen gas via a mass flow controller to the manifold of the MOCVD. Due to the reactivity of metalorganics with water vapor and oxygen, some type of system must be incorporated for drying and purifying the bulk carrier gas. For our system, the input hydrogen (H_2) carrier gas is purified through a heated (~ 400 °C) Palladium (Pd) cell membrane. The Pd cell operates on the principle of diffusion of hydrogen through a Pd membrane. The Pd diffusion cell produces an ultra pure stream of hydrogen gas by utilizing a unique property of the metal palladium. The hydrogen diffuses through the membrane by first dissociating into hydrogen atoms at the upstream, or ‘feed’, surface of the membrane. Each hydrogen atom loses its electron to the palladium surface and then diffuses through the metal lattice as a proton. The protons finally recombine with electrons on the downstream or “pure” side and form hydrogen molecules. Because of the process, impurities on the “pure” side of the

membrane are extremely low and typically less than 1 part per billion (ppb). A separate line for nitrogen gas is also used so that the growth can be carried out by either H_2, N_2, or mixed gas. Due to the reactivity between ammonia and the MO sources, ammonia is introduced to the reactor via a separate line to minimize the pre-reactions. High purity H_2, N_2 (99,999%) and blue ammonia (99,99994%) were used.

A high capacity mechanical pump (Pfeiffer DUO-350) with oil filter is used to pump down the system to low pressure. A throttle valve (MKS-Type-653) is used to adjust the reactor pressure in conjunction with the pressure controller (MKS-Type-651C) and the pressure sensor (MKS-Type 722). A turbo pump is assembled to pump the system to high vacuum ($1x10^{-5}$ Torr) prior to growth.

The system has a horizontal quartz reactor. A 10 kW RF generator (TIG-10/100) is used to raise the temperature of the susceptor. To hold the substrate, a BN coated graphite susceptor is used. The temperature of the susceptor is measured by a type R thermal couple. Temperature is controlled by the Eurotherm temperature (Model-904).

The growth temperature, pressure, and all valves, mass flow controllers (MFC) and pressure controller (PC) set-points were controlled through a programmable logic controller computer. The growth parameters and set-points were entered into a “recipe” file before growth was initiated. In addition to reducing the possibility of operator error, automatic control allows for very fast switching times between multiple source gases, further improving the interface quality of any heterostructures grown in the system.

Since oxygen and moisture are usually very detrimental to the growth of common semiconductors, care should be taken not to expose the growth chamber to atmosphere. To accommodate this along with the requirement of loading and unloading substrates, some sort of loading mechanism is required. In our MOCVD system the loading mechanism is based a nitrogen purged glove-box. Fig. 2.1 shows the picture of the MOCVD system used in this work.

Figure 2.1 Picture of MOCVD system used in this work.

An interferometer (EpiEye-2000) is attached to the growth chamber as an in-situ monitoring method for the growth. The interferometer consists of a laser of wavelength 670 nm and detector assembled in a stage to produce the interference pattern. A computer interfaced control unit receives the signal from the detector. The interference occurs from light reflected from surfaces of substrate and growing epilayer. The detector then receives the interference signal. From interference pattern, the growth rate and thickness of the epilayer can be calculated directly. The qualitative nature of the surface can also be monitored from the relative intensity of the interference pattern [37]. Fig. 2.2 shows a typical interference pattern of a Si-doped $Al_{0.75}Ga_{0.25}N$ epilayer grown on AlN/SiC template.

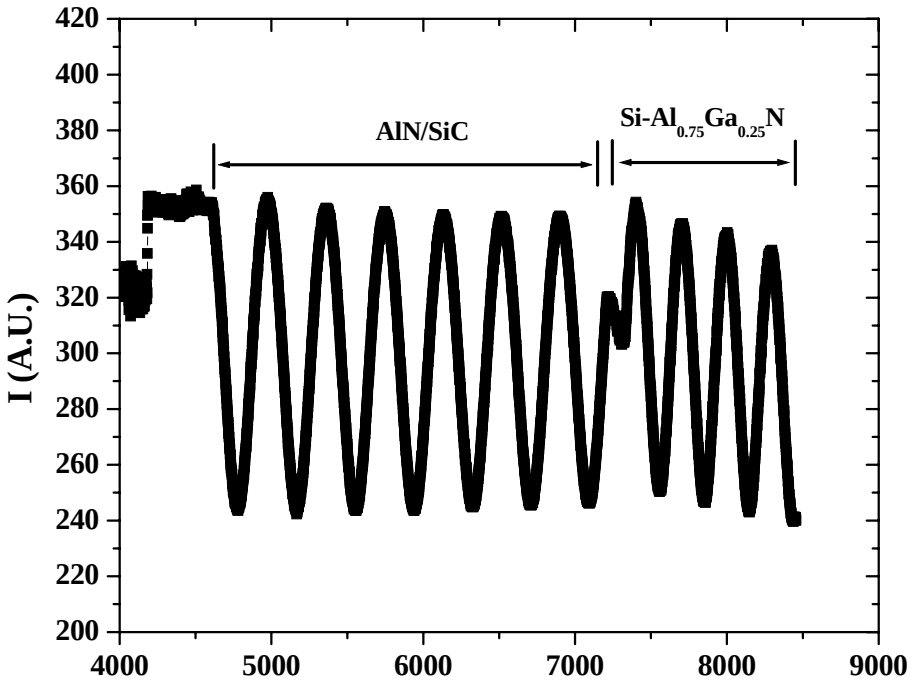

Figure 2.2 Interference pattern of a Si doped $Al_{0.75}Ga_{0.25}N$ layer grown on AlN/SiC template.

2.3 Common characterization techniques

In order to effectively grow high quality crystals and heterostructures we must have some means to evaluate both material quality and properties of the crystal. Therefore, characterization of the sample must be performed in order to optimize any growth parameters. There are many techniques available for characterization of semiconductor crystals, both non-destructive and destructive, using optical, electrical, and mechanical measurement. We present below a brief summary of each of the techniques used in our study.

2.3.1 Naked eye characterization

Typically the first characteristic noted when a thin film is unloaded from the growth reactor is its appearance to the unaided human eyes. This is crystal grower's most valuable tools. In this work, most films are gown on one side polished sapphire substrates. To the unaided eyes, these substrates are perfectly smooth and colorless. Once a proven recipe for growth has been developed, films on sapphire should appear clean and smooth. Deviations from this are indicative of some sort of change or instability in the growth equipment itself. Some of the commonly encountered unintentional growth variations are susceptor lifetime, chamber cleanliness, and vacuum integrity. That is not to say that these are the only factors which may cause a good recipe to go bad, but the problems listed above may not be obvious from equipment displays and readouts. The problems detectable in this manner are mainly associated with equipment maintenance deficiencies.

2.3.2 Optical microscope

The optical microscope is one of the characterization tools that requires no sample preparation and offers visual inspection of grown films. Optical microscopy is an indispensable tool for optimization of III-nitride films growth. Surface morphologies of the as grown films are often attributed to specific process parameters and experienced crystal growers are able to address these problems when necessary. In this research as grown samples are inspected by a Nikon eclipse ME 600 microscope. The surfaces of high-quality films should be smooth and relatively featureless.

2.3.3 X-ray diffraction (XRD)

X-raydiffraction (XRD) is an important characterization tool to study the crystallographic properties of the epitaxial layers. It provides structural information such as the layer orientation, lattice constant of the epilayer, strain and dislocation density in the layer. XRD allows for fast non-destructive measurements, and thus quick turn around for control and optimization of various growth parameters. This technique is based on the detection of x-ray scattering from various crystalline planes. The classic equation by Bragg is based on constructive interference of x-rays from lattice planes:

$$n\lambda = 2d_{hkl}\sin\theta \tag{2.1}$$

where λ is the x-ray wavelength, d_{hkl} is the lattice plane spacing and n is the order of the reflection. The Bragg angle (θ) can be calculated by solving Bragg's equation in first order. The lattice spacing for a hexagonal crystal system is given by:

$$d_{hkl} = \frac{1}{\sqrt{\frac{4}{3}\left(\frac{h^2 + hk + k^2}{a^2}\right) + \frac{l^2}{c^2}}} \tag{2.2}$$

where hkl are the Miller indices, and a and c are the in-plane and out-of-plane lattice constants, respectively [38].

The XRD system employed for this study is a Rigaku RINT2000V/PC series. The X-rays are produced from a sealed-off Cu x-ray tube. The characteristic wavelengths are Cu $K_{\alpha 1}$ = 0.154056 nm and Cu $K_{\alpha 2}$ = 0.154439 nm. The peak from source Cu $K_{\alpha 2}$ is eliminated via software application. The XRD system has a RINT2000V/PC series vertical goniometer.

Two basic types of scan were done with this system, ω and ω-2θ. The ω rocking curve is collected by fixing the detector at twice the Bragg angle (i.e. 2θ) and scanning over ω. As the detector angle is fixed, only one lattice plane spacing can be studied. Due to this, scans are sensitive to localized strain (dislocations) and mosaic structure. In the ω-2θ scan, both angles are set to the Bragg condition and the two angles are linked in a 1:2 ratio. In this case, various lattice spacing can be interrogated. An example for both types of scans is shown in Figures 2.3 and 2.4.

In Fig. 2.3 a ω-2θ scan of p-type GaN grown on AlN/SiC template (p-GaN/AlN/SiC). In Fig. 2.4 a ω rocking curve was measured on the symmetric (002) reflection for p-GaN film with a full width at half maximum (FWHM) of 320 arcsec.

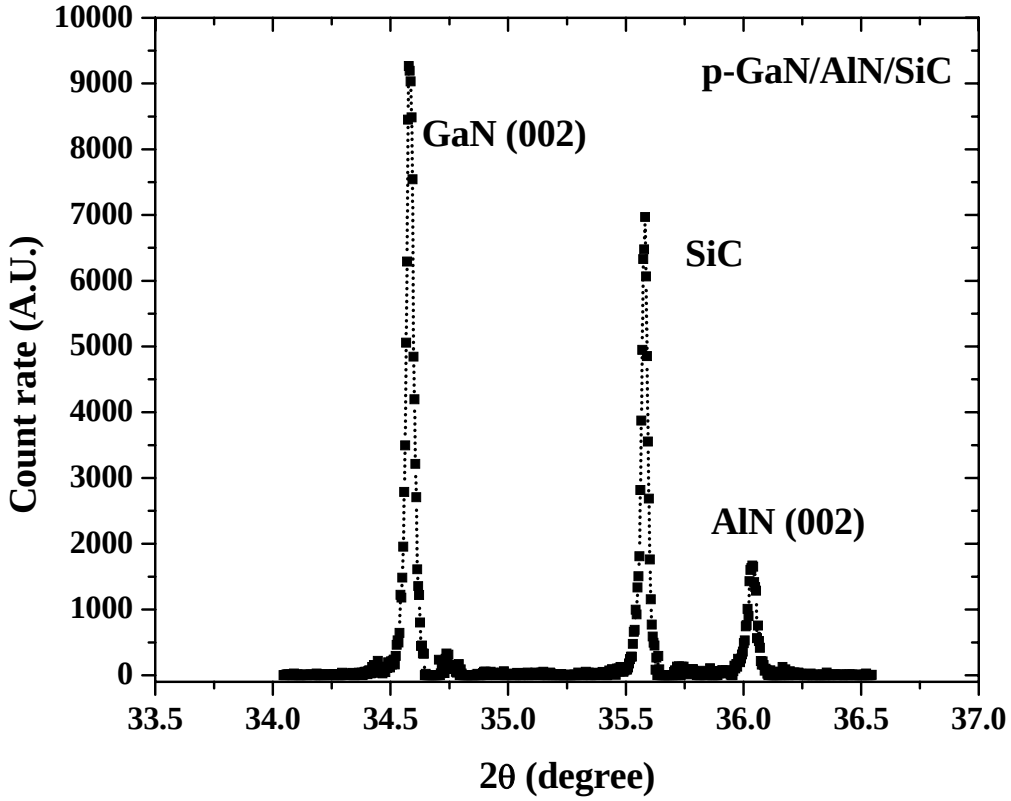

Figure 2.3 ω-2θ scan for c-plane p-GaN grown on AlN/SiC template.

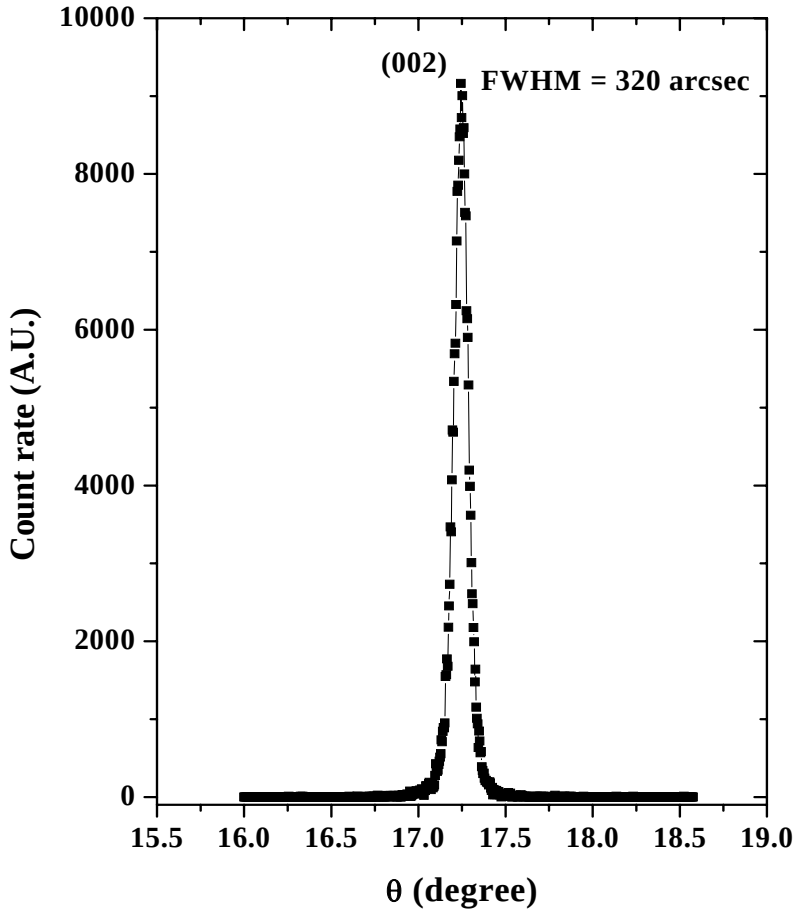

Figure 2.4 ω rocking curve for p-GaN grown on AlN/SiC.

The XRD analysis done in this work involves either symmetric or asymmetric Bragg reflections. In symmetric rocking curves, the lattice plane under investigation is parallel to the surface normal. Symmetric rocking curves have Miller index h=k=0 (e.g. [002], [004], etc.). Asymmetric rocking curves have h, k≠0. These planes are not parallel to the crystal surface normal.

Dislocations play an important role in the electronic quality of the layer. As the rocking curve width is sensitive to dislocations, XRD was used to determine the overall quality of the grown layers. In addition, the type of dislocation information that can be extracted from symmetric or asymmetric curves is different. Each type of rocking curve is sensitive to a particular type of strain in the crystal. In the case of III-nitrides, the crystal structure is usually assumed to be composed of many sub-grains in a mosaic structure [39]. The mosaic crystals can have either tilt or twist with respect to each other. The tilt describes the rotation of the mosaic out of the growth plane and the twist describes the in-plane rotation. The density of screw dislocations is correlated to the tilt of the mosaic structures [40]. The tilt of these sub-grains and thus the total screw-type dislocation density will be linearly dependent on the broadening of the symmetric rocking curve. On the other hand, edge-type and mixed dislocation density is correlated to the twist of the mosaic structure [40]. Twist manifests itself as broadening in asymmetric reflections.

2.3.4 Photoluminescence (PL)

Photoluminescence (PL) spectroscopy has been established as the premiere technique for optical spectroscopy due to its non-destructive nature and ability to yield information about optical transitions in the semiconductors. PL is a very precise tool yielding information about both fundamental optical bandedge transitions in the semiconductor and impurity or defect related transition. The set up for our PL system is shown in Figure 2.5. The laser system for PL measurements has two lasers has a solid state laser as an exciting laser for the Ti:sapphire laser and couples with a frequency quadrupled to produce 3 mW average power at 197 nm with a repetition rate of 76 MHz and pulse width of 100 femtosecond.

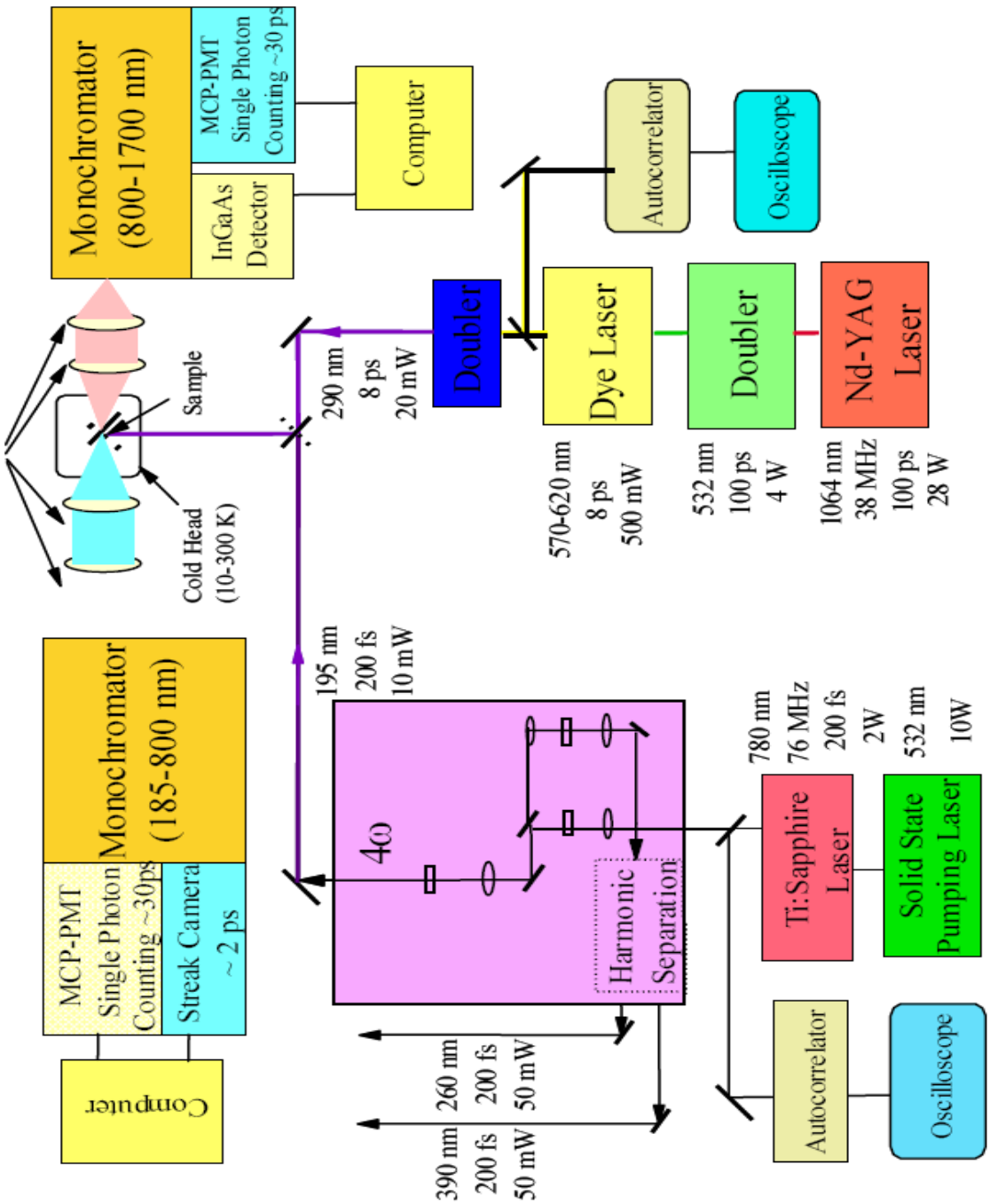

Figure 2.5 Pico-second time-resolved photoluminescence set up.

The detection system has two monochromators. One covers the range from 800 to 1700 nm and the other from 185 to 800 nm. Thus the system has the capability to scan from IR to deep UV regions. The sample is mounted on a high temperature stage with a copper cold finger in a closed-cycled helium refrigerator. The temperature range of this cryostat is between 10 and 800 K.

For PL decay lifetime measurement, either a single photon counting technique or a streak camera is used. The overall time resolution of the single photon counting system is about 30 ps. The analog video streak camera system (Hamamatsu C5680) installed in the PL system enables us to measure sample decay lifetime down to 2 ps.

2.3.5 Hall-effect measurement

The Hall effect measurement is often used to characterize the electronic properties of a crystal. This is due to the non-destructive nature of the test, the simplicity of the sample preparation, and the sensitivity of mobility and carrier concentration to changes in crystal quality due to variation of growth parameters. The turn around time for Hall effect measurement was such that we could quickly relate growth parameters to mobility and carrier concentration trends.

This information is vital for the design of electronic devices because carrier conduction and injection is an integral part of device operation. For epitaxially grown structures, the method is mostly used to study a layered structure where only one layer of known thickness is doped. For such purpose, the van-der Pauw confguration is the most commonly used configuration. In this configuration, four ohmic contacts are made on the corners of a square shaped sample. Then, a constant current is applied through two opposite corners of the sample while a strong magnetic field is applied normal to the surface of the sample. The electrons or holes making up this current experience a force field in the direction determined by the crossproduct of the carrier velocity (in the direction of current) and the magnetic field. As a result, a steady-state electric field is established in this direction, which can easily be determined by measuring the voltage drop at the two remaining contact points. This voltage is known as the Hall voltage. Detailed analysis of this method can be found in most text books on solid state physics [41]. The expression determining the carrier concentration from the Hall voltage, current flow, and magnetic field strength is:

$$n = \frac{IB}{qV} \tag{2.3}$$

where n is the electron concentration, I is the current flowing, B is the applied magnetic flux density, and V is the Hall voltage measured. Since conductivity is given by:

$$\sigma_e = -qn\mu_n \tag{2.4}$$

where σ_e is the electron conductivity and μ_n is the electron mobility. The usefulness of the Hall- effect measurement extends further if the measurement is done at varying temperatures. The temperature dependence of carrier concentration can yield information about the carrier activation energy. The temperature dependence of mobility can be used to determine predominant scattering mechanisms.

The Hall effect measurement set up is shown in Fig. 2.6. The resistivity and Hall voltage measurements are performed by a Hall-effect switching card (Keithley Model 7065). This card has selective input characteristics for high or low resistive measurements and a low electromagnetic interference power supply to maximize the isolation and minimize the noise. A current source (Keithley model 220) with a range from 0.1 pA to 101 mA and 10^{14} Ω output resistance, is used to supply the current into the sample. A picoammeter (Keithley model 485) with 0.1 pA resolution was used to measure the current flowing in the sample. The signal from the sample was fed into the card through triaxial cables to minimize the effect of leakage resistance and capacitance. A multimeter (Keithley model 196) was used to measure the Hall voltage. The system has an electromagnet (Alpha Scientific, Inc.) controlled through a DIO-200 controller (ERBTEC Engineering, Inc.) with a magnetic field of 0.462 Tesla for variable temperature measurement.

For temperature dependent measurement, the sample was attached to a copper holder mounted to the cold finger of the cryostat head which is connected with a closed-cycle He refrigerator (CTI-Cryogenics). The temperature can be varied from 10 K to 900 K. The sample temperature was monitored and controlled by a semiconductor sensor and a temperature controller (Lakeshore, Model 331).

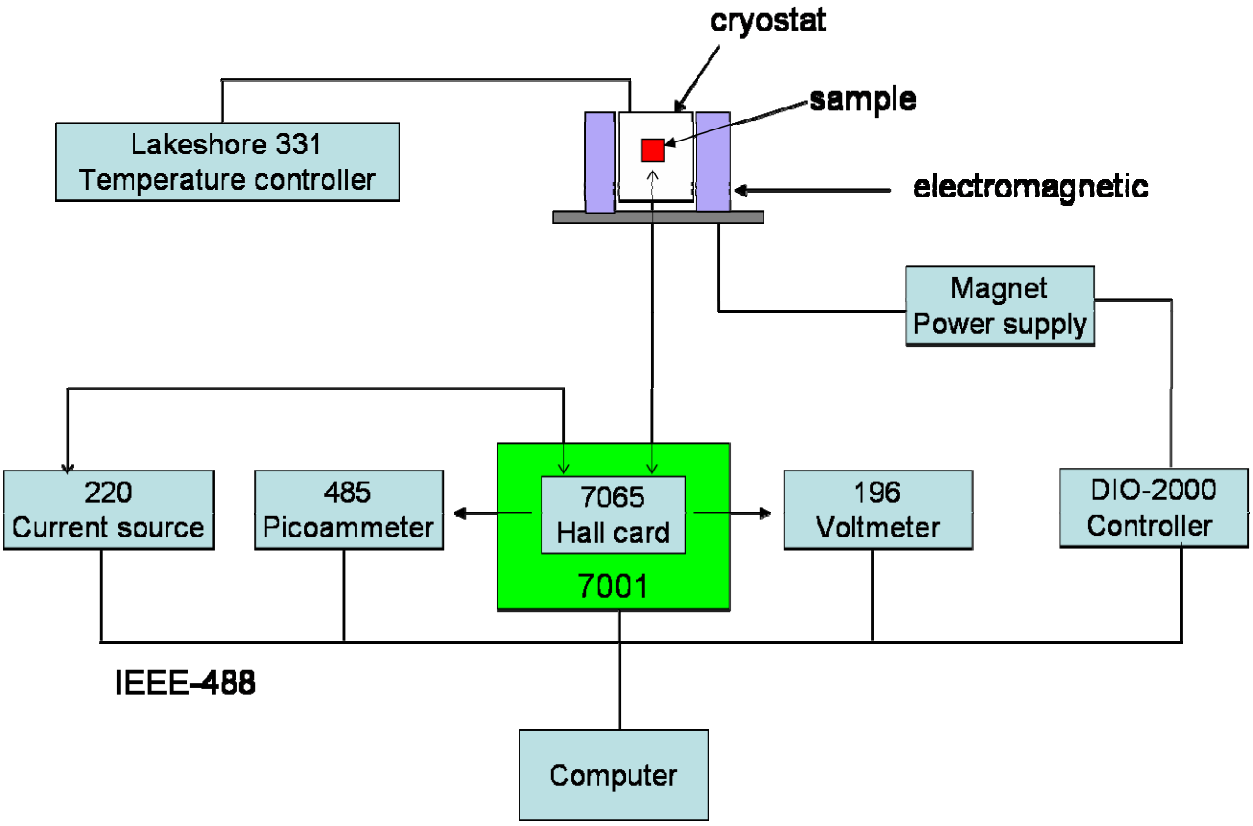

Figure 2.6 Schematic diagram of Hall-effect measurement set up.

2.3.6 Atomic force microscopy (AFM)

Atomic force microscopy (AFM) provides a means to measure the surface properties of the grown material. The AFM allows us to image the surface at atomic scale resolution and to calculate the surface roughness of the material. In the ideal case, the surface of the material will be atomically smooth with little defects observed. In practice, surface roughness is manifested due to imperfection in the substrate that propagates into the overlayer, threading defects that terminate at the surface, and non-ideal growth modes, three dimensional growth leads to island formation and high surface roughness while two dimensional growth gives a much smoother surface. The AFM can be effectively used to relate non-ideal surface conditions to changes in growth parameters.

A sharp tip mounted on a flexible cantilever is scanned over the sample surface area of a few microns square by piezoelectric drive circuitry. Measurement can be done either in contact mode or in tapping mode. In the tapping mode, the tip is vibrated at its resonant frequency and is scanned over the surface. Interaction with surface morphology causes a modulation in the vibration of the tip. The vertical motion of the tip flexes the cantilever, and the amount of deflection is detected by the reflection of a laser beam focused on the back of the cantilever. As the tip is deflected, the reflection angle of the laser is changed, which is measured by a position sensitive photodetector system. Fig. 2.7 shows the picture of the AFM used in this study.

Figure 2.7 AFM system (Q-Scope 250 model from Quesant Co.).

2.3.7 Scanning Electron Microscopy (SEM)

Scanning electron microscopy (SEM) is utilized to study morphological information on a surface at extremely high magnifications. Our scanning electron microscope (SEM) is a LEO 440 model with accelerating voltage up to 40 kV. It is also coupled with Oxford INCA Energy Dispersive X-ray Spectrometer (EDX). Fig. 2.8 shows a photograph of the SEM system.

Electrons are extracted from electron gun by strong electric field. The electrons in the beam are then accelerated by high voltage. When electrons hit the sample, secondary electrons are generated by knocking electrons out of atoms in the sample upon impact. The secondary electrons are then collected by electron detector. The electron beam rasters within the area of observation. From the data collected by the detector, a secondary electron image can be displayed or captured. Fig. 2.9 shows SEM image of an AlN epilayer.

EDX is a standard procedure for identifying elemental composition of specimen within area as small as a few cubic micrometers. When a material is bombarded by electrons in an electron beam instrument, such as SEM, if the electron energy is high enough to knock out a core electron from an atom in the specimen, another electron from the outer shell of the atom can jump down to fill the empty states and release the extra energy by emitting an x-ray photon. Characteristic x-ray spectra can be obtained from the specimen because the position and intensity of the x-ray peaks are element dependent. So the composition of specimen can be determined.

Figure 2.8 The SEM system.

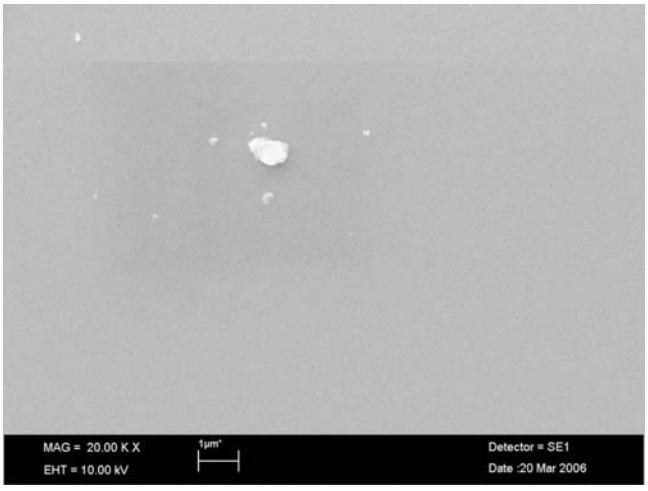

Figure 2.9 SEM image of a representative AlN epilayer.

CHAPTER 3 - Experimental results and discussions

3.1 Correlation between growth polarity and material quality of high Al-content AlGaN alloys

AlGaN alloys have the capability of tuning the direct band gap in a large energy range, from about 3.4 to 6.1 eV, which makes them very useful for ultraviolet (UV) and deep UV (DUV) optoelectronic device applications. Although recent progress has led to the realization of several operational DUV devices such as light emitting diodes (LEDs) operating at wavelengths < 300 nm [42-49], high performance DUV optoelectronic devices including high power LEDs, avalanche photodetectors, and laser diodes working at $\lambda \leq 280$ nm have not been realized. Two outstanding issues resulting in poor device grade material are a high dislocation density and a low conductivity (or doping efficiency) in high Al-content AlGaN alloys. One of the major difficulties in obtaining highly conductive *n*-type high Al-content AlGaN alloys is due to the effect of compensation of electrons by cation vacancies $(V_{III})^{3-}$ and their complexes. Suppressing such intrinsic defects could significantly improve the conductivity and material quality of high Al-content AlGaN alloys [49-55]. The presence of high dislocation densities in III-nitrides generally translates to a high density of native defects that act as self-compensating centers for substitutional doping [52-56]. Therefore, further understanding the effects that influence the structural, electrical and optical properties, and identifying growth methods for obtaining high Al-content AlGaN alloys with improved material quality are essential to DUV optoelectronic device applications based on these materials. An important growth parameter that affects the properties of III-nitrides is the growth polarity. The importance of the growth polarity effects on the material properties of InGaN and GaN films has been previously investigated [57-61]. However a systematic study pertaining the growth polarity effects on the material quality of high Al-content AlGaN alloy has not been carried out.

In this chapter, high Al-content $Al_xGa_{1-x}N$ (x~0.8) epilayers were grown on sapphire substrates by metal organic chemical vapor deposition (MOCVD). Various characterization techniques were employed to probe their structural, optical and impurity properties. Wet

chemical etching with potassium hydroxide (KOH) was employed to confirm the polarity of the samples. X-ray diffraction (XRD) to determine the Al contents and the crystalline quality, while atomic force microscopy (AFM) to study the surface morphology. A variable temperature (up to 900 K) Hall effect measurement was utilized to assess the electrical properties and photoluminescence (PL) emission spectroscopy was employed to investigate the optical properties. The deep UV PL spectroscopy system consists of a frequency quadrupled 100 femtosecond Ti: Sapphire laser with an average power of 3 mW and repetition rate of 76 MHz at 196 nm and a 1.3 m monochromator with a detection capability ranging from 185 – 800 nm [62]. Secondary ion mass spectrometry (SIMS) was carried out by Evans Analytical Group to probe the influence of the growth polarity on the incorporation of unintentional impurities.

Un-doped high Al-content $Al_xGa_{1-x}N$ epilayers were grown on c-plane sapphire substrates by MOCVD. The growth temperature and pressure were 1150 ^{0}C and 80 Torr, respectively. Trimethylgallium (TMGa) and Trimethylaluminum (TMAl) were used as the metalorganic sources. The N-polarity was established by nitriding the sapphire substrate at 1160 ^{0}C for 70 seconds prior to the epi-growth, while Al-polarity was initiated by growing on clean sapphire substrate without nitridation [59-61]. A 1μm un-doped AlN epilayer was first grown to serve as a template, and followed by the growth of a 0.5 μm un-doped $Al_xGa_{1-x}N$ epilayer. The polarities of $Al_xGa_{1-x}N$ epilayers were further confirmed by a KOH based etching process [63-65]. The surface morphology of an $Al_xGa_{1-x}N$ ($x \sim 0.81$) epilayer with Al-polarity was smooth with a root mean square (RMS) of surface roughness of about 1 nm. In contrast, the surface morphology of an $Al_xGa_{1-x}N$ ($x \sim 0.8$) epilayer with N-polarity was rough with a RMS value of about 9 nm, as shown in Fig.3.1. Although the results here are for high Al-content AlGaN alloys, they follow similar trends determined for GaN epilayers [65, 66].

.

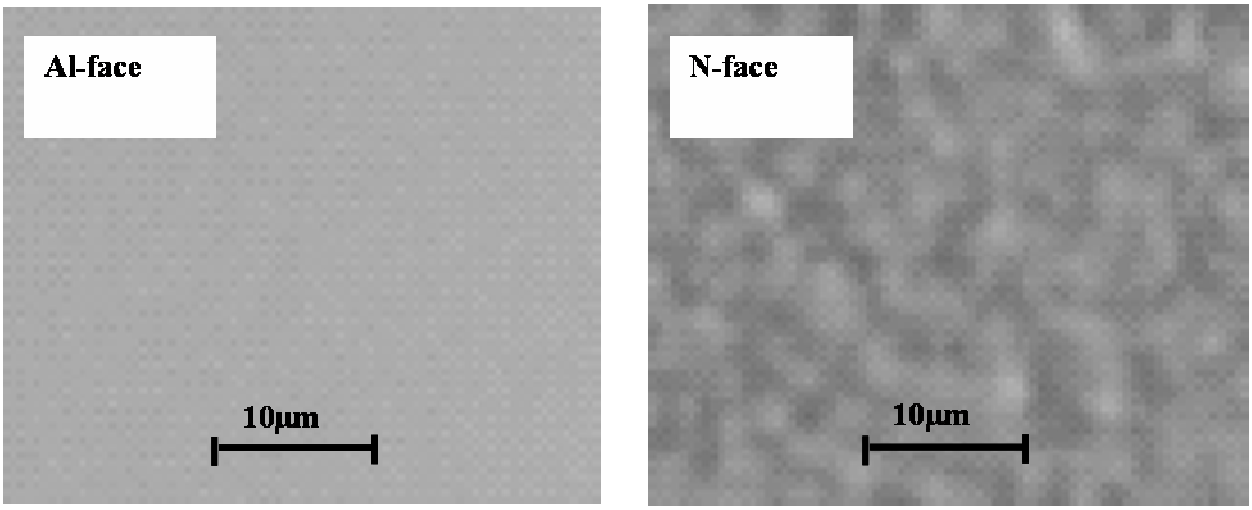

Figure 3.1 Optical microscopy images of Al- and N-polar $Al_xGa_{1-x}N$ (x ~ 0.8) epilayers. The surface morphology measured by AFM for the Al-polar sample is smooth (RMS = 1 nm) and for the N-polar is grainy (RMS = 9 nm).

XRD rocking curves of the symmetric (002) and asymmetric (102) reflection peaks in $Al_xGa_{1-x}N$ (x ~ 0.8) epilayers are shown in Figures 3.2 and 3.3 respectively, for two representative samples. A full width at half maximum (FWHM) as low as 147 arcsec was obtained for the sample with Al-polarity in comparison with 475 arcsec for the sample with N-polarity. Furthermore, FWHM of the XRD rocking curves of the asymmetric (102) reflection peak of the Al-polar sample (1300 arcsec) is about 70% of that of the N-polar sample (1800 arcsec). The XRD results thus confirm that $Al_xGa_{1-x}N$ (x ~ 0.8) epilayers with Al-polarity have a smaller dislocation density and a higher crystalline quality than those with N-polarity.

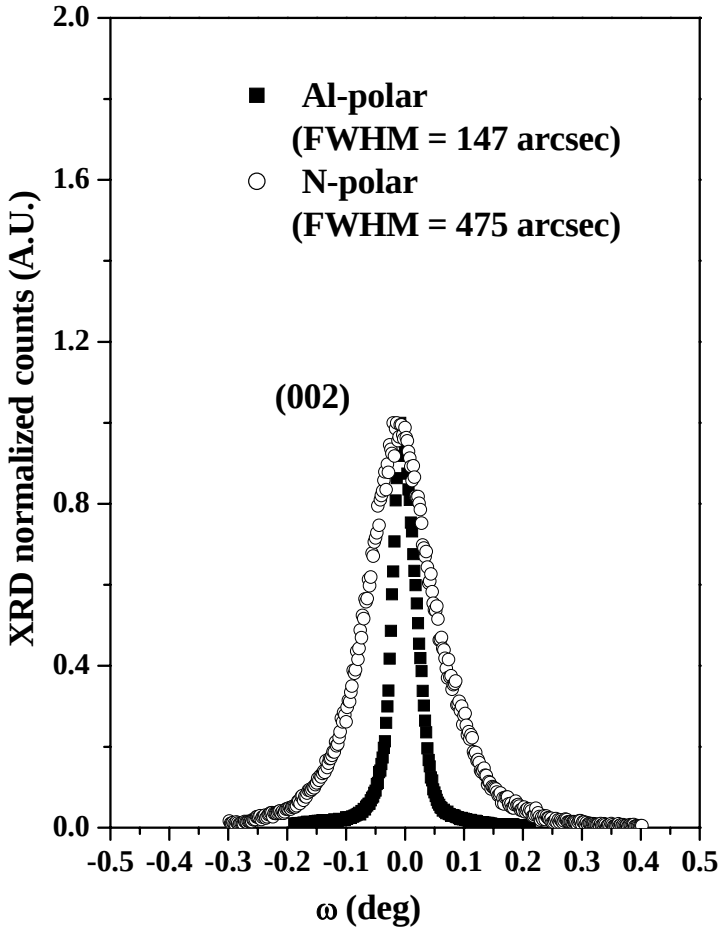

Figure 3.2 Rocking curves of the symmetric (002) reflection peaks in N-polar and Al-polar $Al_xGa_{1-x}N$ (x ~ 0.8) epilayers. Full width at half maximum (FWHM) is 147 (475) arcsec for Al- (N-) polar sample.

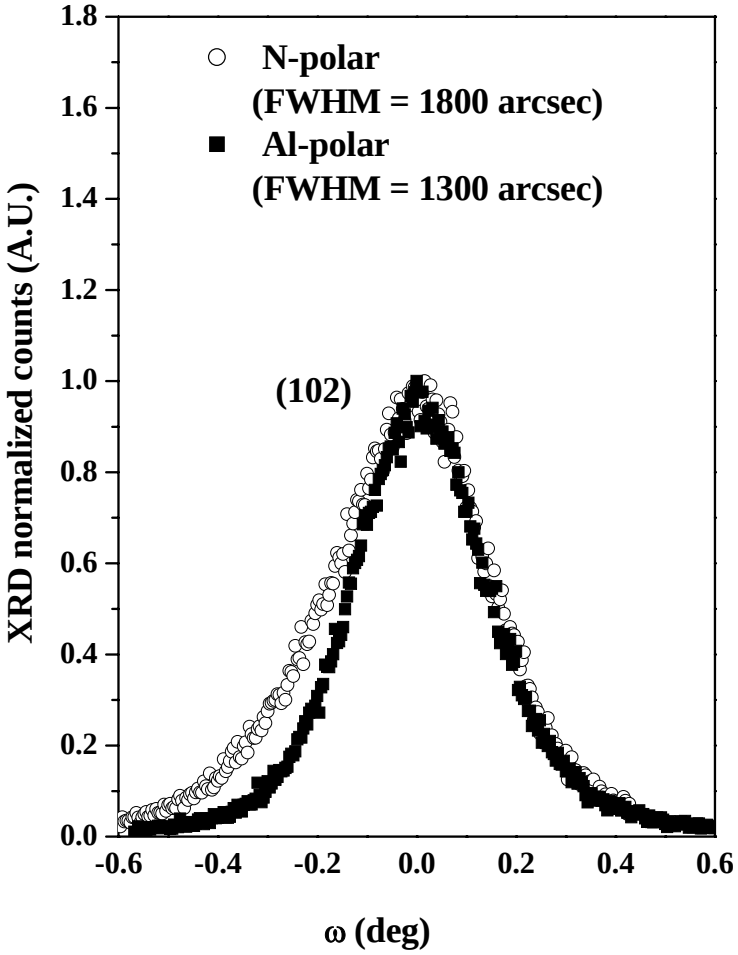

Figure 3.3 Rocking curves of the asymmetric (102) reflection peaks in N-polar and Al-polar $Al_xGa_{1-x}N$ (x ~ 0.8) epilayers. Full width at half maximum (FWHM) is 1300 (1800) arcsec for Al (N)-polar sample.

To probe the optical qualities, we performed PL measurements on these epilayers. Fig. 3.4 compares the low temperature (10 K) PL spectra of two AlGaN epilayers with Al- and N-polarities. The dominant band edge emission peaks of these spectra are due to the localized exciton recombination in the AlGaN epilayers [67, 68]. In addition to the band edge emission peak, the emission spectrum of the N-polar $Al_xGa_{1-x}N$ ($x \sim 0.8$) epilayer also comprises a deep level impurity transition, which has been identified previously, and is assigned to the recombination between shallow donors and cation vacancy complexes with one-negative charge, $(V_{III}\text{-complex})^{1-}$ (Fig. 3.5) [69]. Due to the presence of the $(V_{III}\text{-complex})^{1-}$ related emission, the intensity of the band edge emission in N-polar sample is about 5 times lower than that in Al-polar sample. The binding energy of $(V_{III}\text{-complex})^{1-}$ in $Al_xGa_{1-x}N$ ($x \sim 0.8$) deduced from the PL spectral peak position is about 1 eV [69]. The presence of a higher concentration of the (V_{III}-complex) is partly related to the lower crystalline quality of the N-polar materials.

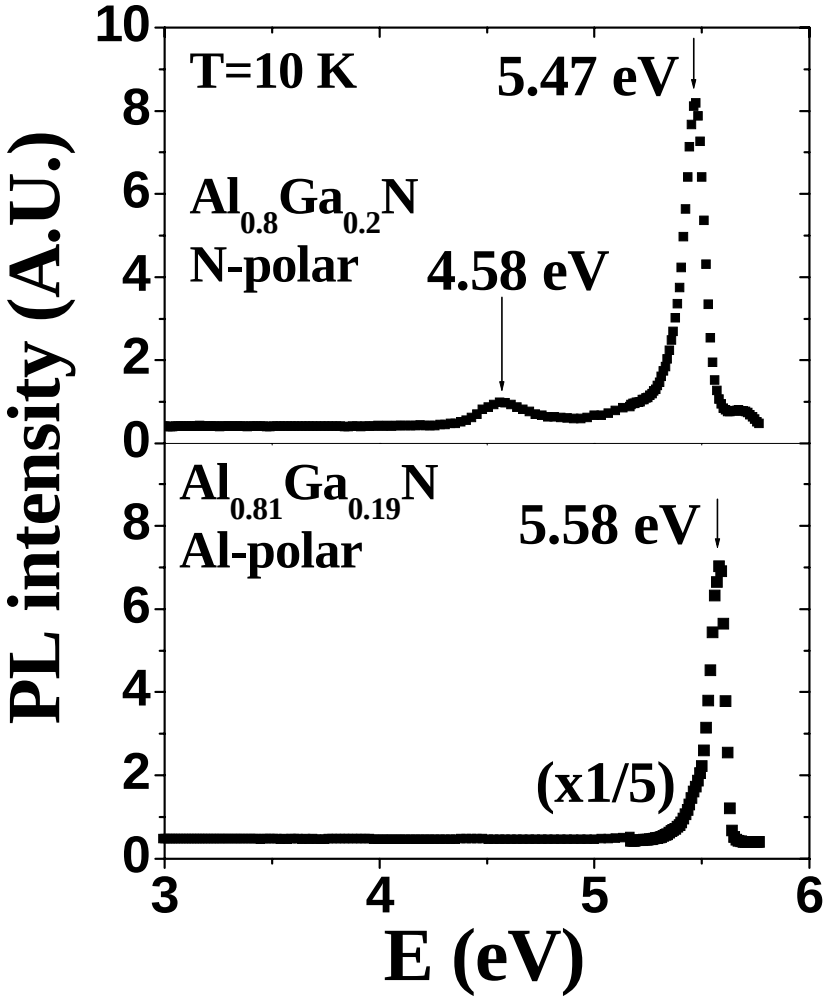

Figure 3.4 The low temperature (10 K) PL spectra of N-polar and Al-polar $Al_xGa_{1-x}N$ (x~ 0.8) epilayers. A deep level impurity transition related with the presence of cation complexes with one-negative charge, $(V_{III}\text{-complex})^{1-}$ is observable in the N-polar sample.

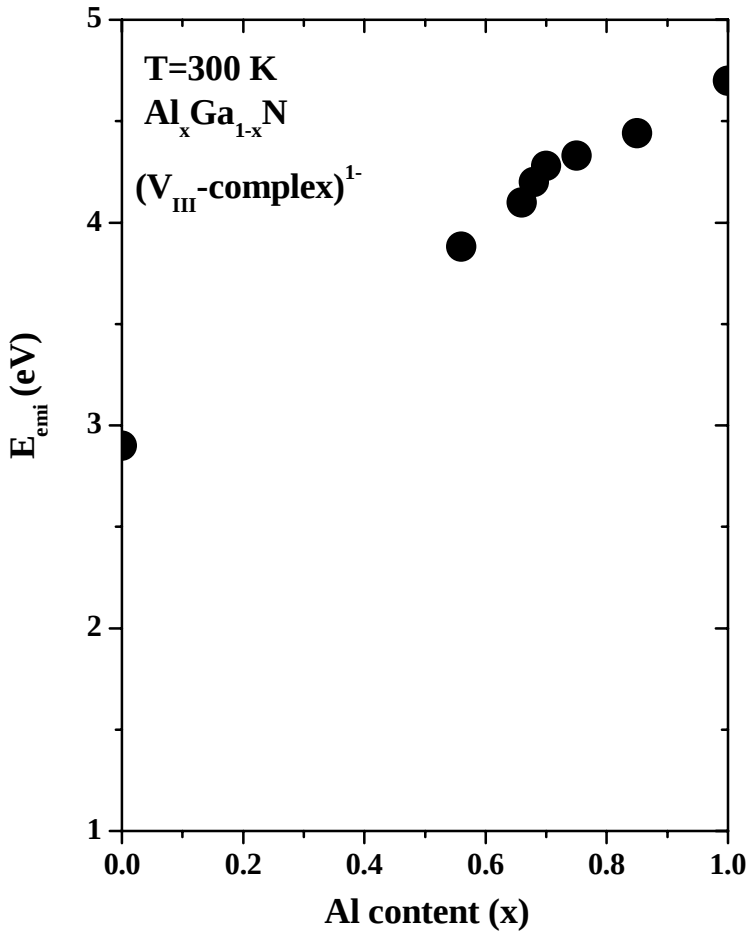

Figure 3.5 The PL spectral peak position of the $(V_{III}\text{-complex})^{1-}$ related impurity transition in $Al_xGa_{1-x}N$ alloys as a function of x.

Hall-effect measurements were attempted in oredr to probe the electrical properties of $Al_xGa_{1-x}N$ (x ~ 0.8) epilayers. However, the resistivity of Al-polar samples was too high to be measurable at values of T up to 900 K. Fig. 3.6 shows the Arrhenius plot of the resistivity (ρ) of an $Al_{0.8}Ga_{0.2}N$ epilayer with N-polarity. The resisitivity decreases with increasing temperature. The solid line is the least squares fit of data according to the following equation:

$$\rho(T) = \frac{\rho_0}{1 + e^{\frac{-E_A}{KT}}} \tag{3.1}$$

where ρ(T) is the resistivity at temperature T, and E_A is the activation energy. The fitted value of the activation energy (E_A) is about 1.00 ± 0.01 eV, which is close to the binding energy of $(V_{III}\text{-complex})^{1-}$ deduced from the PL spectral peak positions in Fig. 3.4.

Figure 3.7 shows the SIMS profiles of oxygen and carbon impurities in Al- and N-polar samples. Comparing the results, oxygen and carbon impurities are incorporated at almost two orders of magnitude higher into the N-polar sample. This could be another cause for the higher concentration of V_{III} and/or V_{III}-complex in N-polar materials.

In summary, un-doped high Al-content $Al_xGa_{1-x}N$ epilayers were grown on sapphire substrates by MOCVD. The growth polarity strongly influences the surface morphology, structural, optical, and electrical properties of high Al-content AlGaN epilayers. The Al-polar $Al_xGa_{1-x}N$ epilayers possess a better surface morphology and crystalline quality compared with those of N-polar $Al_xGa_{1-x}N$ epilayers. Low temperature PL spectra of Al-polar $Al_xGa_{1-x}N$ epilayers exhibit only the band edge transition, while, the PL spectra of N-polar $Al_xGa_{1-x}N$ epilayers comprise an additional deep level impurity transition, which was assigned to the recombination between a shallow donor and $(V_{III}\text{-complex})^{1-}$. The energy level of $(V_{III}\text{-complex})^{1-}$ was obtained to be around 1 eV from the temperature dependence of resistivity and is close to the value deduced from the PL spectral peak positions. Unintentional impurities related to C and O are more readily incorporated into N-polar AlGaN epilayers. Thus, like GaN, the growth polarity is a key parameter to obtain smooth and low defect density high-Al-content AlGaN epilayers.

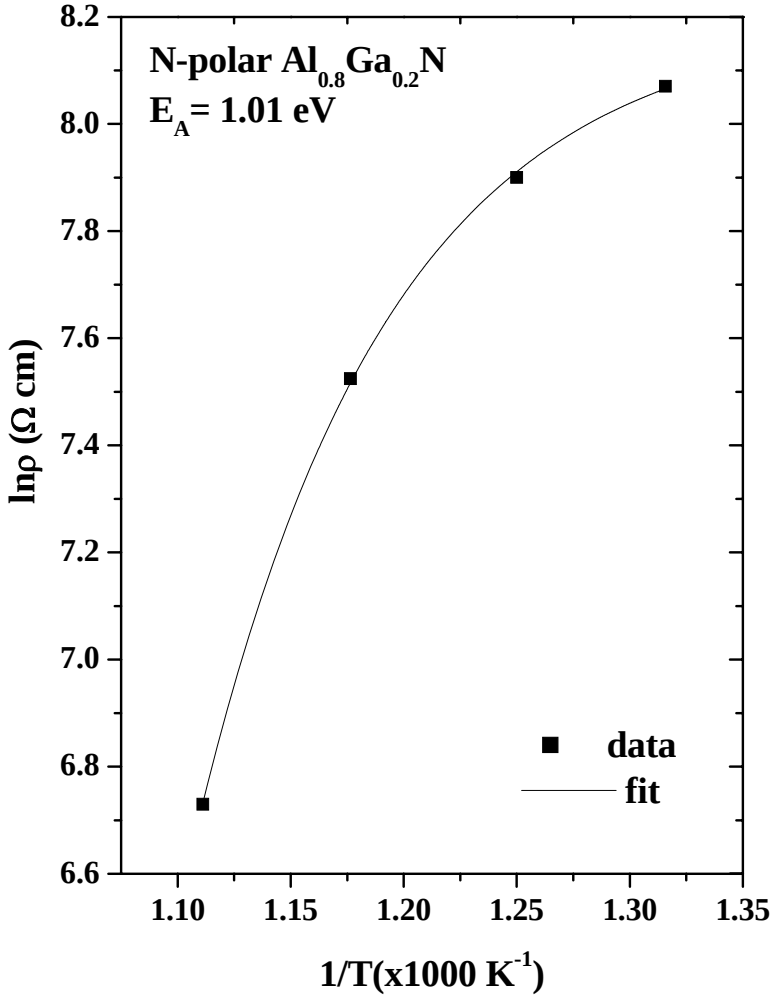

Figure 3.6 The Arrhenius plot of resistivity (ρ) obtained for the N-polar $Al_xGa_{1-x}N$ (x ~ 0.8) epilayers. The solid line is the least-squares fit of data with Eq. (3.1). The fitted value of the activation energy (E_A) is 1.00 ± 0.01 eV, which is believed to be the energy level of cation vacancy complexes with one-negative charge in $Al_xGa_{1-x}N$ (x ~ 0.8) epilayers.

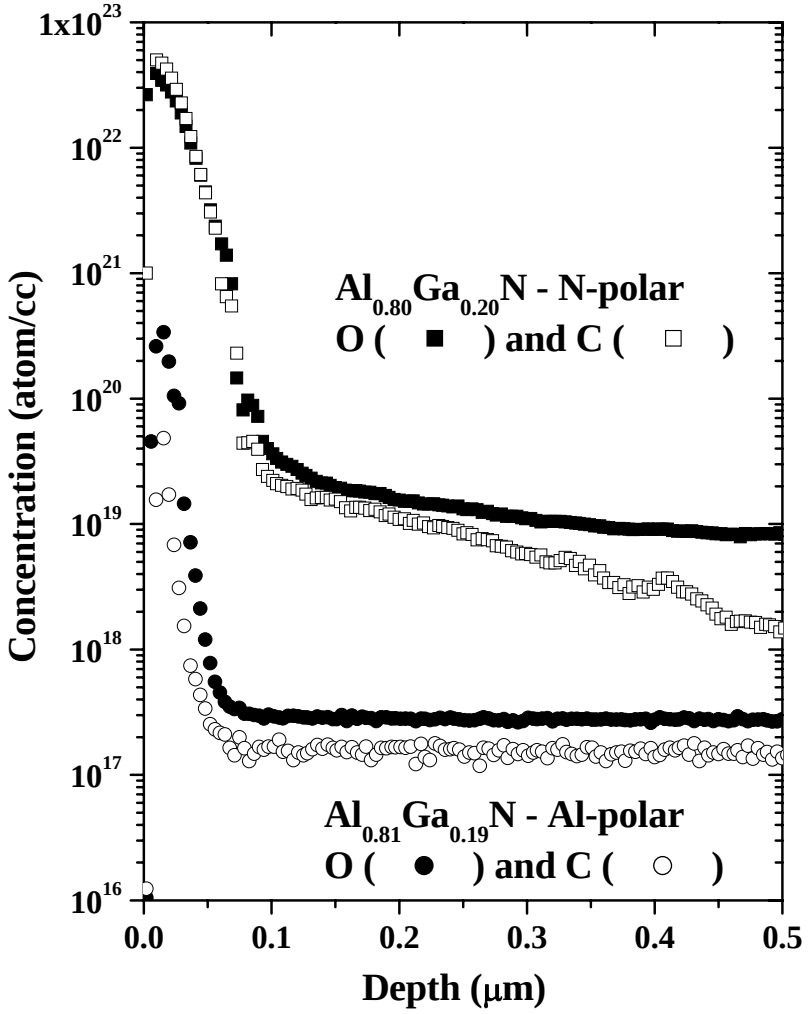

Figure 3.7 Secondary ion mass spectrometry (SIMS) profiles of oxygen and carbon impurities in Al- and N-polar $Al_xGa_{1-x}N$ (x ~ 0.8) epilayers.

3.2 Growth and photoluminescence studies of c-plane Al-rich AlN/$Al_xGa_{1-x}N$ quantum wells

Deep ultraviolet (UV) emitters and detectors operating in the 200 – 340 nm wavelength range are important devices for many applications including water purification, bio-chemical agent detection, medical research/health care, and high-density data storage [70]. Al-rich AlGaN alloys have the capability of emitting at short wavelengths down to 210 nm, which makes them very useful for these applications. As demonstrated by light emitting diodes (LEDs), laser diodes (LDs), and electronic devices, many III-nitride based devices must take advantages of quantum well (QW) structures in order to achieve optimal device performance. To realize deep UV emission ($\lambda < 280$ nm) Al-rich AlGaN based QWs are required. Recently, several groups have studied Al-rich AlGaN-based emitters to obtain UV emission of wavelengths below 300 nm [71-77]. However, the quantum efficiency (QE) of these deep UV emitters is still very low. Systematic studies of Al-rich $Al_xGa_{1-x}N$ alloys and AlN/$Al_xGa_{1-x}N$ QWs are needed in order to probe the underlying mechanisms and the layer structural designs required to provide improved QE.

In this study, a set of AlN/$Al_{0.65}Ga_{0.35}N$ QWs with well width (L_w) varying from 1 to 3 nm and a fixed barrier width of 10 nm have been grown by metalorganic chemical vapor deposition (MOCVD). Low temperature (10 K) deep UV PL emission spectroscopy has been employed to probe the L_w dependence of the optical properties. Our results revealed that the highest QE could be obtained in QWs with L_w between 2 and 2.5 nm. The estimated value of the polarization fields (piezoelectric and spontaneous fields) induced in the well regions was found to be around 4 MV/cm, which agrees well with the calculations. A linear relationship between the emission line width and L_w has also been observed.

AlN/$Al_xGa_{1-x}N$ ($x \sim 0.65$) QW samples were grown on sapphire (001) substrates by MOCVD. The growth temperature and pressure were 1150 ^{0}C and 100 Torr, respectively. For each of the five samples, prior to the growth of $Al_{0.65}Ga_{0.35}N$ QW, a thin AlN buffer layer and a 1-μm undoped AlN epilayer were grown on the sapphire substrate. It was then followed by the growth of $Al_{0.65}Ga_{0.35}N$ QW and a 10 nm AlN barrier. The targeted L_w of these samples were 1, 1.5, 2, 2.5, and 3 nm. The barrier and well widths were determined by the growth rates of the

AlN and $Al_xGa_{1-x}N$ epilayers. The samples were mounted on a low temperature (10 K) stage with a cold finger in a closed–cycle helium refrigerator. The deep UV PL spectroscopy system consists of a frequency quadrupled 100 femtosecond Ti: Sapphire laser with an average power of 3 mW and repetition rate of 76 MHz at 196 nm and a 1.3 m monochromator with a detection capability ranging from 185 – 800 nm [62].

The continuous wave (cw) PL spectra of these five samples measured at 10 K are shown in Fig. 3.8. The dominant PL emission lines are due to the localized exciton recombination in the AlGaN QW regions [78]. With respect to the band edge transition at 4.969 eV in $Al_{0.65}Ga_{0.35}N$ epilayers, the PL peak energy is red-shifted for QWs with L_w = 2.5 and 3 nm and blue-shifted for QWs with L_w = 1, 1.5, and 2 nm. This indicates that the PL peak energy is defined by the quantum confinement as well as by the induced fields (piezoelectric and spontaneous fields) along the growth direction [79]. In order to find out the polarization fields in the QWs, we calculate emission peak positions for QWs with different well widths. The calculation performed by our collaborator, Dr. Chow Weng at Sandia National laboratories. The calculation begins with the determination of quantum-well band structure properties by simultaneously diagonalizing the k.p Hamiltonian and solving Poisson's equation [80]. The input parameters are the bulk material parameters, where for AlGaN, we use the weighted averages of the AlN and GaN values. Using the quantum-well band structure information, we numerically solve the semiconductor Bloch equations for the steady-state microscopic polarization [81]. The many-body effects appear as carrier density dependences in the transition energy and Rabi frequency. Carrier-carrier correlations, which lead to screening and dephasing, are treated at the level of quantum kinetic theory in the Markovian limit. The steady state polarization at an input laser field and carrier density (assuming quasi-equilibrium condition) gives the linear absorption spectrum. The corresponding spontaneous emission spectrum is obtained using phenomenologi- cal relationship that relates the spontaneous emission and absorption spectra [82]. The emission peak energies are then extracted from the spectra.

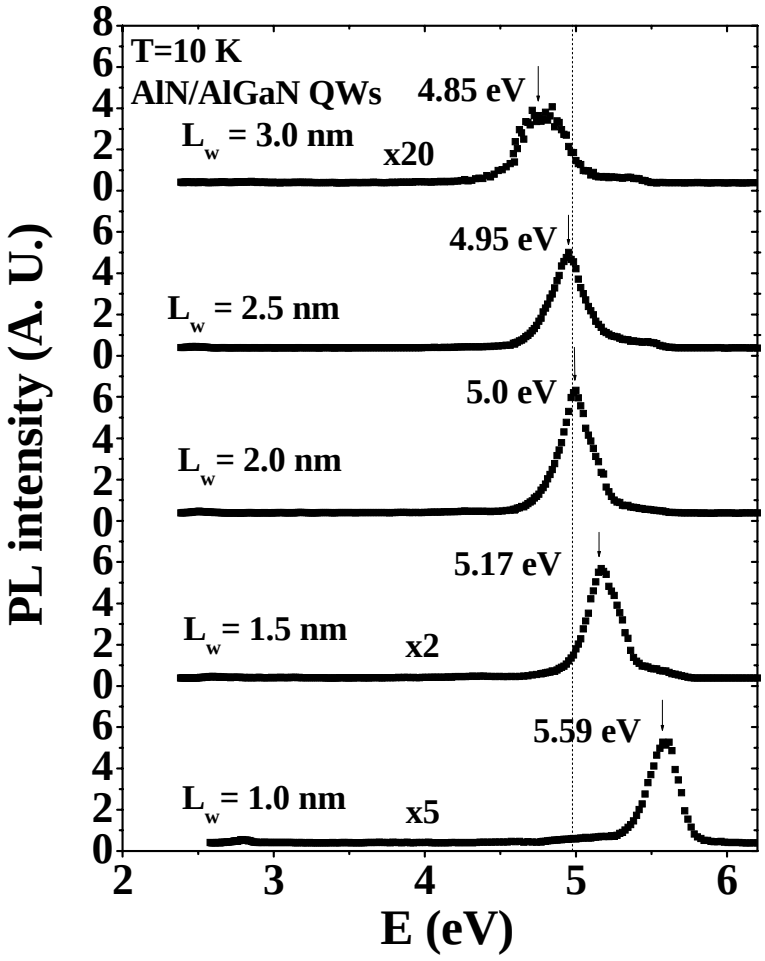

Figure 3.8 Low temperature (10 K) PL spectra of AlN/$Al_{0.65}Ga_{0.35}N$ QW samples with well width varying from 1 to 3 nm and a fixed barrier width of 10 nm. The vertical dashed line represents the emission peak position of $Al_{0.65}Ga_{0.35}N$ epilayers.

Fig. 3.9(a) plots the PL spectral peak position (E_p) as a function of L_w. The curve in Fig. 3.9(b) is the theoretical curve of E_p as a function of L_w from which we deduce the value of the polarization fields to be around 4 MV/cm. The value of the polarization field (F) in the well region can also be calculated using the equation:

$$F = \frac{L_b(P_{tot}{}^b - P_{tot}{}^w)}{[\varepsilon_0(L_w\varepsilon_b + L_b\varepsilon_w)]} \tag{3.2}$$

where $\varepsilon_{b,w}$ is the relative dielectric constant of the barrier and the well materials, $P_{tot}{}^{b,w}$ is the total polarization (piezoelectric plus spontaneous) in barrier and well, L_b is the barrier width [79]. The piezoelectric polarization can be calculated with the equation:

$$P_{piezo} = -(2e_{31} - 2\frac{c_{13}e_{33}}{c_{33}})\varepsilon_{xx} \tag{3.3}$$

where e_{ij} , where i,j = {1,2,3}, are the piezoelectric constants, c_{ij}, where i,j = {1,2,3}, are the elastic constants and ε_{xx} is the in plane strain [79]. To calculate the value of the polarization fields in the $Al_xGa_{1-x}N$ well, we used the parameters given in Ref. 83 assuming a linear relationship between the GaN and AlN values to extract the values for $Al_xGa_{1-x}N$ alloys. The calculated value of the polarization fields from Eq. (3.2) ranges between 3.96 and 3.37 MV/cm depending on the well width, which is in reasonable agreement with the deduced value.

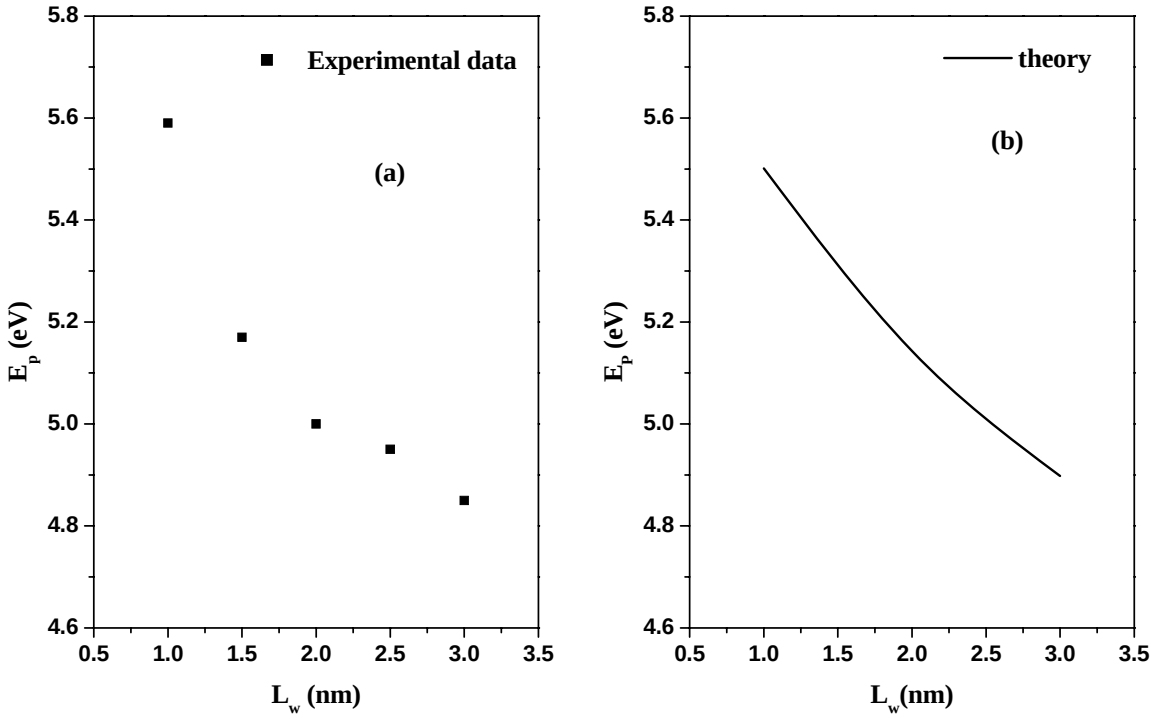

Figure 3.9 (a) PL emission energy peak position, E_p vs well width, L_w for $AlN/Al_{0.65}Ga_{0.35}N$ QWs measured at 10 K. (b) The calculated E_p as a function of L_w, performed by our collaborator, Dr. Chow Weng at Sandia National laboratories.

The integrated PL emission intensity versus L_w measured at 10 K for these QWs is plotted in Fig. 3.10, which shows that the highest QE is achieved when L_w is between 2 and 2.5 nm. The PL intensity depends strongly on L_w. The reason for the rapid reduction of the emission intensity with the increase of L_w can be attributed to the reduction of the radiative recombination rate (or QE) due to the polarization fields in the well, which increases the spatial separation of the electron and hole wave functions with increasing L_w [84,85,86]. On the other hand, the decreased emission intensity with L_w (for small well width $L_w < 2$ nm) is due to enhanced carrier leakage into the barrier region [84]. From Fig. 3.8, the emission line widths of these $AlN/Al_xGa_{1-x}N$ QWs are fairly large. A similar trend was observed for GaN/InGaN QWs. The broad line width of GaN/InGaN has been explained in terms of In compositional fluctuation [87, 88]. For $AlN/Al_xGa_{1-x}N$ QWs in addition to compositional fluctuation, polarization fields have to be taken into account to analyze the emission line width of the QWs. The effective transition energy in QWs under the influence of polarization fields is given by:

$$E = E_g + E_{con} - eFL_w, \tag{3.4}$$

where E_g is the bandgap of the well material, E_{con} is the confinement energy, and eFL_w is a factor accounting for the polarization fields effect [89]. In the first order approximation, the variation of the emitted photon energy (i.e. the line width), is given by the sum of the fluctuations in the bandgap of the well material, the confinement energy, the polarization fields, and L_w,

$$\delta E = \delta E_g + \delta E_{con} + eL_w\delta F + eF\delta L_w. \tag{3.5}$$

Neglecting the variation of the confinement energy δE_{con} in cases where the QWs with well widths larger than the Bohr radius of excitons (i.e. about 1.3 nm), Eq. (3.5) can be written in terms of the dependence on L_w as follows:

$$\delta E = (\delta E_g + eF\delta L_w) + (e\delta F)L_w. \tag{3.6}$$

This equation reveals a linear relation between the line width and L_w with the assumption that the well width fluctuation (δL_w) is fixed for all QWs and is about 1 monolayer (i.e. ~ 0.5 nm).

Fig. 3.11 shows the variation of the full width at half maximum (FWHM) of the emission spectra of $AlN/Al_{0.65}Ga_{0.35}N$ QWs with L_w measured at 10 K. The FWHM increases linearly with increasing L_w. The solid line is a linear fit to the experimental data using Eq. (3.6). A localization energy around 100 meV is extracted which is consistent with the previously reported values in $Al_xGa_{1-x}N$ epilayers [90]. Assuming the well width fluctuation is 1-monolayer (i.e. ~ 0.5 nm), another 35 meV is extracted. Thus the large emission line width of the $AlN/Al_xGa_{1-x}N$ QWs can be explained well by the effects of alloy fluctuation and polarization fields.

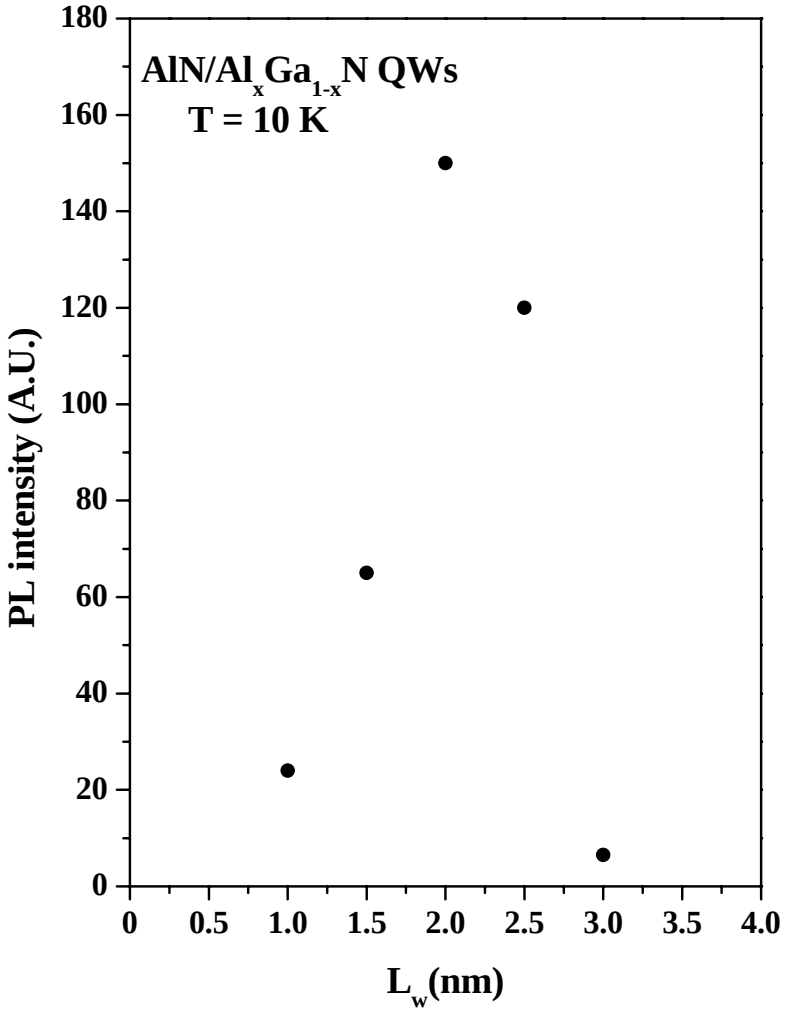

Figure 3.10 Integrated PL emission intensity vs well width of AlN/$Al_{0.65}Ga_{0.35}N$ QWs measured at 10 K.

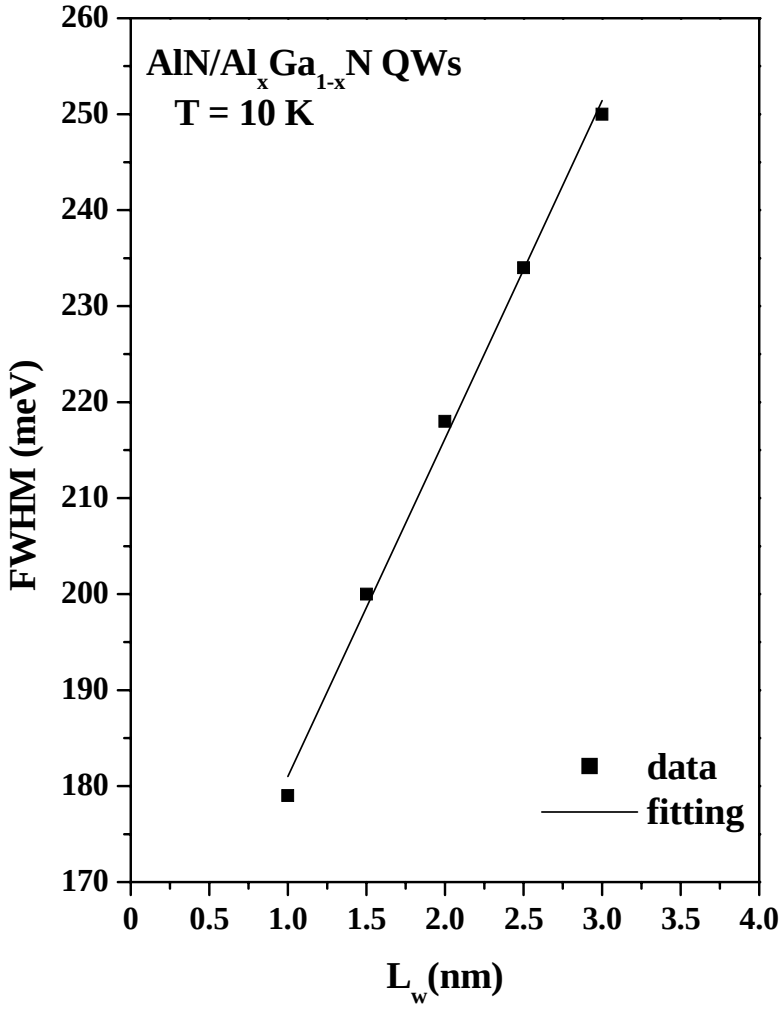

Figure 3.11 The variation of the full width at half maximum (FWHM) of the PL emission spectra with well width for $AlN/Al_{0.65}Ga_{0.35}N$ QWs measured at 10 K. The solid line is the linear fit to the experimental data.

To find which is more effective, varying the L_w or varying the Al-content (x) of QW, we grew a set of samples with varying x and a fixed well width of L_w = 1.5 nm. Figure 3.12 shows the low temperature (10 K) PL spectra for $AlN/Al_xGa_{1-x}N$ QW (L_w = 1.5 nm) with x varying from 0.70 to 0.85. The emission peak position increases with increasing x. The FWHM of the PL emission decreases with increasing x, which is due to reduction of localization energy with increasing x for x > 0.70 [90].

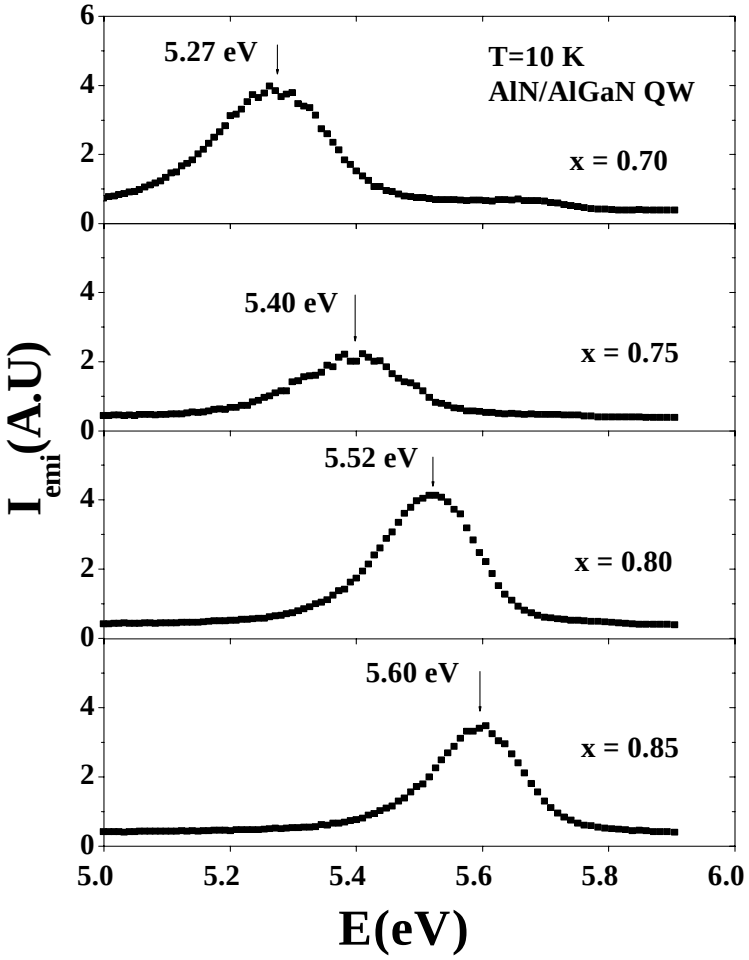

Figure 3.12 Low temperature (10 K) PL spectra of $AlN/Al_xGa_{1-x}N$ QW samples with different Al content. The well width (barrier) is 1.5 (10) nm, respectively, and x varies from x = 0.7 to x = 0.85.

The findings of this chapter, and the previous one, were employed in the design and growth of deep UV LED ($\lambda < 300$ nm) structures. The active region of a LED structure is based on altra-thin AlGaN/AlGaN MQWs. Since the devices were deposited onto c-plane sapphire substrates, it was necessary to use thin wells to reduce the Quantum-confined Stark Effect. In this way the reduction in the luminescence intensity and its red-shift can be minimized. The deep UV LEDs were grown on AlN/sapphire templates by MOCVD. The output power and forward voltage of the device show strong dependence on the thickness of the AlN template. Silicon doped $Al_xGa_{1-x}N$ is a key material in UV LED structures. It is not only the n-type contact layer that supplies electrons to the active region, but it is also a template for the rest of the LED structure and therefore must have high crystalline quality. However, lattice-mismatch iduced strain between AlN template and the AlGaN causes cracks and dislocations. The strain depends on the crystal orientation, the thickness, and the chemical composition of the epitaxial layers [91,92]. Strain engineering can be accomplished by superlattice (SL) layers, low temperature (LT) AlN interlayers, homoepitaxial substrates, and non-polar substrates [93-96]. Among these approaches, $AlN/Al_{0.8}Ga_{0.2}N$ SLs are used in our deep UV LED structures. An additional function of SL layers is to serve as a dislocation filter. The growth of the Si-doped $Al_{0.7}Ga_{0.3}N$ epilayer was followed by AlGaN/AlGaN MQW active region and followed by the Mg-doped $Al_{0.7}Ga_{0.3}N$ electron blocking layer. The structure was then completed with p-$Al_{0.1}Ga_{0.9}N$ and p-GaN layers. A schematic diagram of the deep UV LED layer structure is shown in Fig. 3.13.

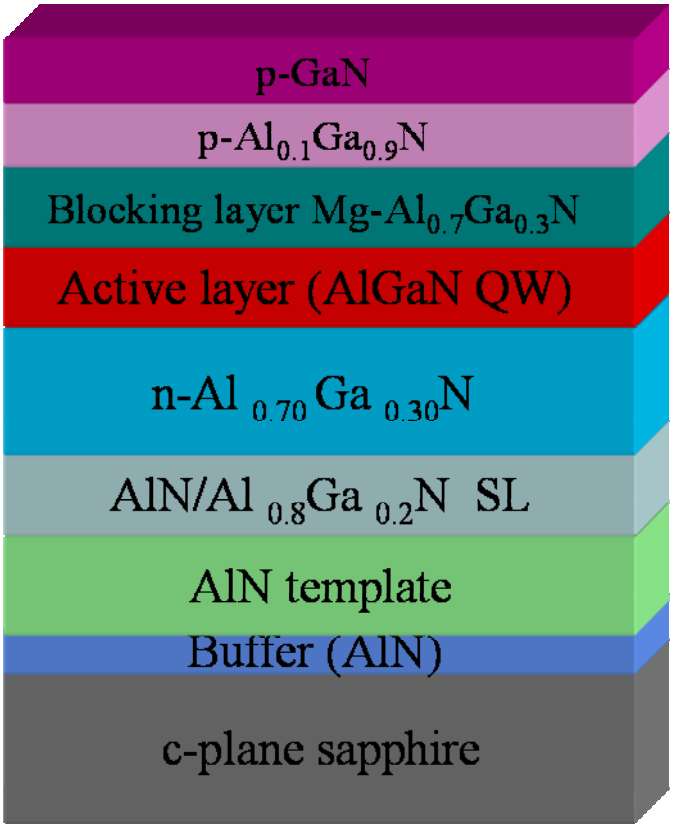

Figure 3.13 Schematic of the layer structure of the deep UV LEDs.

Figure 3.14 shows the electroluminescence (EL) spectrum of a 280 nm deep UV LED with a 300 μm diameter size under 40 mA DC current. The inset of Fig. 3.14 shows the I-V characteristic of 280 nm deep UV LEDs. The forward voltage V_F = 6.7 V, is observed at 20 mA current.

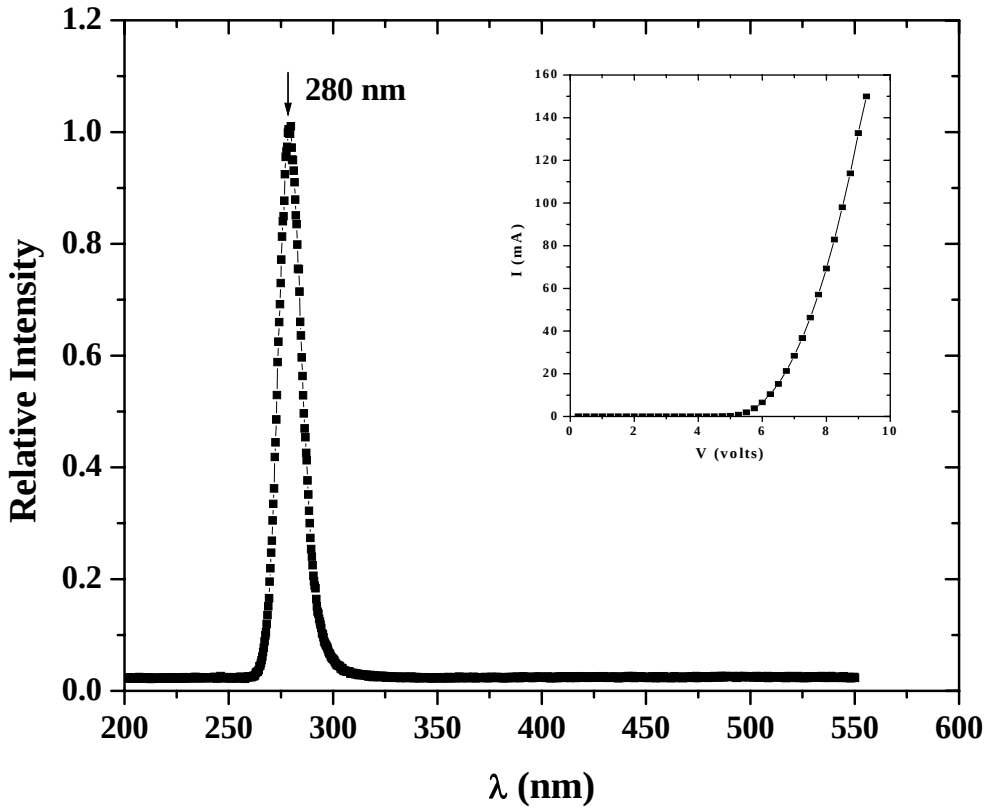

Figure 3.14 EL spectrum of a circular (d = 300 μm) deep UV LED with peak emission at 280 nm under DC bias (I = 40 mA). Inset is the I-V characteristic of the same 280 nm UV LED.

Figure 3.15 shows the light-output power versus current (L-I) characteristic of the 280 nm deep UV LEDs (with a 300 μm disk diameter). We have achieved an optical power output of 0.35 mW and a power density of 0.48 W/cm^2 at 20 mA.

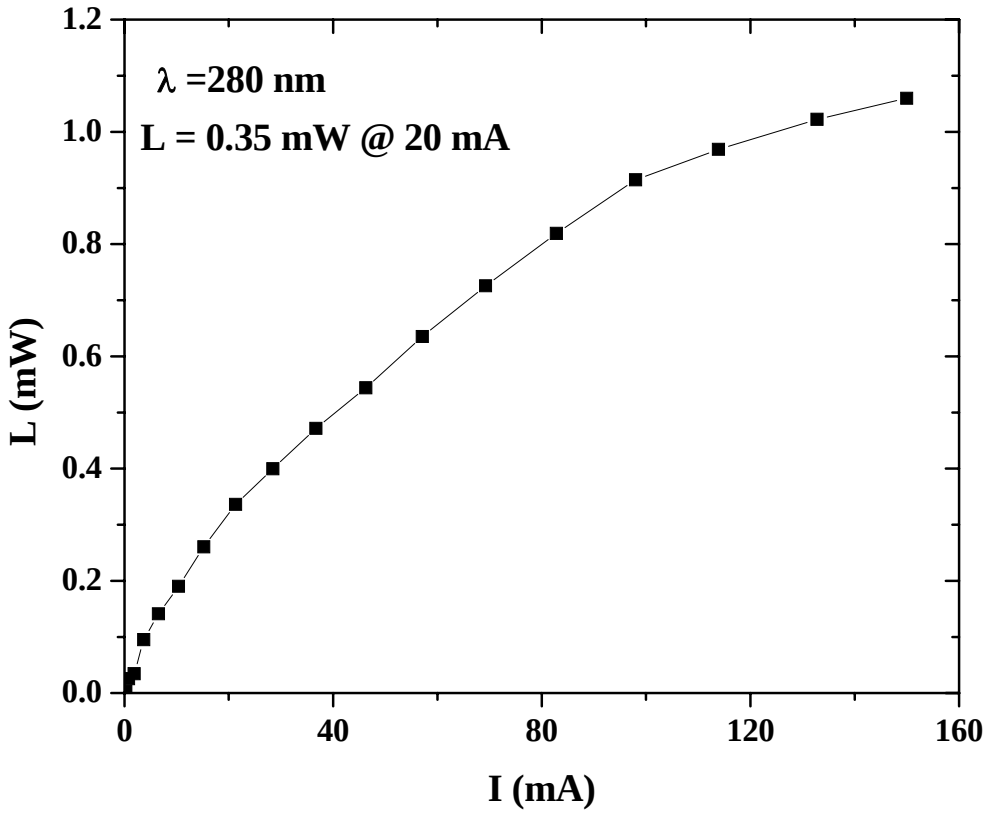

Figure 3.15 Light output power versus current (L-I) of a circular (d = 300 μm) deep UV LED (280 nm).

In summary, a set of AlN/$Al_{0.65}Ga_{0.35}N$ QWs with L_w varying from 1 to 3 nm has been grown by MOCVD. A systematic dependence of the PL emission peak position on L_w was observed, from which a value of about 4 MV/cm for the polarization fields in AlN/$Al_{0.65}Ga_{0.35}N$ QWs was deduced. The PL emission line width was found to increase linearly with L_w. Furthermore, our results have shown that the highest QE was obtained in AlN/$Al_{0.65}Ga_{0.35}N$ QWs with well width between 2 and 2.5 nm, which serves as a guideline for designing optimal deep UV light emitter structures.

3.3 Growth and characterization of a-plane AlN epilayers grown on r-plane sapphire substrate

AlN is emerging as an active material for deep ultraviolet (DUV) optotelectronic devices because of its large direct bandgap ~ 6.1 eV [97, 98]. AlN has strong chemical bonds, which makes AlN based devices very stable and highly resistant to degradation when operating under harsh conditions [99-101]. AlN also plays an important role as a template for the subsequent epitaxial growth of nitride optoelectronic device structures, in which the high quality AlN epilayer serves as a dislocation filter [102-104].

Usually, nitride-based epitaxial structures are grown on (001) *c*-plane sapphire and SiC substrates. Due to the non-symmetric nature of nitrides grown in the (001) direction, a large built-in electrostatic field occurrs perpendicular to the AlGaN/InGaN heterointerfaces because of spontaneous and piezoelectric polarization. Although, these induced fields along the (001) direction have been utilized to design new structures and devices, such as dopant-free high electron mobility transistors, the polarization induced electric fields significantly reduce the electron-hole wavefunction overlap and hence the radiative recombination efficiency in III-nitride quantum wells (QWs). Our previous studies on AlN/AlGaN QWs grown on *c*-plane sapphire substrates showed that the AlN/AlGaN QW structures possess a built-in polarization field of ~ 4 MV/cm [105]. The growth on a nonpolar plane, such as *a*-plane nitrides, is a potential solution to this problem [106]. For DUV emitters utilizing *c*-plane AlGaN alloys as active layers, the dominant emission has a polarization of **E**//**c**, and this unique optical property significantly reduces the surface emission intensity [107]. The growth of nonpolar nitrides on GaN templates has been reported by several groups [108-110]. For optoelectronic devices operating at short wavelengths ($\lambda < 300$ nm), the growth on *a*-plane AlN template would provide reduced effects of polarization fields as well as enhanced surface emission. However, very little work dealing with epitaxial growth [111] of *a*-plane AlN have been previously reported. It has been reported that the Mg energy level in *a*-plane GaN is smaller than that in *c*-plane GaN [112]. If this trend holds true for $Al_xGa_{1-x}N$ alloys and AlN, it will help to improve p-type conductivity in high Al-content AlGaN alloys.

In this chapter we summarize the growth by metalorganic chemical vapor deposition (MOCVD) of *a*-plane AlN epilayers grown on *r*-plane sapphire substrates. We also investigate the energy level of Mg acceptors in *a*-plane AlN. Various characterization techniques were employed to probe their structural and optical properties. X-ray diffraction (XRD) was used to determine the crystalline quality, while atomic force microscopy (AFM) was used to probe the surface morphologies. Photoluminescence (PL) emission spectroscopy was employed to investigate the optical properties.

AlN epilayers were grown on *r*-plane sapphire substrates by MOCVD with a growth temperature and pressure of 1300 ^{0}C and 40 Torr, respectively. Trimethylaluminum (TMAl) and Ammonia (NH_3) were used as the Al and N sources, respectively. A thin AlN buffer layer was first grown to serve as a nucleation layer followed by the growth of a 1μm AlN epilayer as shown in Fig. 3.16. A deep UV optical spectroscopy system, consisting of a frequency quadrupled 100 femtosecond Ti: Sapphire laser with an average power of 3 mW and a repetition rate of 76 MHz at 196 nm and a 1.3 m monochromator with a detection capability ranging from 185 - 800 nm, was utilized for PL studies [62].

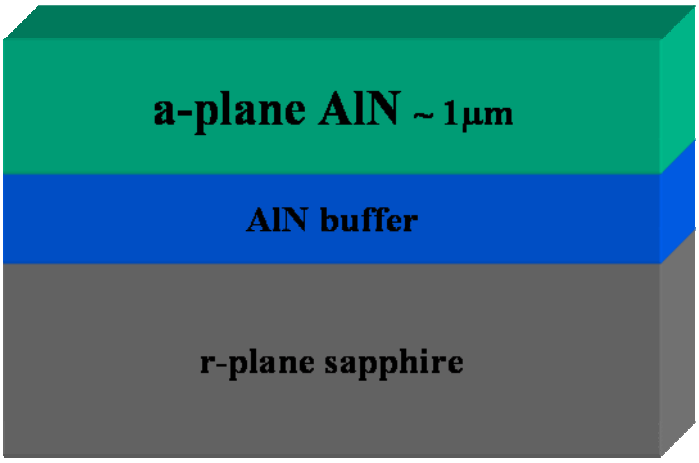

Figure 3.16 Schematic layer structure of a-plane AlN epilayer grown on r-plane sapphire substrate.

The growth surface of the AlN epilayers was determined to be *a*-plane using XRD θ-2θ scan, which detected sapphire (102), (204), and *a*-plane AlN (110) reflections, as illustrated in Fig. 3.17. Only the *a*-plane reflection peak at $2\theta = 59.4^0$ was observed. Since the AlN (002) reflection at $2\theta = 36.02^0$ was not detected, demonstrating that the films were uniformly a-plane-oriented [113].

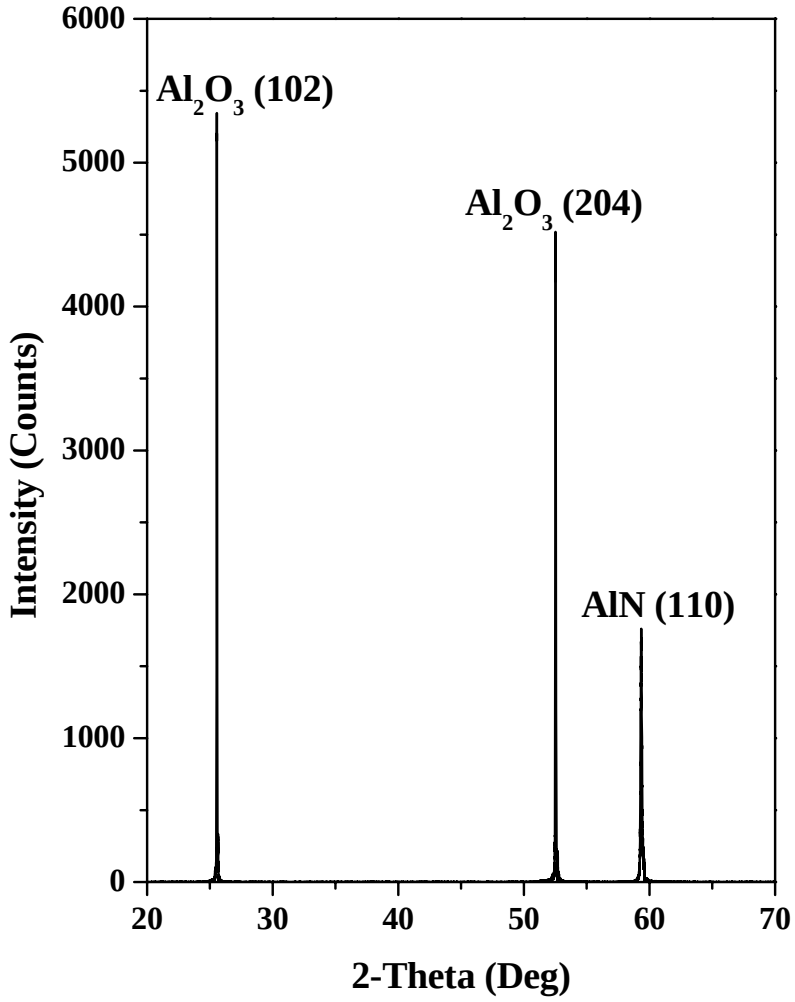

Figure 3.17 XRD θ-2θ scan of an a-plane AlN epilayer.

As shown in Fig. 3.18, the measured FWHM of the XRD rocking curve of the (110) reflection peak is about 940 arcsec, which to our knowledge is the narrowest value reported. The surface morphology of the *a*-plane AlN epilayer is still relatively rough with a root mean square (RMS) of surface roughness of about 8 nm for a 10 μm x 10 μm area, in contrast to the smooth surface of *c*-plane AlN with a typical RMS value of less than 1 nm [114]. Significant improvements in surface morphology and XRD linewidth are expected since the development of growth technology of *a*-plane AlN is in a very early stage.

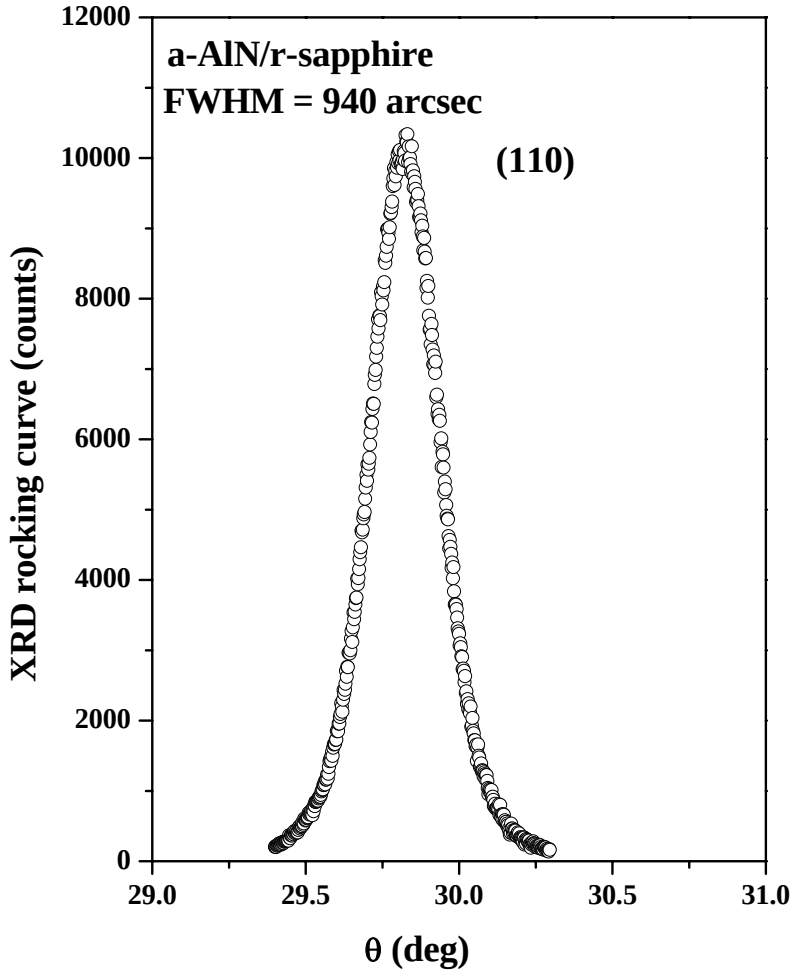

Figure 3.18 XRD rocking curve of (110) reflection peak of an a-plane AlN epilayer with a full width at half maximum (FWHM) of 940 arcsec.

Figure 3.19 compares the room temperature (300 K) PL spectra of *c*-plane and *a*-plane AlN epilayers covering a broad spectral range from 2 to 6.2 eV. The peak position of the band-edge transition in *a*-plane AlN epilayer is at 5.95 eV, which is about 30 meV below that in *c*-plane AlN epilayer (5.98 eV). This redshift of the band-edge transition could be related to the anisotropy of the in-plane strain in *a*-plane AlN epilayer, in which the strain induced band-gap shift depends on all three strain components [115]. Although the growth technology of *a*-plane AlN is much less mature than that for *c*-plane AlN, the intensity of the band-edge emission in *a*-plane AlN is comparable to that in *c*-plane AlN. This is partly due to the unique polarization property of the optical emission (**E**//**c)** in *c*-plane AlN, which tends to reduce the surface emission intensity [107]. Thus, we expect that the band edge emission intensity from *a*-plane AlN epilayers will be much higher than that from *c*-plane AlN of the same optical quality. The PL emission spectrum of the *a*-plane AlN epilayer also comprises of a deep level impurity transition, which could be due to the recombination between shallow donors and cation vacancy complexes with two-negative charges [116, 117]. The emission intensity of this deep level transition is relatively weak and can be suppressed with further improvement in the material quality.

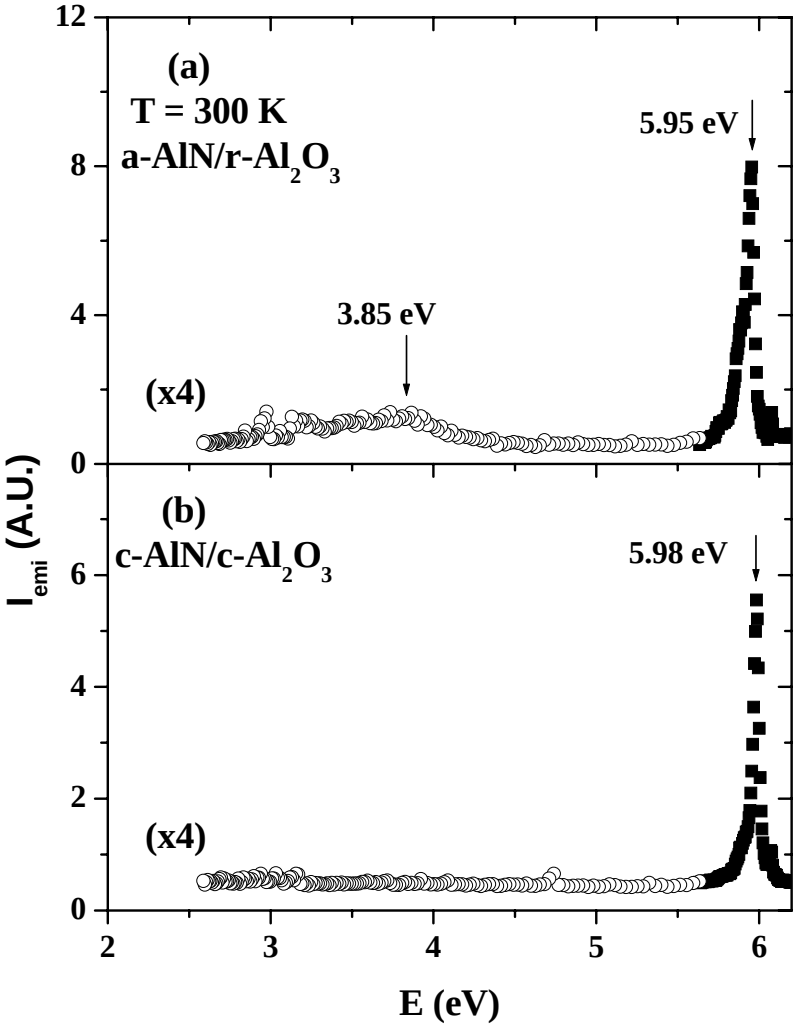

Figure 3.19 Room temperature (300 K) PL spectra of (a) a-plane and (b) c-plane AlN epilayers.

To determine the energy level of Mg dopants in *a*-plane AlN, a 1-μm-thick Mg-doped *a*-plane AlN epilayers were grown on *a*-plane AlN (1μm)/*r*-plane sapphire templates. High quality, undoped AlN epilayer template plays an important role in reducing dislocations in the subsequent doped layer. As-grown Mg-doped layers were highly resistive. Moreover, subsequent post-growth annealing of Mg-doped *a*-plane AlN in nitrogen gas ambient did not result in p-type conduction. Fig. 3.20 shows the room temperature (300 K) PL spectra for Mg-doped (a) *c*-plane and (b) *a*-plane AlN epilayers. The PL spectra presented in both Figs. 3.20(a) and (b) encompass an emission peak at around 4.7 eV, in addition to the band-edge emission at 5.94 and 5.91 eV for *c*-plane and *a*-plane Mg-doped AlN, respectively. The band-edge emission peaks for both *a*-plane and *c*-plane AlN epilayers are due to the recombination of excitons bound to neutral Mg acceptors (or neutral acceptor-bound excitons, I_1). The binding energy, E_{bx}, of the acceptor-bound excitons is the same for both *c*- and *a*-plane AlN epilayers, E_{bx} = (5.98 – 5.94) eV for *c*-plane AlN = (5.95 – 5.91) eV for *a*-plane AlN = 40 meV, which is consistent with our previous measurement for *c*-plane AlN [118] and suggesting an identical energy level of Mg acceptors in both *c*-plane and *a*-plane AlN based on the Haynes' rule. The emission peak at 4.7 eV in Mg-doped AlN was previously identified and is due to the donor-acceptor pair (DAP) recombination involving electrons bound to nitrogen vacancies with three positive charges V_N^{3+} (deep donors) and neutral Mg acceptors (Mg^0) [114].

Based on the two observations shown in Fig. 3.20, the identical acceptor-bound exciton binding energy (E_{bx}) and the emission peak position of the Mg related impurity transition at 4.7 eV, we believe that the Mg acceptor energy level in *c*-plane and *a*-plane AlN is the same, which is ~ 0.5 eV [114,118,119].

In summary, *a*-plane AlN epilayers were grown on *r*-plane sapphire by MOCVD. PL studies showed that (1) the bandedge emission intensity of *a*-plane AlN is comparable to that of *c*-plane AlN and (2) Mg energy levels in *a*- and *c*- plane AlN epilayers are the same and around 0.5 eV. Much improvement in the material quality of *a*-plane AlN can be achieved by further optimizing the growth processes, which would provide significant enhancement in emission efficiency. These results point out that *a*-plane AlN templates can be utilized to build UV optoelectronic devices possessing minimized effects of polarization fields and enhanced surface emission.

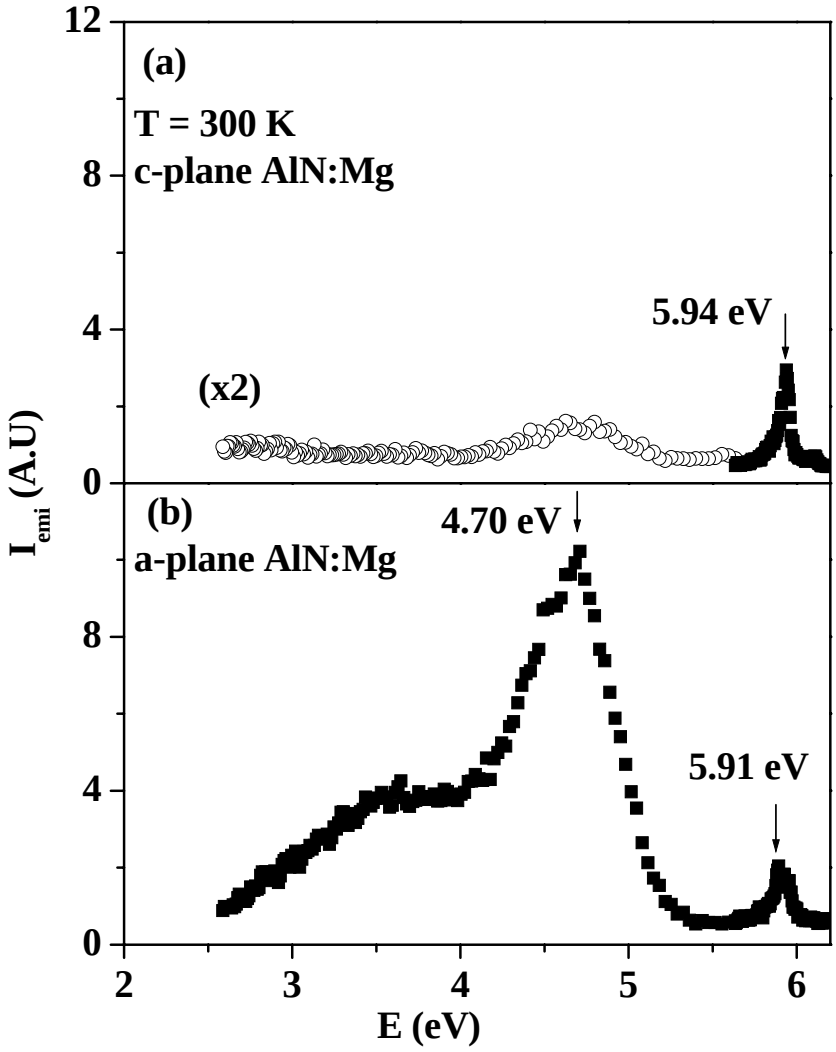

Figure 3.20 Room temperature (300 K) PL spectra of Mg-doped (a) c-plane and (b) a-plane AlN epilayers.

3.4 Growth and photoluminescence studies of a-plane Al-rich AlN/$Al_xGa_{1-x}N$ quantum wells

Deep ultraviolet (UV) emitters and detectors operating in the 200–340 nm wavelength range are important devices for many applications, including water purification, biological and chemical agent detection, and medical research/health care [120]. Al-rich AlGaN alloys have a tunable emission wavelength down to 200 nm, which makes them very useful for these applications. As demonstrated by light emitting diodes, laser diodes, and electronic devices, many III-nitride based devices must take advantages of quantum well (QW) structures in order to achieve optimal device performance. To realize deep UV emission ($\lambda < 280$ nm), Al-rich AlGaN based QWs are required. Recently, several groups have been studying Al-rich AlGaN based emitters to obtain UV emission wavelength below 300 nm [121-126]. The growth of the QW structures on the basal plane of either sapphire or SiC resulted in the deposition of wurtzite material with (001)-plane (*c*-plane) orientation [127]. Interfacial polarization discontinuities within heterostructures are associated with fixed sheet charges which produce strong internal electric fields. These ‘‘built-in’’ polarization-induced electric fields significantly reduce the electron-hole wavefunction overlap and radiative efficiency and hence limit the performance of optoelectronic devices that employ nitride QWs as active region. Our previous studies on AlN/AlGaN QWs grown on c-plane sapphire substrate showed that these AlN/AlGaN QW structures possess a built-in polarization field of ~ 4 MV/cm [105].

Nitride crystal growth along nonpolar directions provides an effective mean for producing nitride-based quantum structures that exhibit reduced effects by the strong polarization-induced electric fields since the polar axis lies within the growth plane of the film. The growth of *a*-plane GaN/AlGaN QW structures on *r*-plane sapphire substrates have been previously demonstrated [128,129]. Optical characterization of these structures has shown that the effects due to the polarization-induced electric fields are greatly reduced in nonpolar QWs.

In this chapter the growth and PL properties of *a*-plane AlN/$Al_{0.65}Ga_{0.35}N$ QWs grown on r-plane sapphire substrates by metalorganic chemical vapor deposition (MOCVD) are studied. We also investigated a range of well widths for *a*-plane and *c*-plane QWs, which allowed us to reveal the emission characteristics that are unique to QWs with nonpolar orientation. Deep UV

PL emission spectroscopy was employed to probe the L_w dependence of the optical properties. Our results showed that in *a*-plane QWs, high emission efficiency can be attained at $L_w > 2$ nm. In contrast, there exists an optimal choice of L_w (= 2 nm) for obtaining high emission efficiency in *c*-plane QWs. The PL decay time of *a*-plane QWs exhibits only a slight increase with increasing L_w, while that of *c*-plane QWs has a strong dependence on L_w.

AlN/$Al_xGa_{1-x}N$ ($x \sim 0.65$) QWs were grown on *r*-plane and *c*-plane sapphire substrates by MOCVD. The growth temperature and pressure were 1120 °C and 50 Torr, respectively. Prior to the growth of AlN/$Al_{0.65}Ga_{0.35}N$ QW, a thin AlN buffer layer and a 1 μm undoped AlN epilayer were first grown on sapphire. This was then followed by the growth of $Al_{0.65}Ga_{0.35}N$ QW and a 10 nm AlN barrier. The barrier and well widths were determined by the growth rates of the AlN and $Al_xGa_{1-x}N$ epilayers. The samples were mounted on a low temperature (10 K) stage with a cold finger in a closed-cycle helium refrigerator. The deep UV PL spectroscopy system consists of a frequency quadrupled 100 fs Ti:sapphire laser with an average power of 3 mW and a repetition rate of 76 MHz at 196 nm, a 1.3 m monochromator with a detection capability ranging from 185 to 800 nm, and a streak camera detector with 2 ps time resolution [62].

The (10 K) PL spectra of the *c*- and *a*-plane AlN/$Al_{0.65}Ga_{0.35}N$ QWs are shown in Figs. 3.21(a) and 3.21(b), respectively. Independent of the crystal orientation, the QW PL emission peak shifts to lower energies with increasing L_w, due to the weakening of the quantum confinement effect. In particular, the emission peak energies of the *a*-plane QWs steadily approach but do not redshift beyond the band edge transition of the $Al_{0.65}Ga_{0.35}N$ epilayer with increasing L_w. Conversely, the *c*-plane QW emission peak energy redshifts with L_w and becomes even lower than the band edge transition peak of the $Al_{0.65}Ga_{0.35}N$ epilayer at $L_w > 2$ nm. This strong dependence of the PL emission energy on L_w in *c*-plane QWs is due to the strong spontaneous and strain-induced piezoelectric fields ~ 4MV/cm [105], in addition to the quantum size effect. These polarization fields are much weaker in *a*-plane QWs [130].

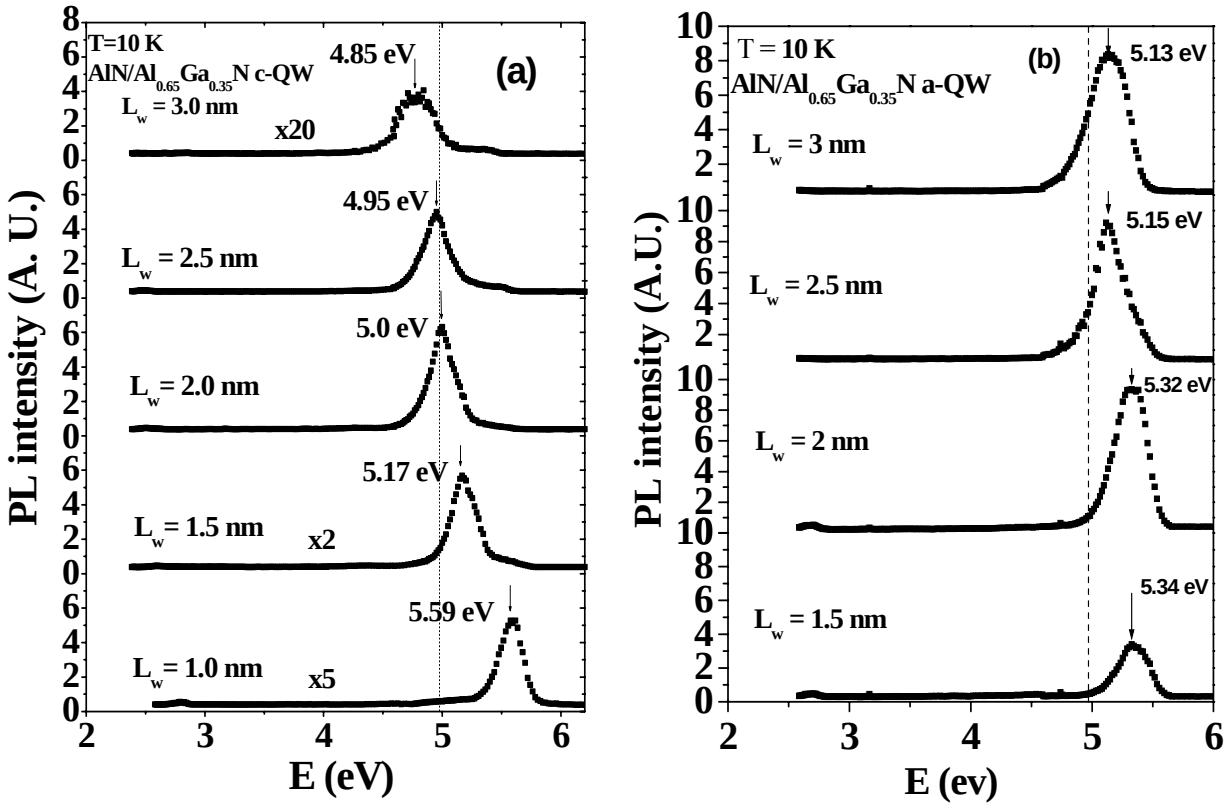

Figure 3.21 Low temperature (10 K) PL spectra of (a) c-plane $AlN/Al_{0.65}Ga_{0.35}N$ QWs with well width, L_w, varying from 1 to 3 nm and (b) a-plane $AlN/Al_{0.65}Ga_{0.35}N$ QWs with well width, L_w, varying from 1.5 to 3 nm. All samples have a fixed barrier width of 10 nm. The vertical dashed lines represent the emission peak position of $Al_{0.65}Ga_{0.35}N$ epilayers.

The normalized PL emission intensity of the *a*- and *c*-plane QWs as a function of L_w is plotted in Fig. 3.22 (each orientation's intensity was normalized separately). We observed that high emission intensity can be obtained in *a*-plane QWs with $L_w > 2$ nm and in *c*-plane QWs with $L_w = 2$ nm. In *c*-plane QWs, the balance between the reduced radiative recombination efficiency in thick wells due to the polarization fields and in thin wells due to enhanced carrier leakage to the barrier region [131] results in an optimal choice of L_w for obtaining high emission efficiency. In contrast, since the polarization fields are much weaker in nonpolar QWs, high emission efficiency is obtained in QWs with $L_w > 2$ nm. This suggests that the *a*-plane AlN/AlGaN QW system potentially provides a much greater flexibility for the device structural design than its *c*-plane counterparts.

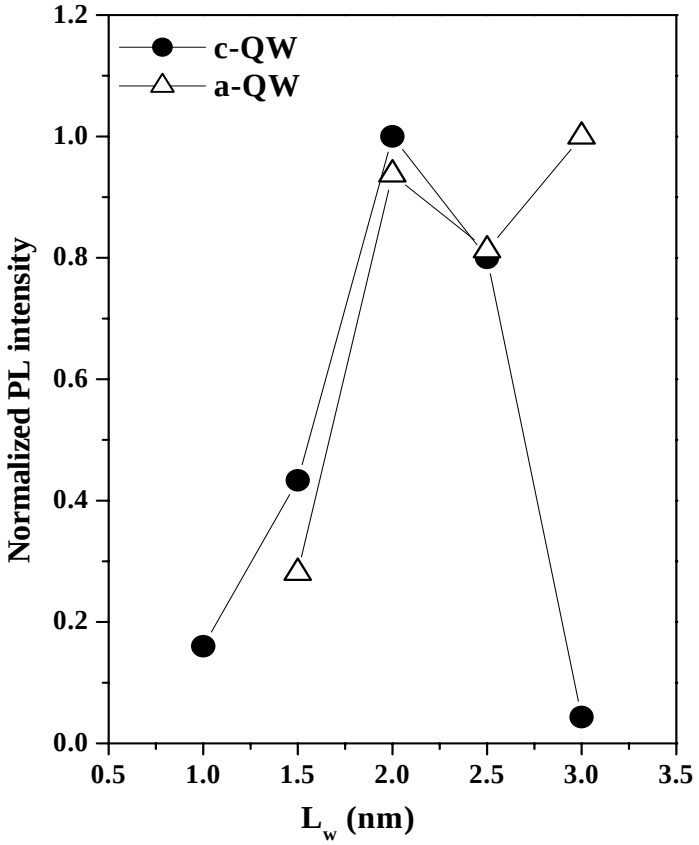

Figure 3.22 Normalized low temperature PL intensity plotted as a function of well width, L_w, for both a- and c-plane AlN/$Al_{0.65}Ga_{0.35}N$ QWs.

To further investigate the differences between polar and nonpolar QWs, the PL decay characteristics of *a*- and *c*-plane QWs for two representative well widths (L_w = 1.5 and 3 nm) were measured and the results are shown in Fig. 3.23. The PL decay transients show nonexponential decay with a slower component at longer decay times. For *c*-plane QWs the PL decay time strongly depends on L_w. This can be explained by the presence of the strong polarization fields (~ 4 MV/cm) in the polar QWs. The electrostatic fields spatially separate the electron and hole wave functions, thereby reducing the oscillator strength for their radiative recombination. At low temperatures, the measured decay time corresponds mainly to the radiative lifetime, which is inversely proportional to the oscillator strength [120]. Conversely, for *a*-plane QWs the PL decay time exhibits only a weak dependence on L_w.

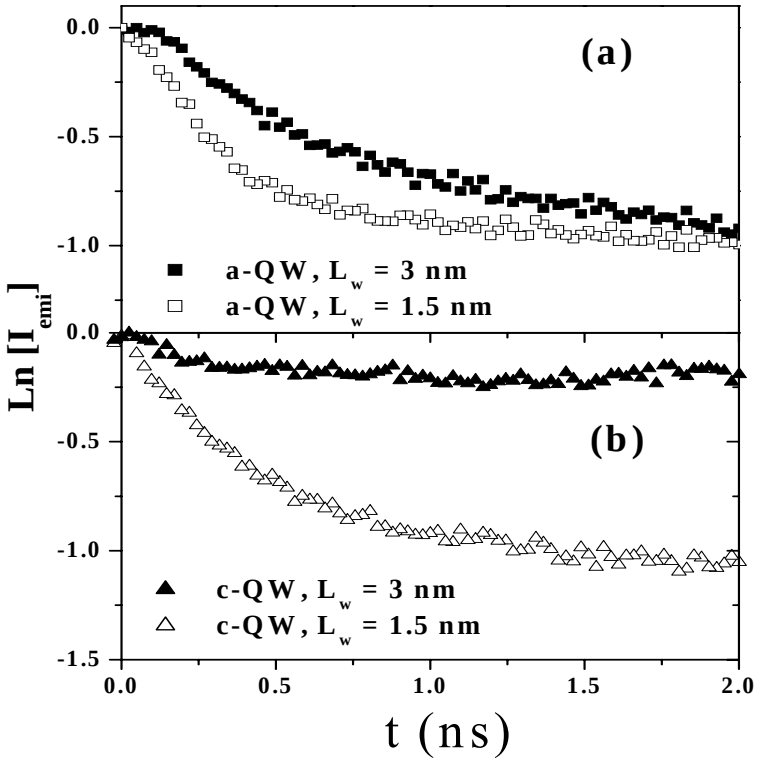

Figure 3.23 Low temperature (10 K) PL decay transients of two representative AlN/$Al_{0.65}Ga_{0.35}N$ (a) a-plane and (b) c-plane QWs with L_w = 1.5 and 3 nm.

Figure 3.24 shows the Arrhenius plots of the PL intensity for (a) *a*-plane and (b) *c*-plane QWs with L_w = 1.5 nm. The solid lines in both plots are the least squares fit of the measured data to the following equation

$$I_{emi}(T) = I_0[1 + Ce^{(-E_0/KT)}]^{-1} \tag{3.7}$$

where I_{emi} (T) and I_0 are, respectively, the PL intensities at finite temperature T and 0 K, while E_0 is the activation energy. At T > 140 K, the PL intensity is thermally activated with activation energy of about 125 meV for *a*-plane QW and 110 meV for *c*-plane QW. Since the observed activation energies are much smaller than the band offsets of the bandgap difference between the wells and barriers, the thermal quenching in these samples is not due to the thermal activation of electrons from QWs to barriers. The quenching of the luminescence with temperature can be explained by thermal emission of the carriers out of a confining potential (exciton localization potential) allowing their scattering with dislocations. An activation energy around 120 meV has been previously measured for the PL intensity in $Al_{0.70}Ga_{0.3}N$ epilayers grown on *c*-plane sapphire [132], which is close to the activation energies obtained in $Al_{0.65}Ga_{0.35}N$ QWs of the present study. The higher activation energy in *a*-plane QWs (125 meV) than in *c*-plane QWs (110 meV) may be attributed to an increased interface or alloy fluctuation, which is also reflected in a slight increase in the PL emission linewidth in *a*-plane QW (Fig. 3.21). Furthermore, as pointed out previously [133], "lateral" polarization fields may still present in *a*-plane QWs because the *c*-axis lies in the *a*-plane so that the well width fluctuations could induce polarization fields in the *a*-plane, resulting in an inhomogeneous spectral broadening and an apparent enhanced localization energy. The slow decay component displayed by *a*-plane QWs shown in Fig. 3.23(a) may also suggest the existence of “lateral" polarization fields. The larger drop in PL intensity in *a*-plane QWs than in *c*-plane QWs in the temperature region of 10-300 K may be related to the growth anisotropy along nonpolar directions so that *a*-plane QWs possess more dislocations than *c*-plane QWs, as suggested by XRD and AFM measurements.

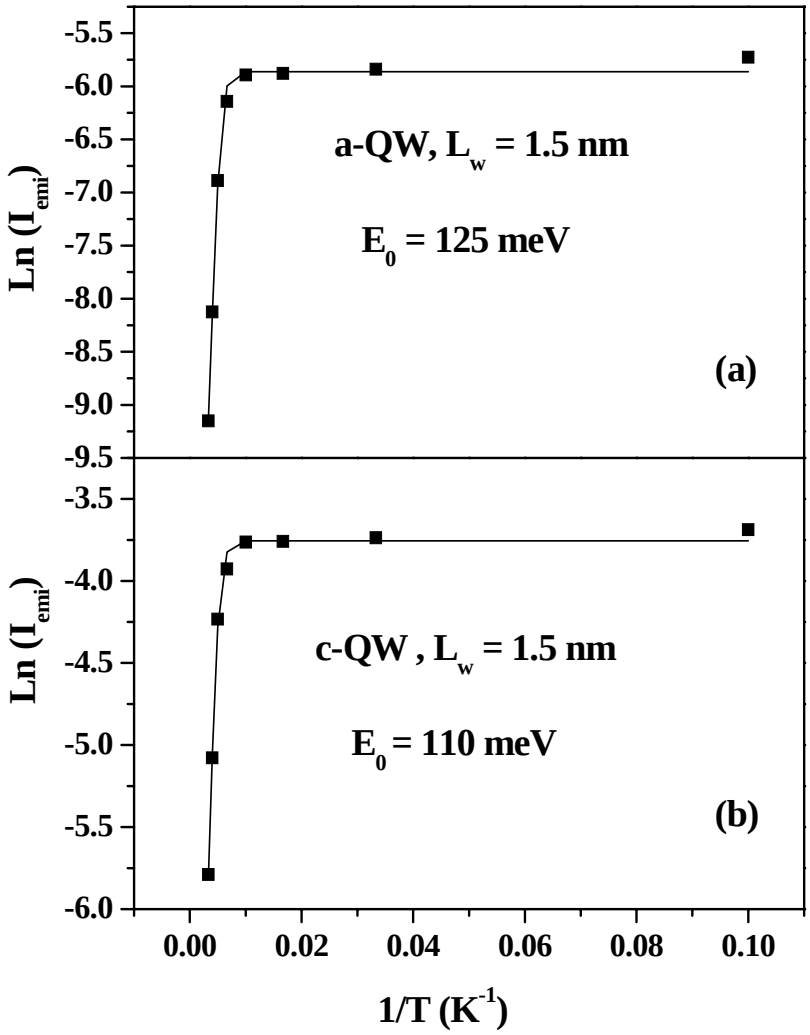

Figure 3.24 The Arrhenius plots of the PL intensity of (a) a-plane and (b) c-plane QWs with L_w = 1.5 nm. The solid lines in both plots are the least square fits of the measured data to Eq.(3.7).

In summary, *a*- and *c*-plane AlN/$Al_{0.65}Ga_{0.35}N$ QWs were grown by MOCVD and their PL emission characteristics were measured and compared. It was found that the low temperature PL characteristics of *a*-plane QWs are primarily governed by the quantum size effect as in traditional III-V semiconductor QWs. In contrast, the emission characteristics of *c*-plane QWs are affected by strong polarization fields in addition to the quantum confinement effect. The PL decay time was found to be weakly dependent on the well width, L_w, for *a*-plane QWs. However, a strong dependence of the PL decay time on L_w was observed for *c*-plane QWs, which is caused by the variation of the polarization fields in QWs due to varying L_w. The thermal quenching of PL emission in both *a*- and *c*-plane QWs is attributed to the activation of excitons from localized states. It was shown that to obtain highest quantum efficiency, *a*- and *c*-plane AlN/AlGaN QWs with high Al contents should be designed to have $L_w > 2$ nm and $L_w \approx 2$ nm, respectively. The results thus suggested that the *a*-plane AlN/AlGaN QW system potentially provides a much greater flexibility for the device structural design than its *c*-plane counterparts.

3.5 Growth of high quality AlN epilayers on silicon carbide (SiC) substarte by MOCVD

As the demand for nitride optoelectronic devices at shorter wavelengths continues to increase, the growth of high quality AlN and Al-rich AlGaN has been the subject of great focus. AlN has been used for years as a nucleation layer for GaN grown on sapphire [134] and SiC [135]. Recently much research has been directed towards producing high-quality epilayers on sapphire [136–138] and SiC [139, 140]. We used SiC substrates, for the following three primary advantages: (1) as a conducting substrate, SiC presents the opportunity for vertically conducting optoelectronic devices, (2) it has a lattice mismatch (0.9%) with regards to AlN that is significantly less than that with sapphire (13%), (3) the thermal coefficient of expansion of SiC is also very close to those of the nitrides, and the substrate provides good heat-sinking for many device applications.

However, despite the apparent benefits of SiC substrates, III-nitride films deposited on SiC substrates have yet to demonstrate less defective microstructures than films of comparable thickness on sapphire. One reason proposed for this is the damaged surface of as-received SiC wafers as a result of slicing from the boule and polishing. The AFM image of Fig. 3.25 shows the surfaces of on-axis 4H-SiC (001) substrates feature numerous randomly oriented scratches due to mechanical polishing, with widths from 100-300 nm and depths to 5 nm. These scratches are commonly observed on as-received SiC wafers since the mechanical hardness and chemical inertness of this material makes polishing difficult [141]. The polishing process results in damage extending to a micron beneath the surface [142], and even with a highly optimized polishing process, sub-surface damage extends up to 8 nm in the regions of the scratches [143].

A dramatic improvement in surface quality is attained after annealing the wafers to high temperatures in flowing H_2 gas. Under high temperatures, H_2 is cracked such that very reactive H atoms etch the surface of the SiC substrate [144].

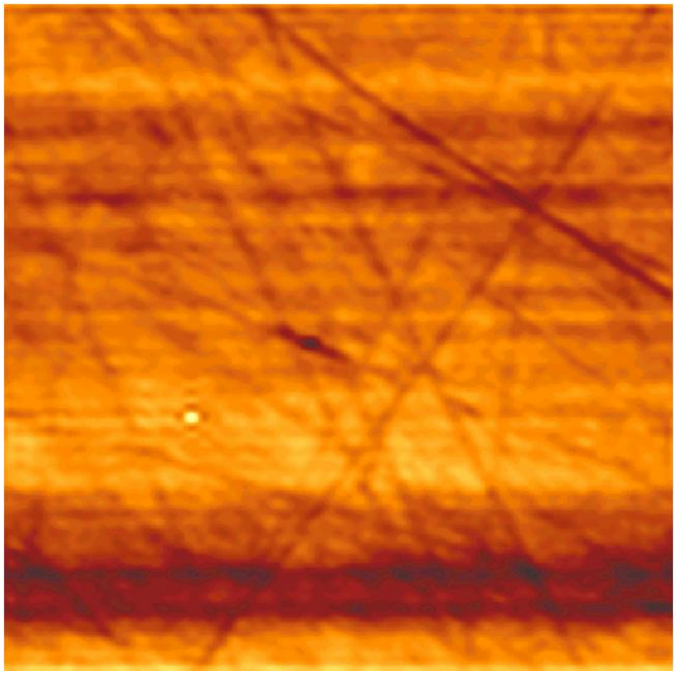

Figure 3.25 A 10 μm x 10 μm AFM image of as-received Si-face SiC (001) wafer showing polishing scratches present on the surface.

Preparation of the Al_2O_3 substrates consisted of a chemical cleaning in acetone, methanol, and then deionized water. These steps are utilized to remove organic, ionic, and metallic impurities on the surface. For the preparation of SiC substrates, one pertinent issue, in addition to removing organics or grease, is the removal of oxide from the surface. So the SiC substrates were dipped in a 10% HF solution to remove the surface oxide.

Fig. 3.26 shows the layer structure for 1 μm thick AlN epilayers grown on Si-face SiC (001) substrates. TMAl and NH_3 were used as Al and N sources, respectively. The typical AlN/SiC growth procedure can be summarized as follows, after the substrate was cleaned and loaded onto the susceptor, the reactor was evacuated and purged with hydrogen gas to remove any traces of air. The total H_2 flow rate was 3 liters/minute (l/min) and it took around 5 minutes. The susceptor temperature was then ramped to 1250 ^{0}C in the H_2 ambient established in the previous step. This temperature was maintained for 50 minutes aiming to eliminate the scratches from the surface of the substrate. The pressure of the reaction chamber was about 40 Torr. After this step the susceptor temperature was lowered down to 950 ^{0}C and the hydrogen flow rate was lowered to 2 l/min. After the temperature and pressure were stabilized, and all the appropriate flows were set up in the vent mode, the growth of AlN buffer layer was initiated by switching the H_2/TMAl and NH_3 flow into the reaction chamber. The growth lasted for around 30 sec with total thickness around 12 nm. The growth was terminated by diverting the H_2/TMAl flow into the vent line. This layer was used as the buffer for the AlN epilayer. The temperature was ramped up to 1325 ^{0}C under the established H_2 and NH_3 ambient. The epitaxial growth AlN was started at 1325 ^{0}C by switching all the necessary gas flows into the reactor. At the end of the growth period, the organometallic flows were diverted back to the bypass line, and turned off. The sample was cooled under the established H_2 + NH_3 ambient until 600 ^{0}C, and then NH_3 was turned off. The sample was removed from the reactor when the susceptor temperature was below 100 ^{0}C. The above growth procedure was a typical one, but the actual process could be varied to get the intended results. In Fig. 3.27 the susceptor temperature sequence in a typical AlN growth is shown.

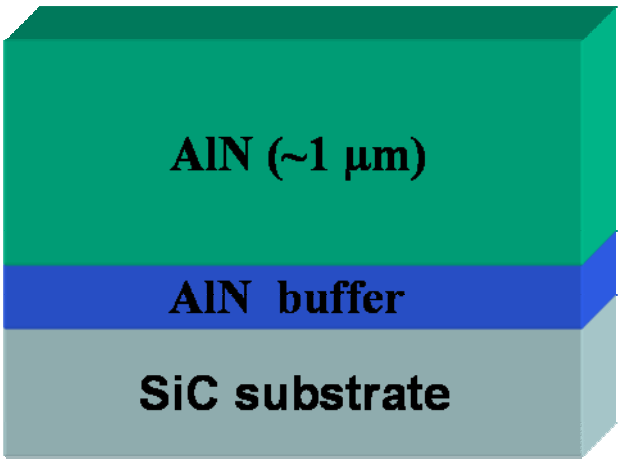

Figure 3.26 Schematic layer structure for the growth of AlN epilayers.

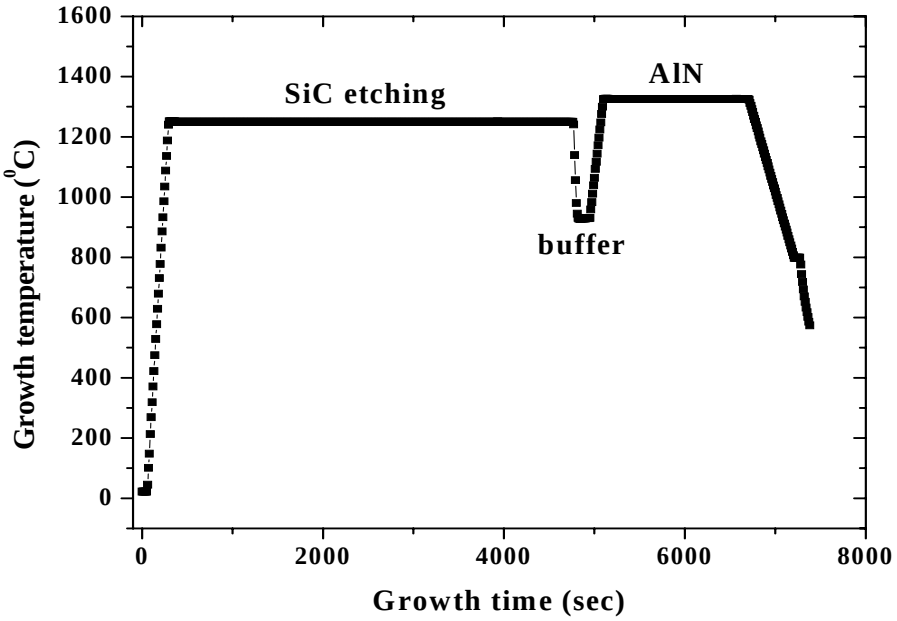

Figure 3.27 Growth temperature sequence of the AlN epilayer growth on SiC substrate.

Growth conditions for AlN on SiC are very different with that on sapphire substrate. AlN layers grown on SiC with the same growth conditions of sapphire substrate peeled off and were cracked, the PL spectra exhibit impurity transition, and the XRD rocking curves of (002) and (105) peaks were broad.

Lattice mismatch usually causes tensile or compressive stress degrading crystalline and structural quality of epilayers. Stresses in thin films consist of intrinsic and thermal components. The intrinsic component is complex and can originate from one or more factors occurring during growth, such as incorporation of impurities and lattice mismatch between film and substrate. The thermal component is easily modeled as the difference in thermal expansion between the film and substrate. During cooling from the growth temperature, the film is tensioned if the film contracts more than the substrate will allow. Conversely, the film is compressed if the substrate contracts more than the film will allow.

The resulting strain due to lattice mismatch is compressive for AlN grown on sapphire [145]. This strain is relieved after several nanometers of growth according to the critical thickness theory [146]. The primary relief mechanism is the formation of dislocations in the film/substrate interface during film growth. Upon cooling, the difference in thermal expansion coefficients ($\alpha_{sapphire} > \alpha_{AlN} > \alpha_{GaN}$) results in additional compressive stresses assumed to be responsible for the compression.

Studies of AlN (001) grown on SiC (001) found strains due to lattice mismatch at the AlN/SiC interface to be compressive (i.e. $a_{GaN} > a_{AlN} > a_{SiC}$). The mismatch is believed to be partially relieved by the formation of misfit dislocations. However, there is tensile strain along the a-axis in the AlN layers grown on SiC, which tends to crack the surface of the nitride layers [147]. This problem has limited the layer structures of devices. Thus crack elimination from nitride layers is a crucial issue in realizing device applications.

Growth of AlN on SiC requires careful optimization of the buffer conditions to achieve a balance between the compressive lattice mismatch and the tensile thermal mismatch. The high density crack in the AlN was not totally eliminated with any of the growth conditions for both the AlN buffer layer and the AlN epilayer. With such a high crack density the technique of Ga flux as substrate treatment before the initiation of the growth was employed. The AlN crystalline quality and surface morphology declined with increasing TMGa flow. Meanwhile, the density of cracks was reduced and totally eliminated at high TMGa flow (10 sccm). Fig. 3.28(a) indicates

the results of XRD measurements for different TMGa flow rates. FWHM of the (002) and (105) XRD rocking curve increases with increasing TMGa flow rate. In (b) the surface roughness measured by root-mean square (RMS) increased with increasing TMGa flow rate.

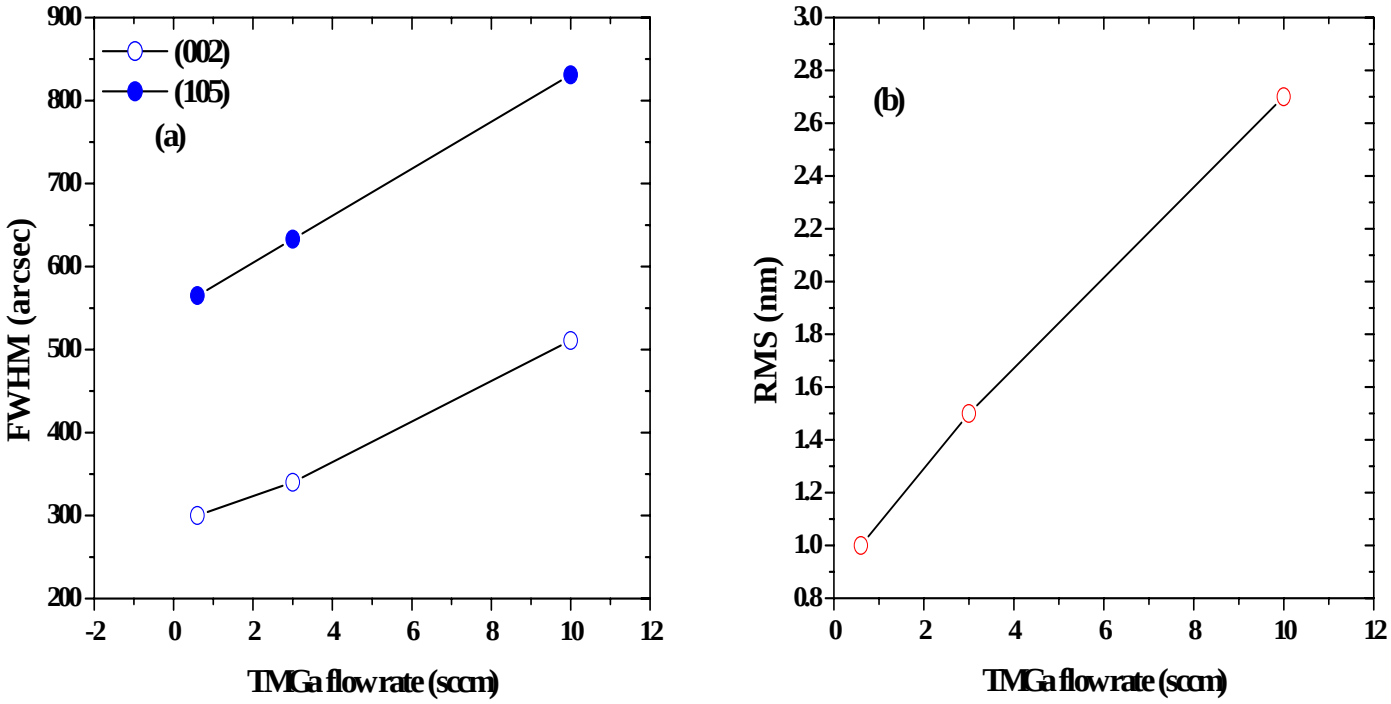

Figure 3.28 (a) FWHM of (002) and (105) rocking curve and (b) RMS of surface roughness of AlN epilayers as functions of TMGa flow rate.

Another approach to eliminate the crack problem was to use gallium as a surfactant. Various TMGa flow rates ranging from 0.1 to 1 sccm have been used. The crystalline quality of the AlN epilayer declined with increasing TMGa flow rate. A 0.4 sccm TMGa was enough to totally eliminate the cracks (Fig. 3.29) with a reasonable crystalline quality. The FWHM of (002) and (105) rocking curve are 350 and 626 arcsec respectively.

Figure 3.29 Optical microscope image of a crack free AlN epliayer grown on SiC.

The growth conditions of the AlN buffer layer on SiC were investigated. The growth pressure was varied from 40 to 90 Torr, the buffer pressure in the investigated range showed almost no effect on the crystalline quality and surface morphology of AlN epilayer. As the layer temperature and thickness have a significant effect on the crystalline quality of AlN grown on sapphire [37], the buffer temperature was varied for 1 μm AlN epilayers grown on SiC from 900 to 960 ^{0}C. As shown in Fig. 3.30, FWHM of (105) rocking curve increases with increasing temperature. (002) rocking curve has lowest linewidth at 930 ^{0}C. In this temperature range the surface roughness was not significantly impacted.

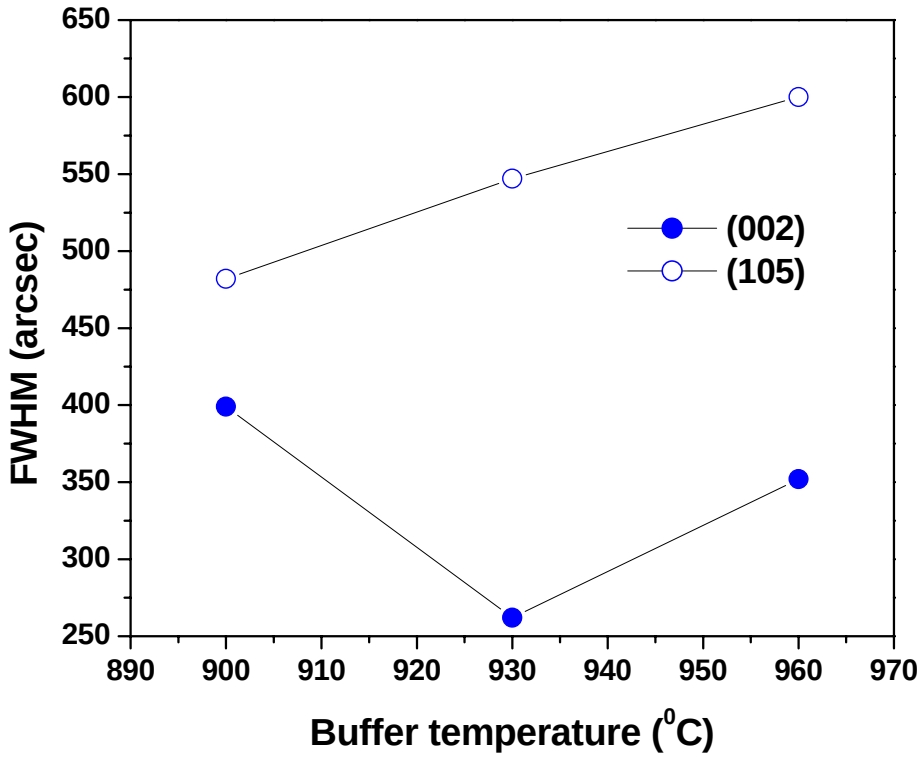

Figure 3.30 Full width at half maximum (FWHM) of (002) and (105) rocking curves of AlN epilayer as functions of AlN buffer temperature.

The buffer thickness was varied from 6 to 21 nm and Fig. 3.31 shows the FWHM of (105) and (002) rocking curve as functions of buffer thickness. The optimum buffer thickness was 12 nm.

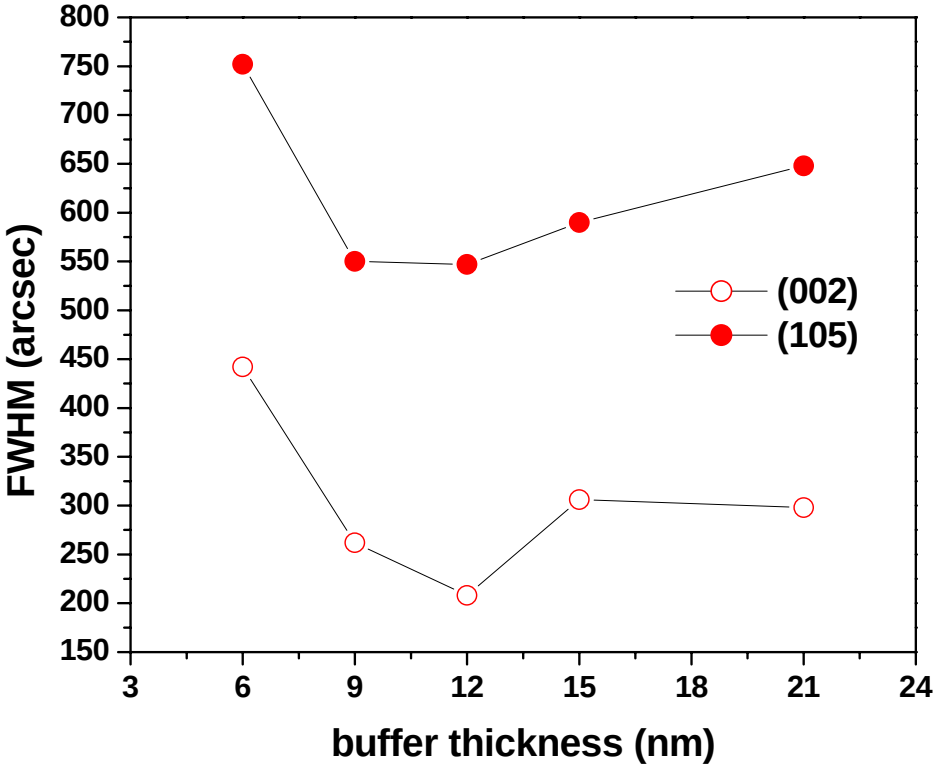

Figure 3.31 Full width at half maximum (FWHM) of (002) and (105) rocking curves of AlN epilayer as functions of AlN buffer thickness.

After the AlN buffer optimization, a systematic study was also done to optimize high temperature AlN epilayer growth. For example, AlN growth rate was investigated by varying TMAl flow rate. The NH_3 flow was held constant thus the V/III ratio varied. Fig. 3.32 shows the effect of the V/III ratio on the surface morphology of AlN epilayers. At the highest V/III ratio investigated, the growth switched completely from two dimensional into an island growth mode. Obviously, the increased concentration of N-species in growth chamber decreases the surface mobility of adsorbed Al-species.

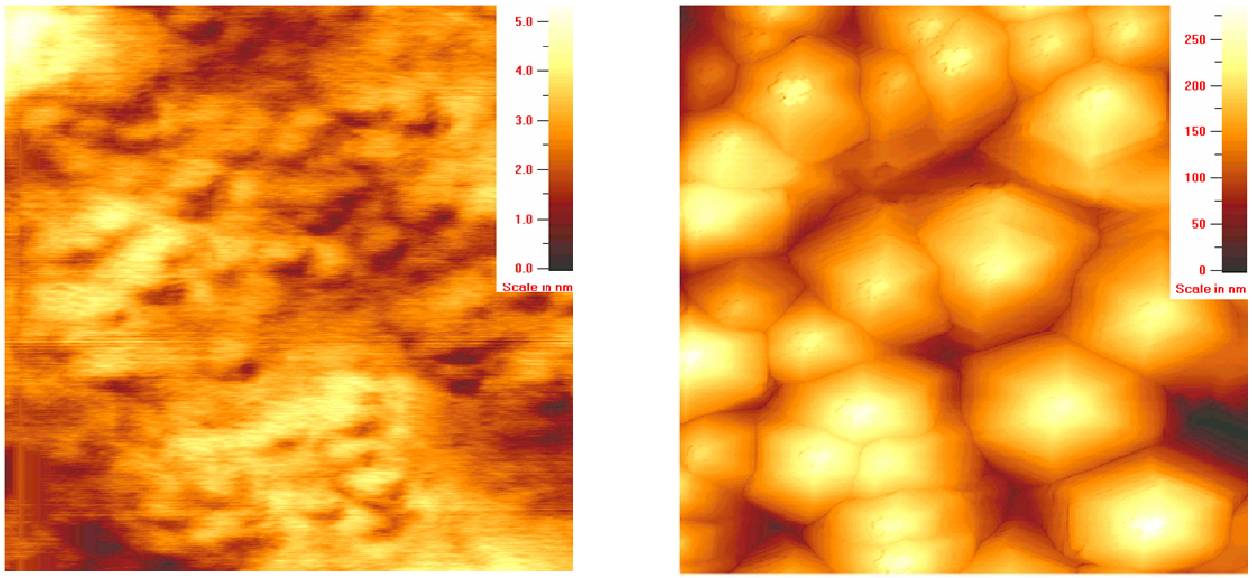

(a) (b)

Figure 3.32 AFM images of a 1μm AlN epilayers with different V/III ratios (a) 5000 and (b) 6850. Smooth surface with RMS = 0.5 nm is observed in (a). Three dimensional growth is evident in (b).

After the optimization of the growth conditions for high temperature AlN epilayer, a 1 μm thick AlN epilayer is grown with V/III ratio of 5000 and growth temperature 1325 ^{0}C for the high temperature AlN epilayers. The surface quality assessed by AFM is shown in Fig. 3.32 (a), with a surface roughness of RMS = 0.5 nm, indicating an atomically smooth surface. To further assess the surface quality, an etch pit density study is performed. The AlN epilayer is etched for 10 min in a 60 % KOH solution heated to 80 ^{0}C. The etched surface is measured by AFM and the result is shown in Fig. 3.33. An average etch pit density of $9x10^7$ cm^{-2} was obtained.

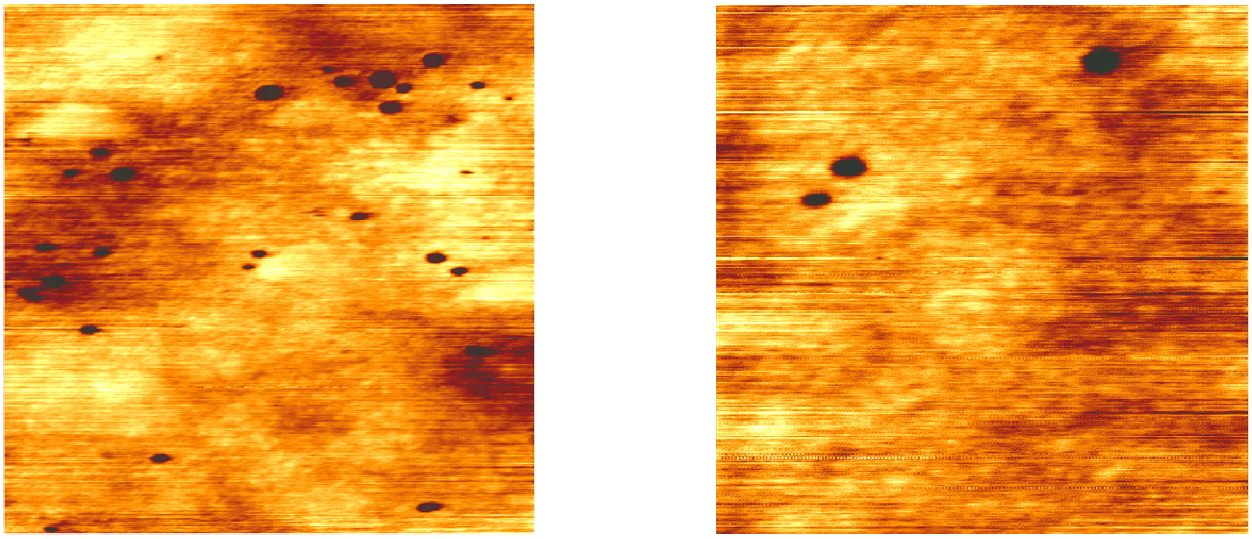

(a) (b)

Figure 3.33 AFM images of KOH-etched AlN epilayer. (a) 5 x 5 μm^2 image and (b) 2 x 2 μm^2 image.

Figure 3.34 shows the low temperature (10 K) PL spectra of AlN epilayers grown on (a) SiC and (b) bulk AlN substrates measured in the energy range from 2.4 to 6.2 eV. Each PL spectrum exhibits a strong band edge emission line. Compared to the spectral peak position of the band edge emission line in the AlN grown on AlN bulk crystal (AlN/AlN), the band edge emission peak of AlN epilayer grown on SiC (AlN/SiC) is red-shifted due to tensile strain.

To reveal detailed features, the low temperature (10 K) band edge emission spectra are re-plotted in a small spectral range from 5.8 to 6.2 eV. In this energy range, AlN/SiC and AlN/AlN (Fig. 3.35 (a) and (b) respectively) show two emission lines. The higher energy emission line at 5.974 eV in AlN/SiC (Fig. 3.35(a)) and at 6.029 eV (Fig. 3.35(b)) in AlN/AlN can be assigned to the free exciton (FX) recombination. Based on the known value of about 16 meV for the binding energy of the bound-excitons in AlN epilayers grown on sapphire [148], we assign the emission line at about 17 meV below the FX transition (5.957 eV in AlN/SiC and 6.012 eV in AlN/AlN) to donor-bound exciton (I_2) transition. The strong I_2 transition in both AlN spectra indicates the presence of high unintentional donor impurity concentrations. The impurities could be oxygen and silicon in AlN/AlN and AlN/SiC, respectively. The presence of these impurities may be due to the diffusion of oxygen and silicon atoms from AlN and SiC substrates to the top AlN epilayer during the epitaxial growth.

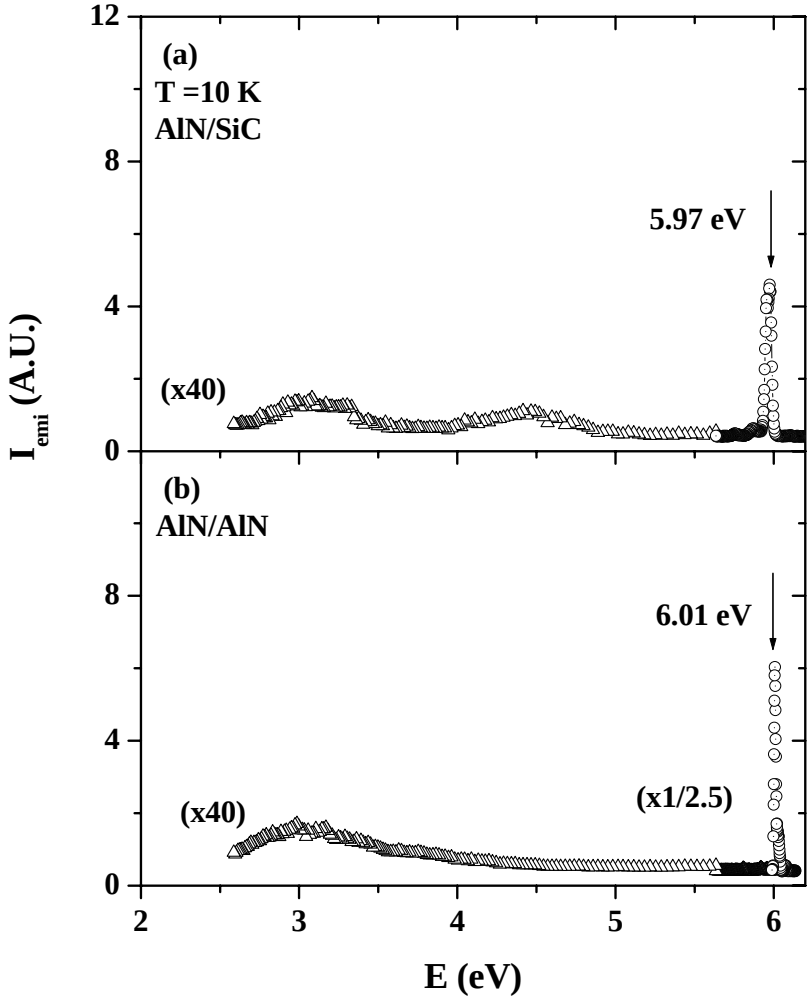

Figure 3.34 10 K PL spectra of (a) AlN/SiC and (b) AlN/AlN, measured in a broad spectral range from 2.4 to 6.2 eV.

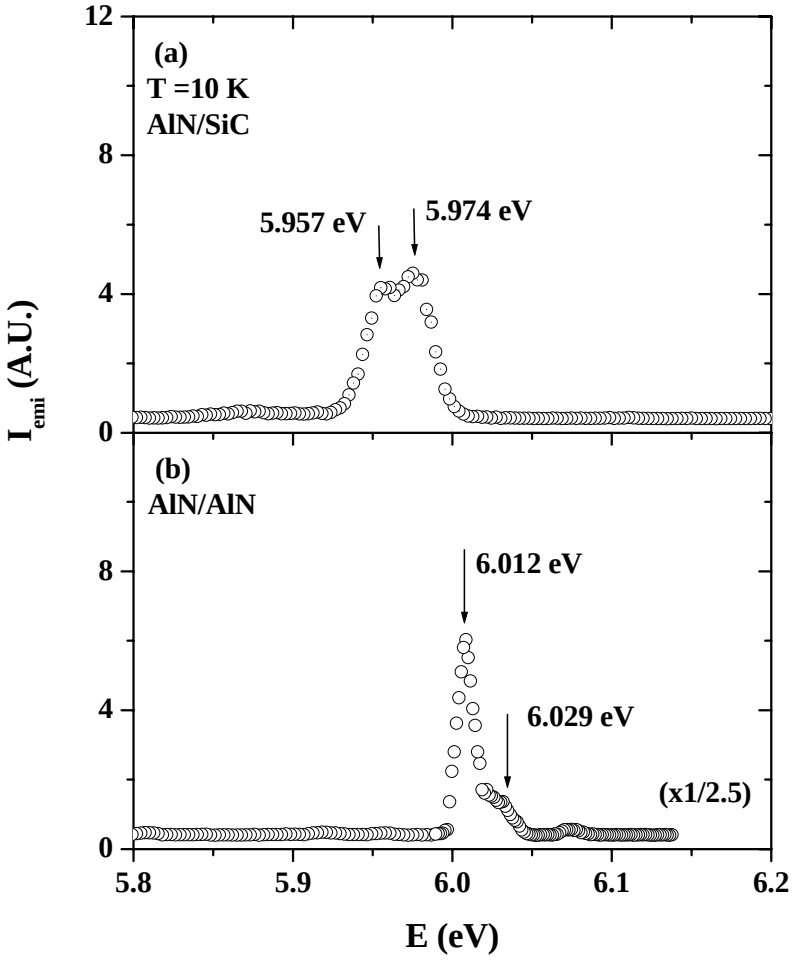

Figure 3.35 10 K PL spectra of (a) AlN/SiC and (b) AlN/AlN, measured in a small spectral range from 5.8 to 6.2 eV.

The structures of AlN epilayers grown on n-type 4H-SiC were used to fabricate AlN/SiC Schottky photodetectors with excellent performance [149].

In summary, the growth of AlN epilayers on n-type 4H-SiC substrates was investigated. A smooth crack free AlN epilayers with high optical and crystalline structural quality were achieved. Because of its high quality, AlN was used as the active layer in the hybrid Schottky photodetector. Also, AlN was used as a template for the growth of highly conductive silicon doped $Al_{0.75}Ga_{0.25}N$ epilayers as will be shown in the next chapter. Further effort is required to improve the material quality.

3.6 Highly conductive n-type $Al_{0.75}Ga_{0.25}N$ alloys grown on SiC substrates

AlGaN alloys are recognized as promising materials for applications in optoelectronic devices in deep ultraviolet (UV) spectral range. Highly conductive (p- and *n*-type) AlGaN alloys are essential for many device applications. Although *n*-type AlN by Si doping with a Si energy level ranging from 86 to 250 meV has been reported [150 -153], further improvements in the material quality and conductivity are still needed for many device applications. One of the major difficulties in obtaining highly conductive *n*-type Al-rich AlGaN alloys is the effect of trapping of electrons by cation vacancies $(V_{III})^{3-}$ and their complexes. Suppressing such intrinsic defects could significantly improve the conductivity and material quality of Al-rich AlGaN alloys [150-159].

Dislocations may also introduce acceptor-like centers through dangling bonds along the dislocation line [160]. Deepening of the Si impurity level as a function of Al composition is another reason as to why the electrical conductivity of n-type AlGaN layers decreases when the Al concentration increases [161]. Indium-silicon co-doping of high Al-content AlGaN layers at relatively low temperatures ~ (920-950) ^{0}C has been reported to result in high electron concentrations and low resistivities [162, 163]. There are a number of hypotheses as to why indium improves the electrical conductivity of Si-doped AlGaN layers. Indium incorporation results in a reduction of threading dislocation (TD) density and causes the annihilation of the defects in the epilayers [164]. This improvement in the crystalline quality can result in higher conductivity through suppression of the dislocation-induced compensation sites. Indium may counteract the incorporation of defects responsible for self-compensation of high Al-content AlGaN layers, such as DX centers and cation vacancies [165].

In this chapter, we studied the effects of using indium as a surfactant during the MOCVD growth of Si-doped $Al_{0.75}Ga_{0.25}N$ epilayers at relatively high temperature ~ 1050 ^{0}C. In addition to significantly increasing the doping efficiency, as shown by room temperature (RT) Hall measurements, the flow of In during the growth also allows for the direct deposition of a crack-free 800 nm thick Si-doped $Al_{0.75}Ga_{0.25}N$ epilayer over a 1μm thick AlN template layer on c-plane SiC substrates. Atomic Force Microscopy (AFM) images show clearly that In as a surfactant plays a role in eliminating the defects by reducing the surface pits density. RT

photoluminescence (PL) measurements show a clear correlation between emission intensity of the defect related transition and TMIn flow rate. X-ray diffraction (XRD) shows correlation between TMIn flow rate and screw dislocation density through the reduction of the full width at half maximum (FWHM) of (002) rocking curves.

Figure 3.36 shows the general layer structure for Si-doped $Al_{0.75}Ga_{0.25}N$ epilayers of about 0.8 μm in thickness grown on AlN/SiC templates by MOCVD. Undoped AlN epilayers of thickness ~ 1 μm were first grown on the c-plane (001) of SiC substrates as templates followed by the growth of 0.8 μm Si-doped $Al_{0.75}Ga_{0.25}N$ epilayers. Trimethylaluminum (TMAl), trimethylgallium (TMGa), trimethylindium (TMIn), and blue ammonia were used as sources for aluminum, gallium, indium, and nitrogen, respectively. For the silicon dopant, silane (SiH_4) was transported into the reactor. The growth temperature and pressure for the Si-doped $Al_{0.75}Ga_{0.25}N$ epilayers were about 1050 ^{0}C and 70 Torr, respectively. Fig. 3.37 shows the entire temperature profile of complete growth. High quality, undoped AlN epilayer template plays an important role to reduce dislocations in subsequent Si doped AlGaN layer [166]. During the growth of Si-doped $Al_{0.75}Ga_{0.25}N$ layer, TMIn was introduced into the gas stream. TMIn flow was intentionally varied as 0, 18, 24, 30 ml/min, which corresponds to (0, 1.55, 2.06, 2.58) μmol/min while keeping other growth conditions the same. RT Hall effect (standard Van der Pauw) measurement was employed to study the electrical properties of these epilayers: electron concentration, mobility, and resistivity. AFM was used to study the morphology of the layers surfaces. RT-PL measurements were performed to investigate the optical properties of these samples. XRD was used to determine the Al contents and the crystalline quality.

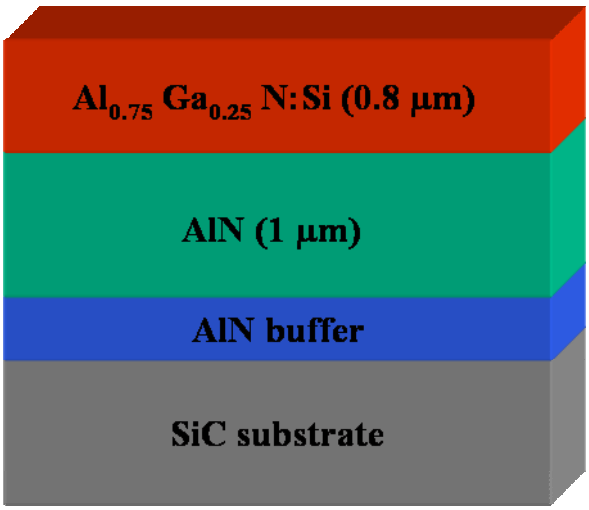

Figure 3.36 Schematic layer structure for the growth of Si-doped $Al_{0.75}Ga_{0.25}N$ epilayer.

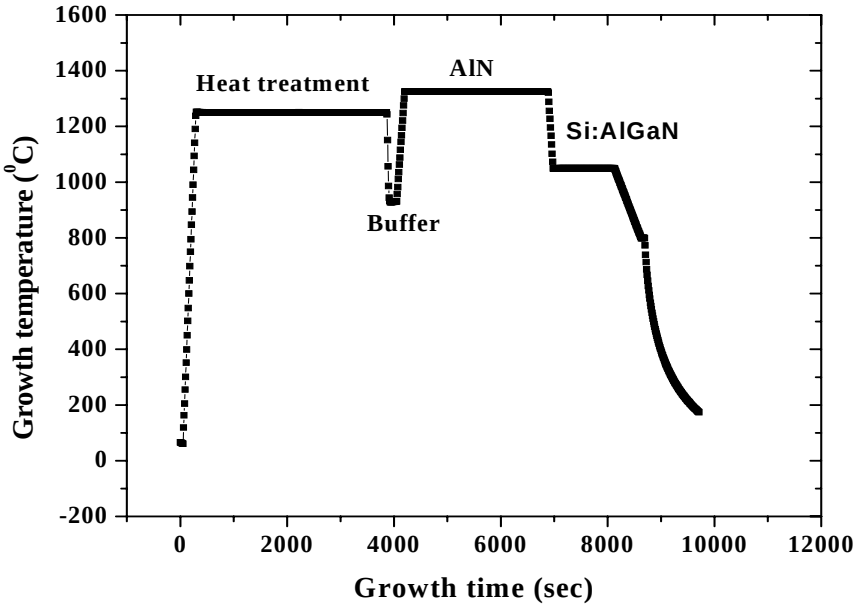

Figure 3.37 The growth temperature profile of Si-doped $Al_{0.75}Ga_{0.25}N$ epilayers.

Figure 3.38 compares the AFM images of the surfaces of these epilayers, with TMIn flow rates of (a) 0, (b) 18, (c) 24, and (d) 30 ml/min. The measured RMS roughness over the 10 x 10 μm^2 scans ranges between 1.2 to 1.5 nm. The surface of the epilayer without TMIn flow in (a) is characterized by high density of nanometer-scale surface pits (dark spots). These surface pits are associated with the surface termination of threading dislocations [167, 168]. As seen in the AFM images from (a) to (d), increasing TMIn flow rate reduces the density of surface pits. This could be a result of enhancing the adatom mobility of group III atoms.

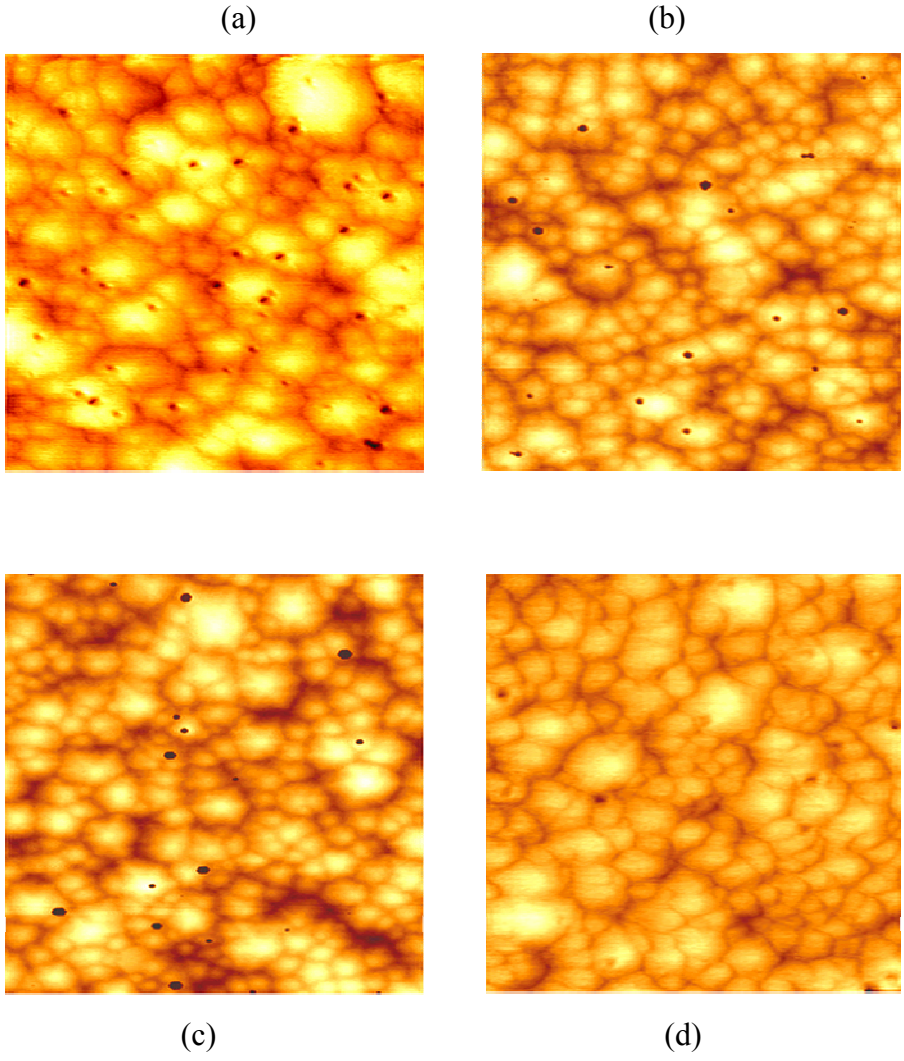

Figure 3.38 AFM images of 0.8 µm thick Si-$Al_{0.75}Ga_{0.25}N$ showing change in density of surface pits with TMIn flow rate (a) 0, (b) 18, (c) 24, (d) 30 ml/min.

Fig. 3.39 compares the room temperature PL spectra corresponding to the series of epilayers shown in Fig. 3.38. All samples were scanned from 2 to 6 eV to probe impurity transitions as well as band-edge transition. The dominant band edge emission peaks at 5.20 eV of these spectra are due to the localized exciton recombination in the AlGaN epilayers [169, 170]. In addition to the band edge emission peak, the emission spectra of all these samples comprise a deep level impurity transition at 3.2 eV, which has been previously identified and is assigned to the recombination between shallow donors and cation vacancy complexes with two-negative charge, $(V_{III}\text{-complex})^{2-}$ [171]. There is clear correlation between the intensity of the $(V_{III}\text{-complex})^{2-}$ related impurity emission and the TMIn flow rate. Increasing TMIn flow rate decreases the intensity of the deep level impurity transition.

Room temperature Hall effect measurements reveal that the conductivity and electron concentration of the Si-doped $Al_{0.75}Ga_{0.25}N$ alloys increase with increasing TMIn flow rate. The mobility decreases slightly by increasing the TMIn flow rate. The increase of electron concentration is directly related with reduced cation vacancy complexes. As shown in Fig. 3.39 the intensity of deep level impurity transition is decreased with increasing TMIn flow rate, which indicates that indium as a surfactant counteracts the incorporation of defects responsible for the self compensation of high-Al mole fraction AlGaN layers. The slight reduction of the mobility could be due to the increased of the electron-electron scattering, due to the enhanced free electron concentration, which has been confirmed both for GaN epilayers and AlGaN alloys. The Hall effect measurements results are summarized in Table 2.

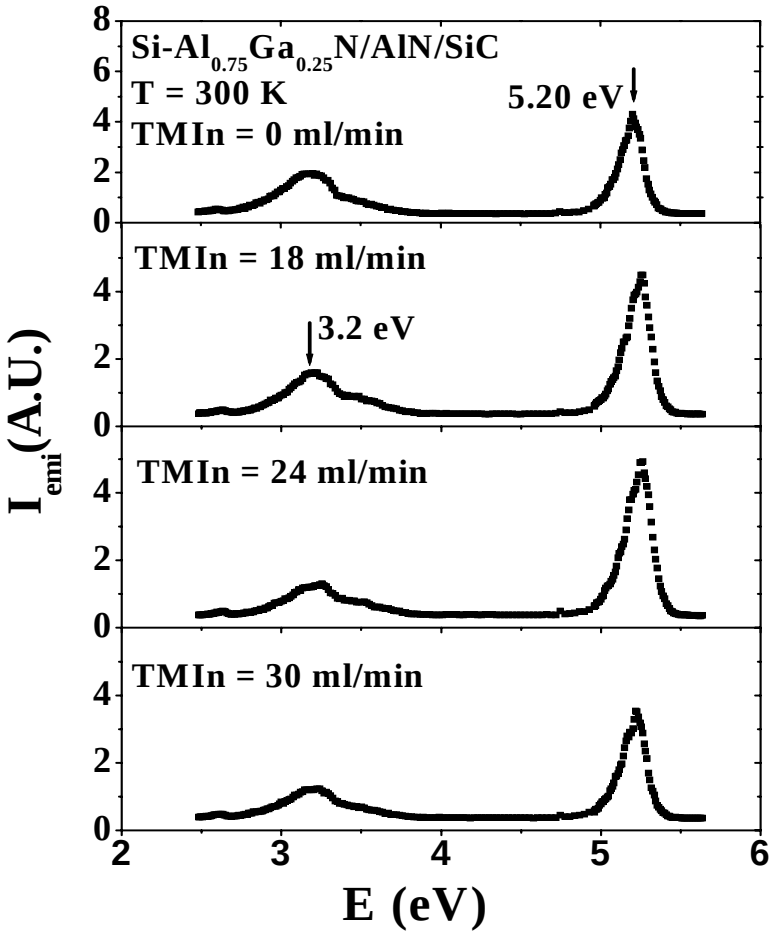

Figure 3.39 Room temperature PL spectra of 0.8 μm thick Si-$Al_{0.75}Ga_{0.25}N$ showing change in intensity of deep level impurity transition at 3.2 eV with TMIn flow rate.

Table 3.1 Resistivity ρ, electron concentration n, and mobility μ as functions of TMIn flow rate.

TMIn (ml/min)	ρ (Ω.cm)	n (cm^{-3})	μ (cm^2/Vs)
0	0.044	$5.6x10^{18}$	26.0
18	0.038	$7.3x10^{18}$	24.0
24	0.032	$8.1x10^{18}$	23.3
30	0.027	$9.5x10^{18}$	21.1

The XRD rocking curve of the (002) peak is measured and shown in Fig. 3.40. The full width at half maximum (FWHM) of the (002) peak is reduced with increasing TMIn flow rate, which indicates that the presence of TMIn improves the crystalline quality of Si-doped $Al_{0.75}Ga_{0.25}N$. From the FWHM of the symmetric scan the screw dislocation density can be evaluated [172]. The screw dislocation density reduced from 2.18 x 10^8 cm^{-2} to 1.12 x 10^8 cm^{-2} for TMIn flow rate increases from 0 to 30 ml/min.

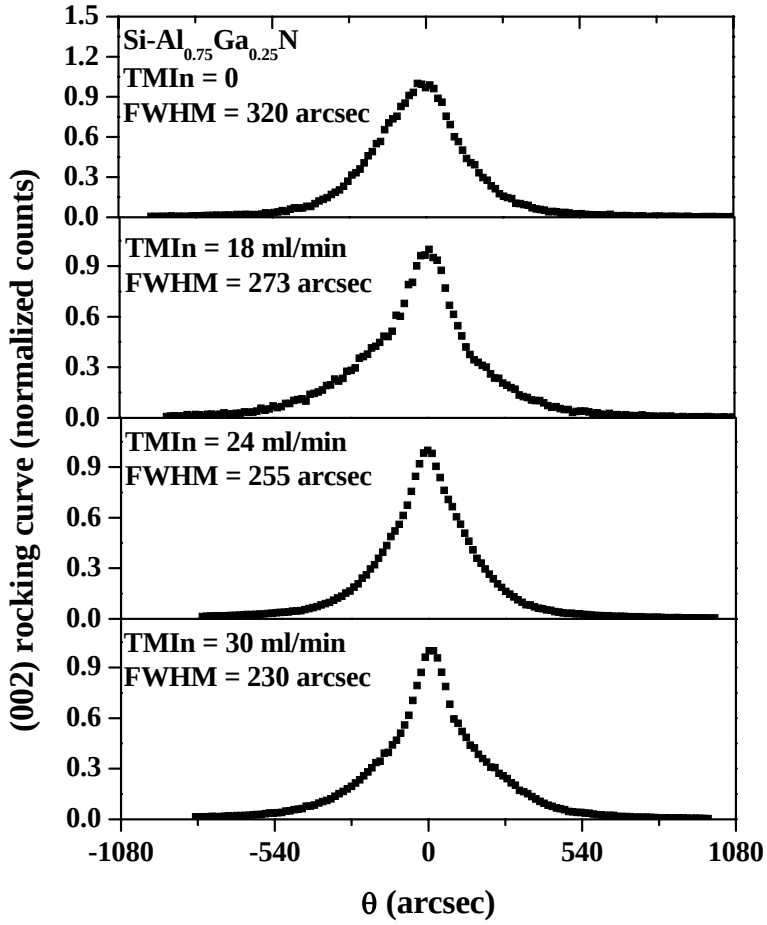

Figure 3.40 (002) rocking curves of Si-$Al_{0.75}Ga_{0.25}N$ showing line width changing with TMIn flow rate.

To see the correlation between the intensity of deep level impurity transition and the screw dislocation density, in Fig. 3.41, we plotted the intensity of the deep level impurity as a function of the screw dislocation density. As can be seen, there is a clear correlation between the intensity of the deep level impurity and the density of screw dislocations.

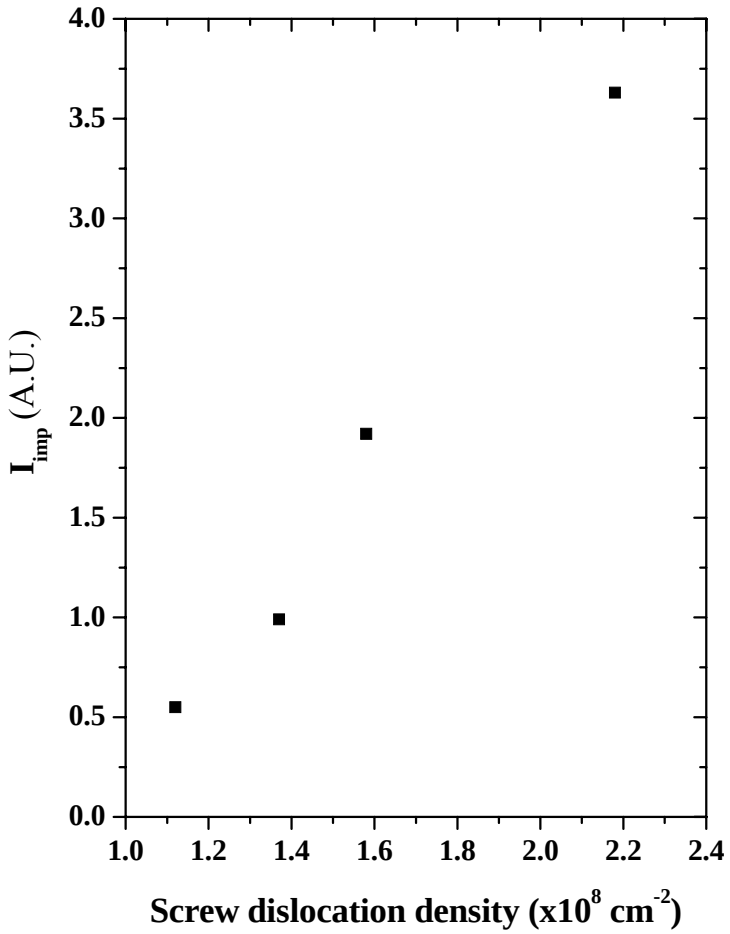

Figure 3.41 Intensity of the deep level impurity transition at 3.2 eV as a function of the screw dislocation density.

Figure 3.42 summarizes the effect of TMIn flow on optical, electrical, and crystalline quality of Si-$Al_{0.75}Ga_{0.25}N$ epilayers. Improvement in the over all quality of the material is evident.

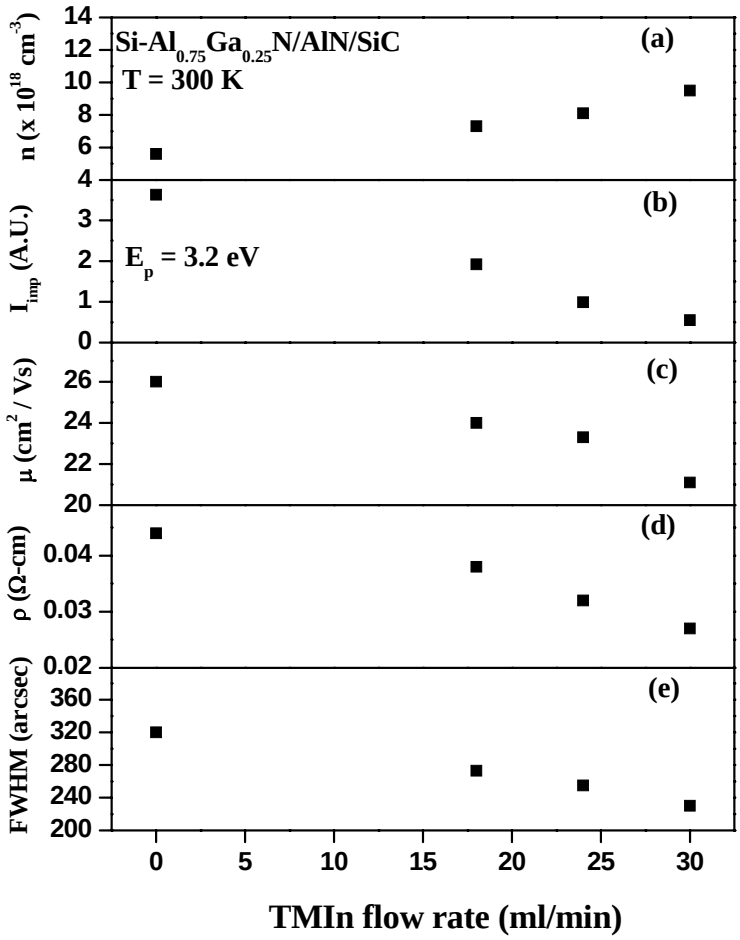

Figure 3.42 Variations of the (a) electron concentration, n, (b) intensity of deep level impurity transition at 3.2 eV, I_{imp}, (c) mobility, μ, (d) resistivity, ρ, and (e) full width at half maximum (FWHM) of (002) rocking curve with TMIn flow rate during the growth of Si-doped $Al_{0.75}Ga_{0.25}N$ alloys.

In summary, using indium as a surfactant during the growth of Si-doped $Al_{0.75}Ga_{0.25}N$ epilayers, improves the electrical quality of the epilayers. Indium as surfactant counteracts the incorporation of defects responsible for self-compensation of high Al-content AlGaN layers, such as cation vacancies as shown from PL spectra of these epilayers.

3.7 MOCVD growth of p-type Beryllium doped GaN

III-nitride semiconductors are currently being used in a wide variety of electronic and optoelectronic devices. Controllable doping is essential for all of these devices. For *n*-type doping of nitrides, Silicon can be successfully used as dopant, and carrier concentrations exceeding ($5x10^{20}$) cm^{-3} can be achieved [10]. The situation is less favorable for *p*-type doping. Magnesium is the acceptor of choice; it can be incorporated in concentrations up to about 10^{20} $cm^{-3,}$ but because of its large ionization energy ~160 meV, the resulting room-temperature hole concentration is only about 10^{18} cm^{-3}, i.e., only about 1% of Mg atoms are ionized at room temperature. Increasing the Mg concentration beyond 10^{20} cm^{-3} leads to a saturation and decrease in the hole concentration [11]. It was proposed that the Mg solubility limit is the main cause of this behavior [12]. The limited conductivity of *p*-type doped layers constitutes an impediment for progress in device applications. It would be desirable to identify an alternative acceptor that would exhibit higher solubility and/or lower ionization energy. Previous computational studies [14–16] have addressed a variety of candidate acceptors, including Li, Na, K, Be, Zn, Ca, and Cd. Only Be emerged as a viable acceptor, exhibiting higher solubility and lower ionization energy than Mg. However, it also emerged that self-compensation may occur due to incorporation of Be on interstitial sites, where it acts as a donor [15]. The conclusions of the theoretical work seem promising enough.

Experimentally, Be doping of GaN in molecular beam epitaxy has been reported by various groups [173,174]. Another technique for Be incorporation that has been attempted is ion implantation [175,176]. No electrical conductivity results were reported; characterization was mostly by optical spectroscopy measurement. A PL peak just below the band edge of GaN was found and attributed to Be. Assuming that this PL line results from a Be substitutional acceptor, an acceptor ionization energy can be extracted but this has resulted in a wide range of values, ranging from 90 to 250 meV, depending on the assumptions made in the analysis [13]. To the best of our knowledge, there have not been any reports on the growth of Be doped GaN using MOCVD.

The objective of this work is to experimentally investigate if Be can be an alternative acceptor in GaN using MOCVD growth technique.

Figure 3.43 shows the general layer structure for Be-doped GaN epilayers of 1µm in thickness grown on GaN/Al_2O_3 templates by MOCVD. Insulating undoped GaN epilayers of thickness ~ 2 µm were first grown on the c-plane (001) of Al_2O_3 substrates as templates followed by the growth of 1 µm Be-doped GaN epilayers. TMGa, and blue ammonia were used as sources for gallium and nitrogen, respectively. For the beryllium dopant, Be was transported into the reactor. The starting growth temperature and pressure for the Be-doped GaN epilayers were the same as that for Mg-doped GaN, i.e. about 1040 ^{0}C and 350 Torr, respectively.

Due to the low vapor pressure of the Be source, the temperature of the Be source was increased to 70 ^{0}C. A systematic study on Be flow was done by varying Be flow rate from 125-750 ml/min. Annealing conditions same as that for Mg-doped GaN were used to anneal Be-doped GaN samples. RT Hall effect (Standard Van der Pauw) measurement was employed to study the electrical properties of this set of epilayers. All the samples were highly resistive. In this Be flow rate range there was no big change in the surface morphology (RMS ~ 3 nm) and the crystalline quality of the material ((002) rocking curve with FWHM ~ 450 arcsec).

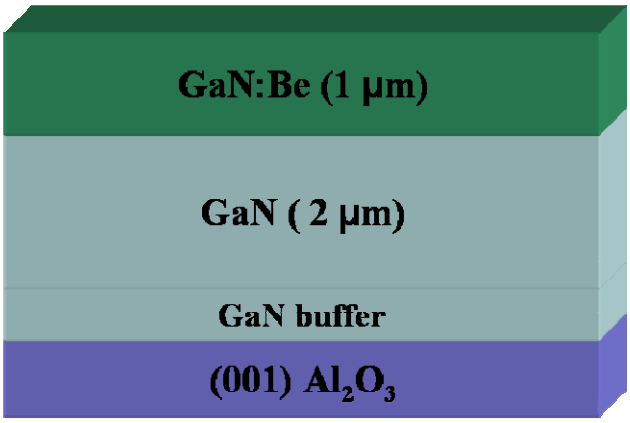

Figure 3.43 Schematic layer structure for the growth of Be-doped GaN epilayer.

Fig. 3.44 shows the Be concentration profile as measured by SIMS for the sample with Be source flow rate of 75 ml/min. The result indicates a Be dopant concentration of about 2.5 x 10^{18} cm^{-3} in the epilayer. The Be concentration for other samples was calibrated assuming a linear relationship between the measured Be concentration and Be source gas flow rate.

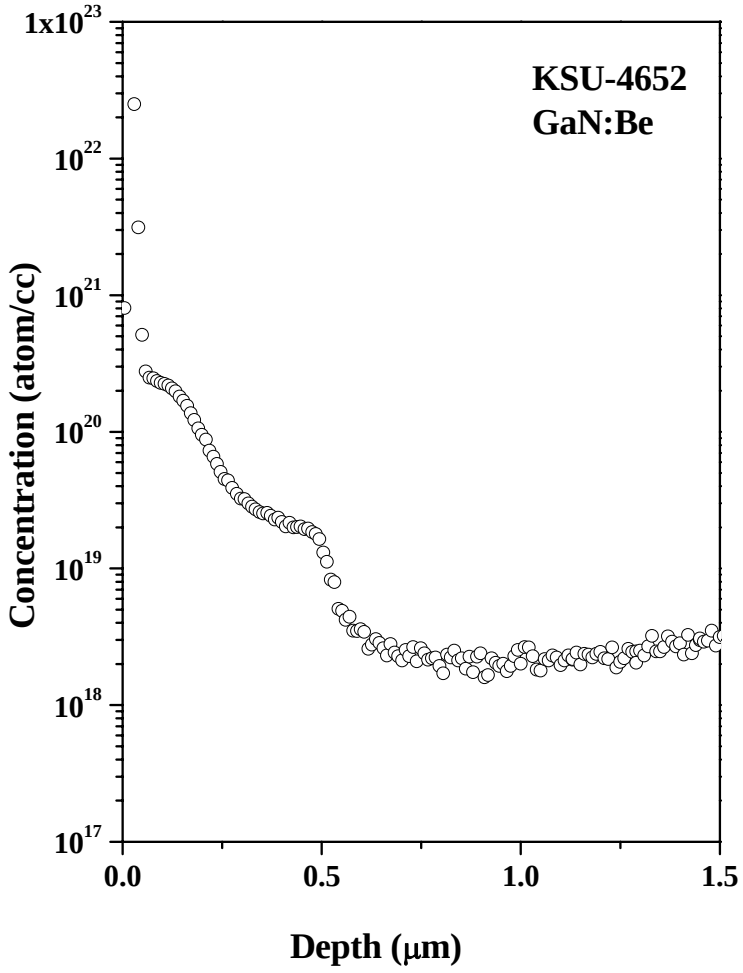

Figure 3.44 Beryllium dopant concentration profile in GaN epilayer with Be source flow rate of 75 ml/min, as probed by SIMS (performed by Charles Evans & Associate).

The optimization of growth conditions was done to improve the conductivity of the material. The effects of the growth temperature, pressure, flow rate of H_2 carrier gas, NH_3, and the TMGa were investigated. The results showed that the growth conditions of Be doped GaN are totally different from that of the Mg doped GaN, the main differences are in the growth temperature and pressure. By using a growth temperature of around 1100 ^{0}C and a pressure of 40 Torr, p-type conduction has been achieved, as confirmed by RT Hall measurement.

As grown Be doped epilayers were highly resistive and post growth rapid thermal annealing was done to activate Be acceptors. The annealing condition was taken to be same as that for Mg acceptor activation. Ni/Au was used to make contacts in the standard Van der Pauw configuration for Hall-effect measruments. The resistivity obtained at RT is about 3.7 Ω.cm. Variable temperature Hall-effect measurements were attempted to probe the electrical properties of Be doped GaN epilayers. Fig. 3.45 shows the Arrhenius plot of the resistivity (ρ) of Be doped GaN epilayer. The resisitivity decreases with increasing temperature. The solid line is the least squares fit of data with Eq. (3.1). The fitted value of the activation energy (E_A) is about 118 ± 4 meV, which is around 40 meV smaller than the E_A of Mg.

The measured values of hole concentration and mobility were fluctuating randomly, so we were not able to use the hole concentration to evaluate the activation energy. This fluctuation could be related to the unoptimized annealing conditions of the material and the contacts. So more studies are needed to optimize these annealing conditions.

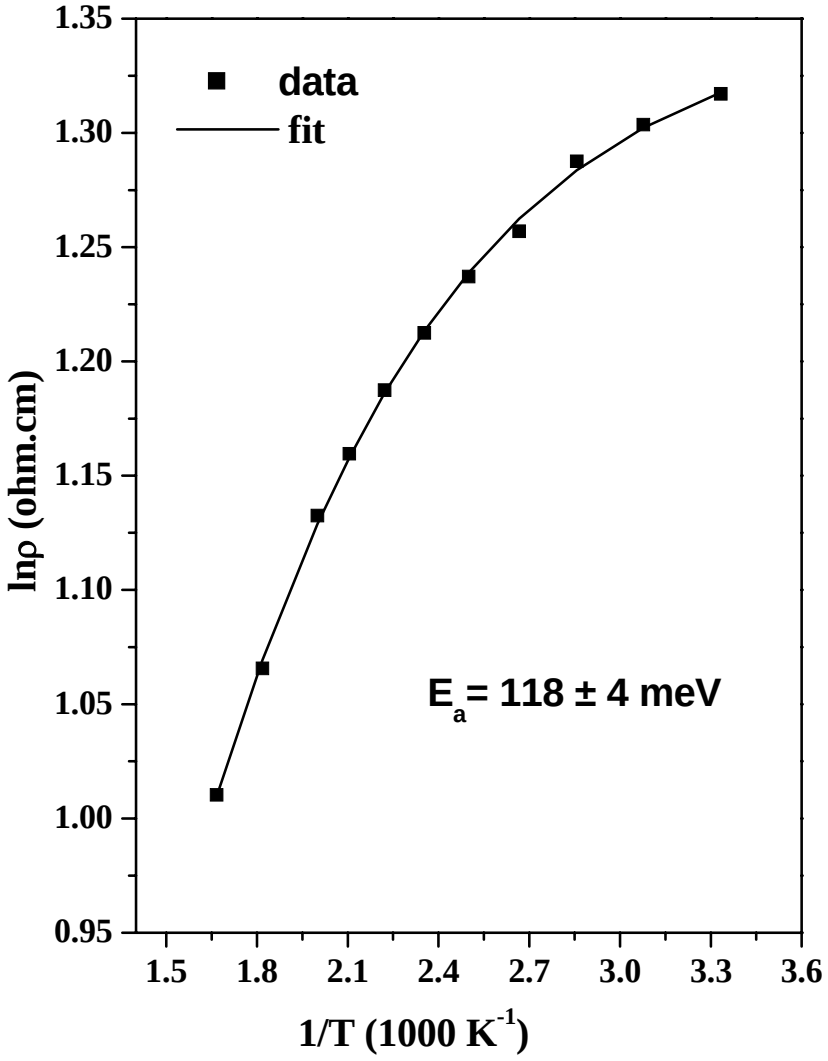

Figure 3.45 The Arrhenius plot of resistivity (ρ) obtained for the Be doped GaN epilayers. The solid line is the least-square fit of data with Eq. (3.1). The fitted value of the activation energy (E_A) is 118 ± 4 meV.

Increasing the growth temperature of the Be doped GaN epilayers from 1040 to 1100 ^{0}C has critical effect in obtaining p-type conductivity but at the same time it has detrimental effect on the surface morphology. Fig. 3.46 shows the effect of growth temperature on the surface morphology of Be doped GaN epilayers. At growth temperature 1040 ^{0}C the surface of Be doped epilayer is relatively smooth with RMS ~ 3 nm and the material is highly resistive. At growth temperature 1100 ^{0}C the surface is rough with RMS ~ 8 nm and the material is conductive.

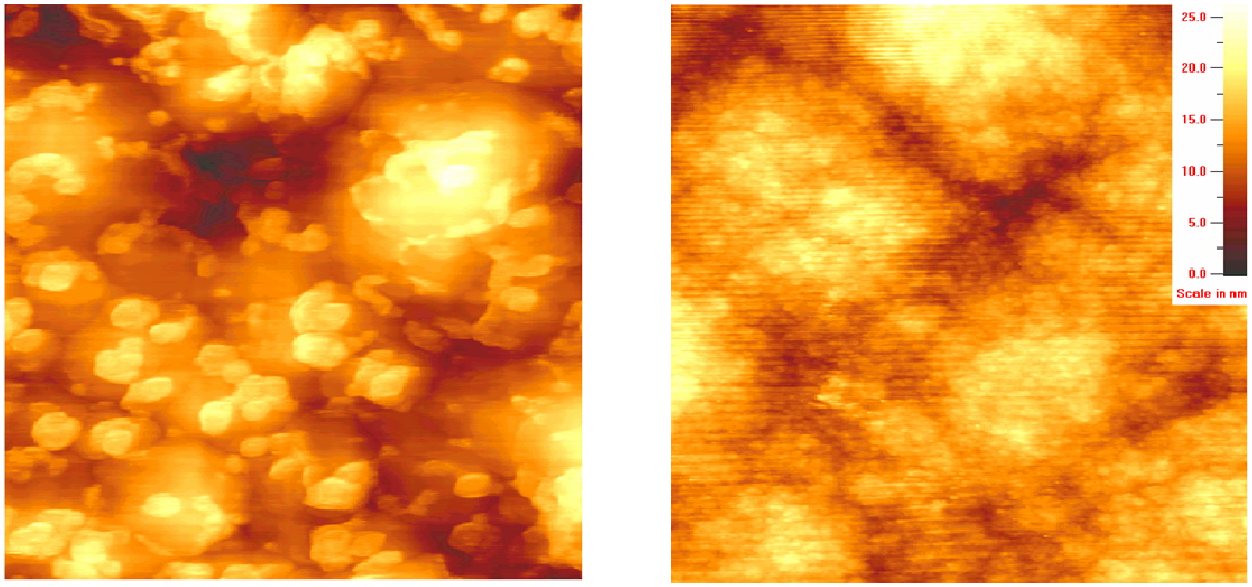

(a) (b)

Figure 3.46 AFM images of Be doped GaN epilayers with different growth temperatures (a) 1100 ^{0}C and (b) 1040 ^{0}C. Rough surface with RMS = 8 nm is observed in (a). Relatively smooth surface with RMS = 3 nm is observed in (b).

In summary, p-type conductivity has been obtained in Be doped GaN by MOCVD. The activation energy of Be acceptor was estimated to be 118 ± 4 meV, which is about 40 meV less than the activation energy of Mg acceptor in GaN. More growth is needed to optimize the surface morphology of the p-type epilayers. Also more studies are needed to optimize the annealing conditions of the Be doped GaN epilayers and the contacts, which is expected to significantly improve the electrical properties.

CHAPTER 4 - General Conclusions

Al-rich AlN/AlGaN epilayers and quantum wells were grown by metaorganic chemical vapor deposition (MOCVD). The materials were characterized by deep UV photoluminescence (PL), X-ray diffraction (XRD), atomic force microscope (AFM), scanning electron microscope (SEM), optical microscope, and Hall-effect measurements. A comprehensive study has been done on the effect of the polarity on the growth materials. The polarity of the material is determined in the early stages of the growth, which shows how critical it is to control the timing of introducing gases and sources to the MOCVD chamber, especially when we are using high temperature buffer layers. The growth polarity strongly influences the surface morphology, structural, optical, and electrical properties of high Al-content AlGaN epilayers. The Al-polar $Al_xGa_{1-x}N$ epilayers possess a better surface morphology and crystalline quality compared with those of N-polar $Al_xGa_{1-x}N$ epilayers. Low temperature PL spectra of Al-polar $Al_xGa_{1-x}N$ alloys exhibit only the band edge transition. In contrast, the PL spectra of N-polar $Al_xGa_{1-x}N$ epilayers comprise an additional deep level impurity transition, which was assigned to the recombination between a shallow donor and $(V_{III}\text{-complex})^{1-}$. Unintentional impurities related to C and O are more readily incorporated into N-polar AlGaN epilayers.

A set of polar $AlN/Al_{0.65}Ga_{0.35}N$ QWs with L_w varying from 1 to 3 nm was grown on c-plane sapphire substarte. A systematic dependence of the PL emission peak position on L_w was observed, from which a value of ~ 4 MV/cm for the polarization fields in $AlN/Al_{0.65}Ga_{0.35}N$ QWs was deduced. The PL emission line width was found to increase linearly with L_w. Furthermore, our results have shown that highest quantum efficiency (QE) was obtained in $AlN/Al_{0.65}Ga_{0.35}N$ QWs with well width between 2 and 2.5 nm, which served as a guideline for designing optimal deep UV light emitter structures.

A- and *c*-plane $AlN/Al_{0.65}Ga_{0.35}N$ QWs have been grown and their PL emission characteristics were measured and compared. The low temperature PL characteristics of *a*-plane QWs are primarily governed by the quantum size effect. In contrast, the emission characteristics of *c*-plane QWs are affected by strong polarization fields in addition to the quantum confinement effect. The PL decay time was weakly dependent on the well width, L_w, for *a*-plane QWs. However, a strong dependence of the PL decay time on L_w was observed for *c*-plane QWs,

which is caused by the variation of the polarization fields in QWs due to varying L_w. The thermal quenching of PL emission in both *a*- and *c*-plane QWs is attributed to the activation of excitons from localized states. In order to obtain highest QE, *a*- and *c*-plane AlN/AlGaN QWs with high Al contents should be designed to have $L_w > 2$ nm and $L_w \approx 2$ nm, respectively. The results thus suggested that the *a*-plane AlN/AlGaN QW system potentially provides a much greater flexibility for the device structural design than its *c*-plane counterparts.

A-plane AlN epilayers have been grown on *r*-plane sapphire substrates by MOCVD. It was observed that (1) the bandedge emission intensity of *a*-plane AlN is comparable to that of *c*-plane AlN and (2) Mg energy levels in *a*- and *c*- plane AlN epilayers are the same and around 0.5 eV. We believe that much improvement in material quality of *a*-plane AlN can be achieved by further optimizing the growth processes, which would provide significant enhancement in emission efficiency. These results point out that *a*-plane AlN template can be utilized to build UV optoelectronic devices possessing minimal effects of polarization fields and enhanced surface emission.

The growth of c-plane AlN epilayers on 4H-SiC substrates was investigated in detail. A smooth crack free AlN with high optical and crystalline structural quality was achieved. Because of its high quality, AlN was used as active layer in hybrid Schottky photodetector, which showed excellent performance; also AlN/4H-SiC was used as template for the growth of highly conductive Si-$Al_{0.75}Ga_{0.25}N$ epilayers. Further improvement in material quality is required to have better device performance.

We investigated the effects of using indium as a surfactant during the MOCVD growth of Si-doped $Al_{0.75}Ga_{0.25}N$ epilayers at relatively high temperature ~ 1050 ^{0}C. In addition to significantly increasing the doping efficiency as shown by room temperature (RT) Hall-effect measurements, the flow of In during the growth also allowed for the direct deposition of a crack-free 800 nm thick Si-doped $Al_{0.75}Ga_{0.25}N$ epilayer over a 1μm thick AlN template layer on c-plane SiC substrates. AFM images showed clearly that indium as a surfactant plays a role in eliminating the defects by reducing the surface pits density. RT PL measurements showed a clear correlation between emission intensity of the defect related transition and TMIn flow rate. XRD showed correlation between TMIn flow rate and screw dislocation density through the reduction of the full width at half maximum of (002) rocking curves.

A p-type conductivity was achieved in beryllium (Be) doped GaN by MOCVD. The activation energy of Be acceptor was estimated to be 118 ± 4 meV, which is about 40 meV less than the activation energy of Mg acceptor in GaN. More growth is needed to optimize the surface morphology of the p-type epilayers. Also more studies are needed to optimize the annealing conditions of the Be doped GaN epilayers and the contacts, which is expected to significantly improve the electrical properties.

References

[1] T. P. Chow and R. Tyagi, IEEE Trans. Electron Devices **41**, 1481 (1994).

[2] M. Asif Khan, Q. Chen, J. W. Yang, M. S. Shur, B. T. Dermott, and J. A. Higgins, IEEE Electron Device Lett. **17**, 325 (1996).

[3] S. Nakamura and G. Fassal, The Blue Laser Diode (Springer, New York, 1997).

[4] L. F. Eastman and U. K. Mishra, IEEE Spectr**. 39**, 28 (2002).

[5] S. Nakamura, IEEE, Circuits and Devices, May, 19 (1995).

[6] T. Matsuoka, H. Okamoto, M. Nakao, H. Hiama, and E. Kurimoto, Appl. Phys. Lett. **81**, 1246 (2002).

[7] O. Ambacher, J. Smart, J. R. Shealy. N. G. Wiemann, K. Chu, M. Murphy, W. J.Schaff, L. F. Eastman, R. Dimitrov. L. Wittmer, M. Stutzman, W. Rieger, and J. Hilsenbeck. J. Appl. Phys. **85**, 3222 (1999).

[8] F. Bernardini, V. Fiorentini, and D. Vanderbilt, Phys. Rev. B **56**, R10024 (1997).

[9] P. Misra, Ph.D. Thesis, University of Berlin (2005).

[10] W. Go¨tz, R. S. Kern, C. H. Chen, H. Liu, D. A. Steigerwald, and R. M. Fletcher, Mater. Sci. Eng., B **59**, 211 (1999).

[11] D. P. Bour, H. F. Chung, W. Gtz, L. Romano, B. S. Krusor, D. Hofstetter, S. Rudaz, C. P. Kuo, F. A. Ponce, N. M. Johnson, M. G. Craford, and R. D. Bringans, in III-V Nitrides, edited by F. A. Ponce, T. D. Moustakas, I. Akasaki, and B. Monemar, Mater. Res. Soc. Symp. Proc. No. **449** (Materials Research Society, Pittsburgh, 1997), p. 509.

[12] J. Neugebauer and C. G. Van de Walle, in Gallium Nitride and Related Materials, edited by R. D. Dupuis, J. A. Edmond, F. A. Ponce, and S. Nakamura, Mater. Res. Soc. Symp. Proc. No. **395** (Materials Research Society, Pittsburgh, 1996), p. 645.

[13] G. Van de Walle, S. Limpijumnong, and J. Neugebauer, Phys. Rev. B **63**, 245205 (2001).

[14] V. Fiorentini, F. Bernardini, A. Bosin, and D. Vanderbilt, in Proceedings of the 23rd International Conference on the Physics of Semiconductors, edited by M. Scheffler and R. Zimmermann (World Scientific, Singapore, 1996), p. 2877.
[15] J. Neugebauer and C. G. Van de Walle, J. Appl. Phys. **85**, 3003 (1999).
[16] F. Bernardini, V. Fiorentini, and A. Bosin, Appl. Phys. Lett. **70**, 2990 (1997).
[17] W. C. Johnson, J. Parsons, and M. C. Crew, J. Phys. Chem. **36**, 2561 (1932).
[18] R. Juza and H. Hahn, Z. Anorg. Allgem. Chem. **234**, 282 (1938).
[19] R. Juza and H. Hahn, Z. Anorg. Allgem. Chem. **244**, 133 (1940).
[20] H. P. Maruska and J. J. Tietjen, Appl. Phys. Lett. **15**, 327 (1969).
[21] M. Ilegems and R. Dingle, J. Appl. Phys. **44**, 4234 (1973).
[22] J. I. Pankove, M. T. Duffy, E. A. Miller, and Berkeyhelser, J. Lumin. **8**, 89 (1973).
[23] O. Lagerstedt and B. Monemar, J. Appl. Phys. **45**, 2266 (1974).
[24] B. Monemar, O. Lagerstedt, and H. P. Gislason, J. Appl. Phys. **51**, 625 (1980).
[25] J. I. Pankove and J. A. Hutchby, J. Appl. Phys. **47**, 5387 (1976).
[26] J. I. Pankove, E. A. Miller, and J. E. Berkeyheiser, J. Lumin. **5**, 84 (1972).
[27] W. Seifert, R. Franzheld, E. Butter, H. Sobotta, and V. Riede, Crystal Res. Technol. **18**, 383 (1983).
[28] H. Amano, I. Akasaki, K. Hiramatsu, and N. Koide, Thin Solid Films **163**, 415 (1988).
[29] I. Akasaki, H. Amano, Y. Koide, K. Hiramatsu, and N. Sawaki, J. Cryst. Growth **98**, 209 (1989).
[30] S. Nakamura, Jpn. J. Appl. Phys., Part 2 **30**, L1705 (1991).
[31] S. Nakamura, M. Senoh, and T. Mukai, Jpn. J. Appl. Phys., Part 2 **30**, L1708 (1991).
[32] H. Amano, M. Kito, K. Hiramatsu, and I. Akasaki, Jpn. J. Appl. Phys., Part 2 **28**, L2112 (1989).
[33] S. Nakamura, T. Mukai, M. Senoh, and N. Iwasa, Jpn. J. Appl. Phys., Part 2 **31**, L139 (1992).
[34] S. Nakamura, T. Mukai, M. Senoh, and N. Iwasa, Appl. Phys. Lett. **64**, 1687 (1994).
[35] Organometallic Vapor-Phase Epitaxy: Theory and Practice, G. B. Stringfellow, (Academic Press, Inc., San Diego, 1989).
[36] Jing Li, Ph.D. Thesis, Kansas State University (2003).

[37] Mim Nakarmi, Ph.D. Thesis, Kansas State University (2005).

[38] P. F. Fewster, X-ray Scattering from Semiconductors, 2nd ed. (Imperial College Press, London, 2003).

[39] R. Chierchia, T. Bottcher, H. Heinke, S. Einfeldt, S. Figge, D. Hommel, J. Appl. Phys. **93**, 8918 (2003).

[40] T. Metzger, R. Hopler, E. Born, O. Ambacher, M. Stutzmann, R. Stommer, M. Schuster, H. Gobel, S. Christiansen, M. Albrecht, and H. P. Strunk, Philos. Mag. A **77**,1013 (1998).

[41] Solid State Physics, J. W. Ashcroft and D. N. Mermin,(Holt, Rinehart, and Winston, New York, 1976).

[42] J. P. Zhang, A. Chitnis, V. Adivarahan, S. Wu, V. Mandavilli, R. Pachipulusu, M. Shatalov, G. Simin, J. W. Yang, and M. Asif Khan, Appl. Phys. Lett. **81**, 4910 (2002).

[43] A. Yasan, R. McClintock, K. Mayes, D. Shiell, L. Gautero, S. R. Darvish, P. Kung, and M. Razeghi, Appl. Phys. Lett. **83**, 4701 (2003).

[44] A. Hanlon, P. M. Pattison, J. F. Kaeding, R. Sharma, P. Fini, and S. Nakamura, Jpn. J. Appl. Phys., Part 2 **42**, L628 (2003).

[45] V. Adivarahan, S. Wu, J. P. Zhang, A. Chitnis, M. Shatalov, V. Mandavilli, R. Gaska, and M. Asif Khan. Appl. Phys. Lett. **84**, 4762 (2004).

[46] A. J. Fischer, A. A. Allerman, M. H. Crawford, K. H. A. Bogart, S. R. Lee, R. J. Kaplar, W. W. Chow, S. R. Kurtz, K. W. Fuller, and J. J. Figiel, Appl.Phys. Lett. **84**, 3394 (2004).

[47] S. Wu, V. Adivarahan, M. Shatalov, A. Chitnis, W. Sun, and M. Asif Khan, Jpn. J. Appl. Phys. **43**, L1035 (2004).

[48] M. L. Nakarmi, K. H. Kim, M. Khizar, Z. Y. Fan, J. Y. Lin, and H. X. Jiang, Appl. Phys. Lett. **86**, 092108 (2005).

[49] Y. Taniyasu, M. Kasu, and N. Kobayashi, Appl. Phys. Lett. **81**, 1255 (2002).

[50] M. L. Nakarmi, K. H. Kim, K. Zhu, J. Y. Lin, and H. X. Jiang, Appl. Phys. Lett. **85**, 3769 (2004).

[51] K. B. Nam, M. L. Nakarmi, J. Y. Lin, and H. X. Jiang, Appl. Phys. Lett. **86**, 222108 (2005).

[52] C.G. Van de Walle and J. Neugebauer, J. Appl. Phys**. 95**, 3851 (2004).

[53] T. Mattila and R.M. Nieminen, Phys. Rev. B **55**, 9571 (1997).

[54] C. Stampfl and C.G. Van de Walle, Phys. Rev. B **65**, 155212 (2002).

[55] I. Gorczyca, N.E. Christensen, and A. Svane, Phys. Rev. B **66**, 075210 (2002).

[56] J. Oila, J. Kivioja, V. Ranki, K. Saarinen, D. C. Look, R.J. Molnar, S. S. Park, S. K. Lee, and J. Y. Han, *Appl. Phys. Lett*. **82**, 3433 (2003).

[57] T. Takeuchi, S. Sota, M. Katsuragawa, M. Komori, H. Takeuchi, H. Amano, and Akasaki, Jpn. J. Appl. Phys., Part 2 **36**, L382 (1997).

[58] M. Shur. B. Gelmont. and M. Asif Khan, J. Electron. Mater. **25**, 777 (1995).

[59] M. Sumiya, K. Yoshimura. K. Ohtsuka, and S. Fuke, Appl. Phys. Lett. **76**, 2098, (2000).

[60] F. Tumisto, K. Saarinen. B. Lucznik, I. Grzegory, H. Teisseryre, T. Suski, S. Porowski, P.R. Hageman, and J. Likonen, Appl. Phys. Lett. **86,** 031915, (2005).

[61] M. Sumiya and S. Fuke, MRS Internet J. Nitride Semicond. Res. **9**, 1 (2004).

[62] http://www.phys.ksu.edu/area/GaNgroup

[63] M. Seelmann-Eggebert, J. L. Weyher, H. Obloh, H. Zimmermann, A. Rar, and S. Porowski, Appl. Phys. Lett. **71**, 2635 (1997).

[64] J. L. Weyher, S. Muller, I. Grzegory, and S. Porowski, J. Cryst. Growth **182**, 17 (1997).

[65] M. Sumiya, T. Ohnishi, M. Tanaka, A. Ohtomo, M. Kawasaki, M. Yoshimoto, H. Koinuma, K. Ohtsuka, and S. Fuke, MRS Internet J. Nitride Semicond. Res. **4S1**G6.23 (1999).

[66] J. L. Rouviere, J. L. Weyher, M. Seelmann-Eggebert, and S. Porowski, Appl. Phys. Lett. **73**, 668 (1998).

[67] H. S. Kim, R. A. Mair, J. Li, J. Y. Lin, and H. X. Jiang, Appl. Phys. Lett. **76**, 1252 (2000).

[68] G. Coli, K. K. Bajaj, J. Li, J. Y. Lin, and H. X. Jiang, Appl. Phys. Lett. **80**, 2907 (2002).

[69] N. Nepal, M. L. Nakarmi, J. Y. Lin, and H. X. Jiang , Appl. Phys. Lett. **89,** 092107

(2006).

[70] C. J. Collins, A. V. Sampath, G. A. Garrett, W. L. Saeney, H. Shen, M. Wraback, A. Yu. Nikiforov, G. S. Cargill, and V. Dierolf, Phys. Appl. Phys. Lett. **86**, 031916 (2005).

[71] H. Hirayama, Y. Enomoto, A. Kinoshita, A.Hirata, and Y. Aoyagi, Appl. Phys. Lett. **80**, 37 (2001).

[72] V. Adivarahan, S. Wu, J. P. Zhang, A. Chitnis, M. Shatalov, V. Mandavilli, R. Gaska, and M. Asif Khan, Appl. Phys. Lett. **84**, 4762 (2004).

[73] J. P. Zhang, A. Chitnis, V. Adivarahan, S. Wu, V. Mandavilli, R. Pachipulusu, M. Shatalov, G. Simin, J. W. Yang, and M. Asif Khan, Appl. Phys. Lett. **81**, 4910 (2002).

[74] A. Yasan, R. McClintock, K. Mayes, D. Shiell, L. Gautero, S. R. Darvish, P. Kung, and M. Razeghi, Appl. Phys. Lett. **83**, 4701 (2003).

[75] A. Hanlon, P. M. Pattison, J. F. Kaeding, R. Sharma, P. Fini, and S. Nakamura, Jpn. J. Appl. Phys., Part 2 **42**, L628 (2003).

[76] A. J. Fischer, A. A. Allerman, M. H. Crawford, K. H. A. Bogart, S. R. Lee, R. J. Kaplar, W. W. Chow, S. R. Kurtz, K. W. Fuller, and J. J. Figiel, Appl.Phys. Lett. **84**, 3394 (2004).

[77] S. Wu, V. Adivarahan, M. Shatalov, A. Chitnis, W. Sun, and M. Asif Khan, Jpn. J. Appl. Phys. **43**, L1035 (2004).

[78] H. S. Kim, R.A. Mair, J. Li, J.Y. Lin, and H. X. Jiang, Appl. Phys. Lett. **76**, 1252 (2000).

[79] A. Bonfiglio, M. Lomascolo, R. Cingolani, A. Di Carlo, F. Della Sala, P. Lugli, A. Botchkarev, and H. Morkoc, J. Appl. Phys. **87**, 2289 (1999).

[80] J. Wang, J. B. Jeon, M. Sirenko, and K. W. Kim, IEEE Photonics Technol. Lett. **9**, 728 (1997).

[81] W. Chow, M. Kira, and S. W. Koch, Phys. Rev. B **60**, 1947 (1999).

[82] C. H. Henry, R. A. Loganr, and F. R. Merritt, J. Appl. Phys. **51**, 3042 (1980).

[83] I. Vurgaftman, J. R. Meyer, and L.R. Ram-Mohan, J. Appl. Phys. **89**, 5815 (2001).

[84] K. C. Zeng, J. Li, J.Y. Lin, and H. X. Jiang, Appl. Phys. Lett. **76**, 3040 (2000).

[85] S. H. Park and S. L. Chuang, Appl. Phys. Lett. **72**, 3103 (1998).

[86] J. S. Im, H. Kollmer, J. Off, A. Sohmer, F. Scholtz, and A. Hangleiter, Phys. Rev. B **57**, R9435 (1998).

[87] S. Chichibu, T. Azuhata, T. Sota, and S. Nakamura,Appl. Phys. Lett. **69**, 4188 (1996).

[88] A. Satake, Y. Masumoto, T. Miyajima, T. Asatsuma, F. Nakamura, and M. Ikeda, Phys. Rev. B **57**, R2041 (1998).

[89] C. Bodin, R. Andre, J. Cibert, Le Si Dang, D. Bellet, G. Feuillet, and P. H. Jouneau, Phys. Rev. B **51**, 13181 (1995).

[90] N. Nepal, J. Li, M. L. Nakarmi, J.Y. Lin, and H. X. Jiang, Appl. Phys. Lett. **88**, 062103 (2006).

[91] A. Bykhovski, B. Gelmont, and M. S. Shur, Appl. Phys. Lett. **63**, 2243 (1993).

[92] M. A. Khan, J. W. Yang, G. Simin, H. Loye, R. Bicknell, R. Gaska, M. S. Shur, and G. Tamulaitis, Phys. Stat. Sol. **A 176**, 227 (1999).

[93] H. Amano, M. Iwaya, T. Kashima, M. Katssuragawa, I. Akasaki, J. Han, S. Hearne, J. Floro, E. Cheson, and J. Figiel, Jpn. J. Appl. Phys. Lett. **37**, L1540 (1998).

[94] X. Hu, J. Deng, N. Pala, R. Gaska, M. S. Shur, C. Q. Chen, J. Yang, S. Simin, M. A. Khan, C. Rojo, and L. J. Schowalter, Appl. Phys. Lett. **82**, 1299 (2003).

[95] R. Gaska, C. Chen, J. Yang, E. Kuokstis, M. A. Khan, G. Tamulaitis, I. Yalmaz, M. S. Shur, J. C. Rojo, and L. J. Schowalter, Appl. Phys. Lett. **81**, 4658 (2002).

[96] S. Ghosh, P. Waltereit, O. Brandt, H. T. Grahn, and K. H. Ploog, Phys. Rev. **B65**, 075202 (2002).

[97] Y. Taniyasu, M. Kasu, and T. Makimoto, Nature **441**, 325 (2006).

[98] J. Li, Z. Y. Fan, R. Dahal, M. L. Nakarmi, J. Y. Lin, and H. X. Jiang, Appl. Phys. Lett. **89**, 213510 (2006).

[99] T. Matsutani, M. Kiuchi, K. Shirouzu, A. Yoshioka, R. Shimizu, and S. Takahashi, Solid State Phenom. **107**, 43 (2005).

[100] V. Mortet, O. Elmazria, M. Nesladek, M. B. Assouar, G. Vanholyland, J. D'Haen, M. D'Olieslaeger, and P. Alnot, Appl. Phys.Lett. **81**, 1720 (2002).

[101] A. T. Sowers, J. A. Christman, M. D. Bremser, B. L. Ward, R. F. Davis, and R. J. Nemanich, Appl. Phys. Lett. **71**, 2289 (1197).

[102] K. H. Kim, Z. Y. Fan, M. Khizar, M. L. Nakarmi, J. Y. Lin, and H. X. Jiang, Appl.

Phys. Lett. **85**, 4777 (2004).

[103] S. Arulkumaran, M. Sakai, T. Egawa, H. Ishikawa, and T. Jimbo, T. Shibata, K. Asai, S. Sumiya, Y. Kuraoka, M. Tanaka, and O. Oda, Appl. Phys. Lett. **81**, 1131 (2002).

[104] B. Zhang, T. Egawa, H. Ishikawa, Y. Liu, and T. Jimbo, J. Appl. Phys **95**, 3170 (2004).

[105] T. M. Al tahtamouni, N. Nepal, J. Y. Lin, H. X. Jiang, and W. W. Chow, Appl. Phys. Lett. **89,** 131922 (2006).

[106] T. Takeuchi, H. Amano, and I. Akasaki, Jpn. J. Appl. Phys. **39,** 413 (2000).

[107] K. B. Nam, J. Li, M. L. Nakarmi, J. Y. Lin, and H. X. Jiang, Appl. Phys. Lett. **84**, 5264 (2004).

[108] D. Doppalapudi, E. lliopoulos, S. N. Basu, and T. D. Moustakas, J. Appl. Phys. **85**, 3582 (1999).

[109] X. Ni, Y. Fu, Y. T. Moon, N. Biyikli, and H. Morkoc, J. Crystal. Growth. **290**, 166 (2006).

[110] M. D. Carven, S. H. Lim, F. Wu, J. S. Speck, and S. P. DenBaars, Appl. Phys. Lett. **81**, 469 (2002).

[111] A. Saxler, P. Kung, C. J. Sun, E. Bigan, and M. Razeghi, Appl. Phys. Lett. **64**, 339 (1993).

[112] Y. Tsuchiya, Y. Okadome, A. Honshio, Y. Miyake, T. Kawashima, M. Iwaya, S. Kamiyama, H. Amano, and I. Akasaki, Jpn. J. Appl. Phys. **44,** 1516 (2005).

[113] Y. Danylyuk, S. Perooly, M. Rahman, and G. Auner, Phys. Stat. Sol. (c) **2**, 2228 (2005).

[114] M. L. Nakarmi, N. Nepal, C. Ugolini, T. M. Al tahtamouni, J. Y. Lin, and H. X. Jiang, Appl. Phys. Lett. **89**, 152120 (2006).

[115] P. P. Paskov, R. Schifano, B. Monemar, T. Paskova, S. Figge, and Hommel, J. Appl. Phys. **98**, 093519 (2005).

[116] K. B. Nam, M. L. Nakarmi, J. Y. Lin, and H. X. Jiang, Appl. Phys. Lett. **86**, 222108 (2005).

[117] N. Nepal, M. L. Nakarmi, J. Y. Lin, and H. X. Jiang, Appl. Phys. Lett. **89**, 092107 (2006).

[118] N. Nepal, M. L. Nakarmi, K. B. Nam, J. Y. Lin, and H. X. Jiang, Appl. Phys. Lett. **85**, 2271 (2004).

[119] K.B. Nam, M. L. Nakarmi, J. Li, J. Y. Lin and H. X. Jiang**,** Appl. Phys. Lett **83**, 878 (2003).

[120] C. J. Collins, A. V. Sampath, G. A. Garrett, W. L. Saeney, H. Shen, M. Wraback, A.Yu. Nikiforov, G. S. Cargill, and V. Dierolf, Appl. Phys. Lett. **86**, 031916 (2005).

[121] H. Hirayama, Y. Enomoto, A. Kinoshita, A. Hirata, and Y. Aoyagi, Appl. Phys. Lett. **80**, 37 (2001).

[122] V. Adivarahan, S. Wu, J. P. Zhang, A. Chitnis, M. Shatalov, V. Mandavilli, R. Gaska, and M. Asif Khan, Appl. Phys. Lett. **84**, 4762 (2004).

[123] M. L. Nakarmi, K. H. Kim, M. Khizar, Z. Y. Fan, J. Y. Lin, and H. X. Jiang, Appl. Phys. Lett. **86**, 092108 (2005).

[124] A. Yasan, R. McClintock, K. Mayes, D. Shiell, L. Gautero, S. R. Darvish, P.Kung, and M. Razeghi, Appl. Phys. Lett. **83**, 4701 (2003).

[125] A. J. Fischer, A. A. Allerman, M. H. Crawford, K. H. A. Bogart, S. R. Lee, R. J. Kaplar, W. W. Chow, S. R. Kurtz, K. W. Fuller, and J. J. Figiel, Appl. Phys. Lett. **84**, 3394 (2004).

[126] S. Wu, V. Adivarahan, M. Shatalov, A. Chitnis, W. Sun, and M. Asif Khan, Jpn. J. Appl. Phys., Part 2 **43**, L1035 (2004).

[127] E. Kuokstis, W. H. Sun, C. Q. Chen, J. W. Yang, and Asif Khan, J. Appl. Phys. **97**, 103719 (2005).

[128] H. M. Ng, Appl. Phys. Lett. **80**, 4369 (2002).

[129] M. D. Craven, S. H. Lim, F. Wu, J. S. Speck, and S. P. DenBaars, Appl. Phys. Lett. **81**, 469 (2002).

[130] N. Akopian, G. Bahir, D. Gershoni, M. D. Carven, J. S. Speck, and S. P. DenBaars, Appl. Phys. Lett. **86**, 202104 (2005).

[131] K. C. Zeng, J. Li, J. Y. Lin, and H. X. Jiang, Appl. Phys. Lett. **76**, 3040 (2000).

[132] N. Nepal, J. Li, M. L. Nakarmi, J. Y. Lin, and H. X. Jiang, Appl. Phys. Lett. **88**, 062103 (2006).

[133] S. Founta, F. Rol, E. Bellet-Amalric, J. Bleuse, B. Daudin, B. Gayral, and H. Mariette, and C. Moisson, Appl. Phys. Lett. **86**, 171901 (2005).

[134] H. Amano, N. Sawaki, I. Akasaki, and Y. Toyoda, Appl. Phys. Lett. **48**, 353 (1986).

[135] T. W. Weeks, M. D. Bremser, K. S. Ailey, E. Carlson, W. G. Perry, and R. F. Davis, Appl. Phys. Lett. **67**, 401 (1995).

[136] J. P. Zhang, M. Asif Khan, W. H. Sun, H. M. Wang, C. Q. Chen, Q. Fareed, E. Kuokstis, and J. W. Yang, Appl. Phys. Lett. **81**, 4392 (2002).

[137] F. Yan, M. Tsukihara, A. Nakamura, T. Yadani, T. Fukumoto, Y. Naoi, and S. Sakai, Jpn. J. Appl. Phys. **43**, L1057 (2004).

[138] Y. Ohba and R. Sato, J. Cryst. Growth **221**, 258 (2000).

[139] C. M. Zetterling, M. Östling, N. Nordell, O. Schön, and M. Deschler, Appl. Phys. Lett. **70**, 3549 (1997).

[140] N. Onojima, J. Suda, and H. Matsunami, Jpn. J. Appl. Phys. **42**, L445 (2003).

[141] S. Dogan, D. Johnstone, F. Yun, S. Sabuktagin, J. Leach, A. Baski, H. Morkoc, G. Li, and B. Ganguly, Appl. Phys. Lett. **85**, 1547 (2004).

[142] E. Sanchez, J. Grim, M. Skowronski, W. Vetter, M. Dudley, R. Bertke, and C. Mitchell, J Electrochem Soc. **149**, G131 (2002).

[143] W. Qian, M. Skowronski, G. Augustine, R. Glass, H. Hobgood, and R. Hopkins, J. Electrochem. Soc.**142**, 4290 (1995).

[144] V. Ramachandran, M. F. Brady, A. R. Smith, R. M. Feenstra, and D. W. Greve, J. Electron. Mater. **27**, 308 (1998).

[145] H. Amano, K. Hiramatsu, and I. Akasaki, Jpn. J. Appl. Phys. **27**, 1484 (1988).

[146] K. Hiramatsu, T. Detchprohm, and I. Akasaki, Jpn. J. Appl. Phys. **32**, 1528 (1993).

[147] Y. Ishihara, J. Yamamoto, M. Kurimoto, T. Takano, and T. Honwanishi, Jpn. J. Appl. Phys. **38**, L1296 (1999).

[148] K. B. Nam, J. Li, M. L. Nakarmi, J. Y. Lin, and H. X. Jiang, Appl. Phys. Lett. **82**, 1694 (2003).

[149] R. Dahal, T. M. Al Tahtamouni, Z. Y. Fan, J. Y. Lin, and H. X. Jiang, Appl. Phys. Lett. **90**, 263505 (2007).

[150] Y. Taniyasu, M. Kasu, and N. Kobayashi, Appl. Phys. Lett. **81**, 1255 (2002).

[151] M. L. Nakarmi, K. H. Kim, K. Zhu, J. Y. Lin, and H. X. Jiang, Appl. Phys. Lett. **85**, 3769 (2004).

[152] Y. Taniyasu, M. Kasu, and T. Makimoto, Appl. Phys. Lett. **85**, 4672 (2004).

[153] T. Ive, O. Brandt, H. Kostial, K. J. Friedland, L. Daweritz, and K. H. Ploog, Appl. Phys. Lett. **86**, 024106 (2005).

[154] J. Neugebauer and C. G. Van de Walle, Appl. Phys. Lett. **69**, 503 (1996).

[155] T. Mattila and R. M. Nieminen, Phys. Rev. B **55**, 9571 (1997).

[156] C. Stampfl and C. G. Van de Walle, Phys. Rev. B **65**, 155212 (2002).

[157] I. Gorczyca, N. E. Christensen, and A. Svane, Phys. Rev. B **66**, 075210 (2002).

[158] K. B. Nam, M. L. Nakarmi, J. Y. Lin, and H. X. Jiang, Appl. Phys. Lett. **86**, 222108 (2005).

[159] N. Nepal, M. L. Nakarmi, J. Y. Lin, and H. X. Jiang, Appl. Phys. Lett. **89**, 092107 (2006).

[160] B. Pödör, Phys. Status Solidi **16**, K167 (1966).

[161] A. Y. Polyakov, N. B. Smirnov, A. V. Govorkov, M. G. Milidivskii, J. M. Redwing, M. Shin, M. Showronski, D. W. Greve, and R. G. Wilson, Solid State Electron. **42**, 627 (1998).

[162] P. Cantu, S. Keller, U. Mishra, S. DenBaars, Appl. Phys. Lett. **82**, 3683 (2003).

[163] V. Adivarahan, G. Simin, G. Tamulaitis, R. Srinivasan, J. Yang, A. Khan, M. Shur, and R. Gaska, Appl. Phys. Lett. **79**, 1903 (2001).

[164] H. Kang, S. Kandoor, S. Gupta, I. Ferguson, S. P. Guo, and M. Pophristic, Phys. Stat. Sol. (c) **2**, 2145 (2005).

[165] C. Stampfl and C. Van de Walle, Appl. Phys. Lett. **72**, 459 (1998).

[166] M. L. Nakarmi, N. Nepal, C. Ugolini, T. M. Altahtamouni, J. Y. Lin, and H. X. Jiang, Appl. Phys. Lett. **89**, 152120 (2006).

[167] X. H. Wu, P. Fini, E. J. Tarsa, B. Heying, S. Keller, U. K. Mishra, S. P. DenBaars, and J. S. Speck, J. Cryst. Growth. **190,** 231 (1998).

[168] P. Cantu, F. Wu, P. Waltereit, S. Keller, A. E. Romanov, U. K. Mishra, S. P. DenBaars, and J. S. Speck, Appl. Phys. Lett. **83**, 674 (2003).

[169] H. S. Kim, R. A. Mair, J. Li, J. Y. Lin, and H. X. Jiang, Appl. Phys. Lett. **76**, 1252 (2000).

[170] G. Coli, K. K. Bajaj, J. Li, J. Y. Lin, and H. X. Jiang, Appl. Phys. Lett. **80**, 2907 (2002).

[171] N. Nepal, M. L. Nakarmi, J. Y. Lin, and H. X. Jiang, Appl. Phys. Lett. **89,** 092107 (2006).

[172] B. N. Pantha, R. Dahal, M. L. Nakarmi, N. Nepal, J. Li, J. Y. Lin, and H. X. Jiang, Appl. Phys. Lett. **90,** 241101 (2007).

[173] A. Salvador, W. Kim, O. Aktas, A. Botchkarev, Z. Fan, and H. Morkoc, Appl. Phys. Lett. **69**, 2692 (1996).

[174] T. Cheng, S. Hooper, L. Jenkins, C. Foxon, D. Lacklison, J. Dewsnip, and J. Orton, J. Cryst. Growth **166**, 597 (1996).

[175] C. Ronning, E. Carlson, D. Thomson, and R. Davis, Appl. Phys. Lett. **73**, 1622 (1998).

[176] C. Ronning, K. Linthicum, E. Carlson, P. Hartlieb, D. Thomson, T. Gehrke, and R. Davis, MRS Internet J. Nitride Semicond. Res. **4S1**, G3.17 (1999).

Appendix A - Research work publications

1. B. N. Pantha, N. Nepal, **T. M. Al Tahtamouni**, M. L. Nakarmi, J. Li, J. Y. Lin, and H. X. Jiang, "Correlation between biaxial stress and free exciton transition in AlN epilayers", Appl. Phys. Lett. **91**, 121117 (2007).
2. **T. M. Al Tahtamouni**, A. Sedhain, J. Y. Lin, and H. X. Jiang, "Growth and photoluminescence studies of *a*-plane AlN/$Al_xGa_{1-x}N$ quantum wells", Appl. Phys. Lett. **90**, 221105 (2007).
3. R. Dahal, **T. M. Al Tahtamouni**, Z. Y. Fan, J. Y. Lin, and H. X. Jiang, "Hybrid AlN–SiC deep ultraviolet Schottky barrier photodetectors", Appl. Phys. Lett. **90**, 263505 (2007).
4. **T. M. Al Tahtamouni**, N. Nepal, J. Y. Lin, and H. X. Jiang, "Al rich AlN/AlGaN Quantum Wells", Mater. Res. Soc. Symp. Proc. Vol. 955 © 2007 Materials Research Society.
5. **T. M. Al Tahtamouni**, N. Nepal, J. Y. Lin, H. X. Jiang, and W. W. Chow, "Growth and photoluminescence studies of Al-rich AlN/$Al_xGa_{1-x}N$ quantum wells", Appl. Phys. Lett. **89**, 131922 (2006).
6. M. L. Nakarmi, N. Nepal, C. Ugolini, **T. M. Al Tahtamouni**, J.Y. Lin, and H. X. Jiang, "Correlation between optical and electrical properties of Mg-doped AlN epilayers", Appl. Phys. Lett. **89**, 152120 (2006).